

**Immunological synapse arrays: Patterned protein  
surfaces that modulate immunological synapse structure  
formation in T cells**

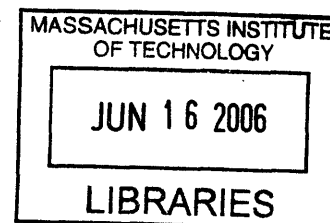
By  
**Junsang Doh**

**B.S. Chemical Engineering  
Seoul National University, 1999**

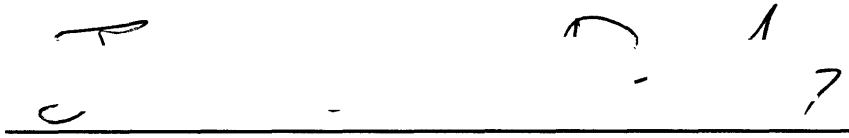
**SUBMITTED TO THE DEPARTMENT OF CHEMICAL ENGINEERING IN  
PARTIAL FULFILLMENT OF THE REQUIREMENTS FOR THE DEGREE OF  
DOCTOR OF PHILOSOPHY IN CHEMICAL ENGINEERING  
AT THE  
MASSACHUSETTS INSTITUTE OF TECHNOLOGY**

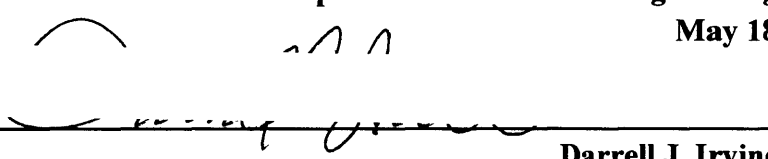
**JUNE 2006**

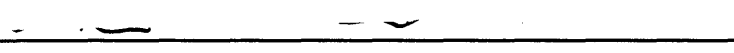
**© 2006 Massachusetts Institute of Technology  
All right reserved.**



**ARCHIVES**

Signature of Author:   
Department of Chemical Engineering  
May 18

Certified by:   
Darrell J. Irvine  
Eugene Bell Career Development Associate Professor in Tissue Engineering  
Thesis Supervisor

Accepted by:   
William M. Deen  
Professor of Chemical Engineering  
Chairman, Committee for Graduate Students

# **Immunological synapse arrays: Patterned protein surfaces that modulate immunological synapse structure formation in T cells**

**By  
Junsang Doh**

**Submitted to the Department of Chemical Engineering  
on June, 2006 in Partial Fulfillment of the Requirements for the  
Degree of Doctor of Philosophy in Chemical Engineering**

## **ABSTRACT**

T cells are activated by recognition of foreign peptides displayed on the surface of antigen presenting cells (APCs), an event that triggers assembly of a complex microscale structure at the T cell-APC interface known as the immunological synapse (IS). It remains unresolved whether the unique physical structure of the synapse itself impacts the functional response of T cells, independent of the quantity and quality of ligands encountered by the T cell. As a first step toward addressing this question, we fabricated multicomponent protein surfaces that surrogate the role of APCs and studied T cell responses as a function of synapse structure.

To pattern multiple proteins on surfaces, we synthesized and characterized a new polymer, poly(o-nitrobenzyl methacrylate-r-methyl methacrylate-poly(ethylene glycol) methacrylate (PNMP), a photoresist that can be processed under mild aqueous conditions. Based on the pH- and temperature-sensitive solubility of UV-exposed PNMP random terpolymers in aqueous buffers, two-component protein patterning was achieved under conditions that avoid exposing proteins to conditions outside the narrow range of physiological pH, ionic strength, and temperature where their stability is greatest.

Using a photolithographic strategy we developed employing this novel PNMP photoresist polymer, we created multicomponent protein surfaces presenting micron-scale arrays of tethered T cell receptor (TCR) ligands (anti-CD3 'activation sites') surrounded by a field of tethered intercellular adhesion molecule-1 (ICAM-1), as a model substrate on which T cells could be seeded to mimic T cell-APC interactions. CD4<sup>+</sup> T cells seeded on these surfaces polarized and migrated; on contact with activation sites, T cells assembled an

IS with a structure modulated by the physical pattern of ligand encountered. On surfaces patterned with focal spots of TCR ligand, T cells stably interacted with activation sites, proliferated, and secreted cytokines. In contrast, T cells interacting with activation sites patterned to preclude centralized clustering of TCR ligand failed to form stable contacts with activation sites, exhibited aberrant PKC- $\theta$  clustering in a fraction of cells, and had significantly reduced production of interferon- $\gamma$ . These results suggest that focal clustering of TCR ligand characteristic of the 'mature' IS may be required under some conditions for full T cell activation.

**Thesis Supervisor: Darrell J. Irvine**

**Title: Eugene Bell Career Development Associate Professor in Tissue Engineering**

# Table of Contents

<b>List of Figures .....</b>	<b>7</b>
<b>List of Table .....</b>	<b>12</b>
<b>Acknowledgement .....</b>	<b>13</b>
<b>1 Background and Thesis Scope.....</b>	<b>15</b>
1.1 Microengineering of cellular microenvironments.....	15
1.2 T Cell Activation and the Immunological Synapse.....	16
1.3 Scope of Current Work.....	19
1.3.1 Developing a New Strategy for Patterning Multiple Proteins on Surfaces..	20
1.3.2 Current Strategies for Visualizing T Cell Activation and the Potential Role of Patterned Surfaces as a Tool for the Study of T Cell Triggering.....	23
1.3.3 Outline of the Thesis .....	27
<b>2 Synthesis and Characterization of o-Nitrobenzyl Methacrylate Containing     Photoresists for Multi-component Protein Patterning.....</b>	<b>29</b>
2.1 Materials and Methods .....	30
2.2 Synthesis of o-NBMA and PNMP .....	35
2.3 Composition Dependence of UV-Exposed Photoresist Film Solubility .....	38

### **3 Two-component Photolithographic Protein Patterning under Mild Aqueous**

<b>Conditions .....</b>	<b>47</b>
3.1 Materials and Methods .....	48
3.2 Dual Streptavidin Patterning Using Negative-tone Photoresist .....	55
3.3 Dual Streptavidin Patterning Using Positive-tone Photoresist.....	59
3.4 Protein Ligand Immobilization on streptavidin patterned surfaces .....	72

### **4 Fabrication of ‘Immunological Synapse Arrays’ and T Cell Responses to These**

<b>Patterned Surfaces .....</b>	<b>79</b>
4.1 Materials and Methods .....	81
4.2 Control of T cell Adhesion and Migration .....	87
4.3 Fabrication of the immunological synapse arrays.....	90
4.4 Early TCR signaling triggered by immunological synapse arrays.....	94
4.5 Dynamics of T cells interacting with immunological synapse arrays at late times and end point functional responses .....	100

### **5 Control of T cell activation by modulating immunological synapse formation in T**

<b>cells.....</b>	<b>104</b>
5.1 Materials and Methods .....	105
5.2 Subcellular components distribution in T cells on the adhesion field.....	106

5.3 Modulating the Immunological Synapse Formation in T cells .....	108
5.4 The Effect of Ligand Dstribution on T Cell Activation .....	113
<b>6 Conclusions and Future Work .....</b>	<b>122</b>
6.1 A Novel in vitro Platform for Studying Cell Biology .....	122
6.2 Issues for Future Work .....	123
6.2.1 Effect of costimulation .....	123
6.2.2 Effect of nano-scale ligand segregation .....	124
<b>7 Bibliography .....</b>	<b>128</b>
<b>8 Biographical Note.....</b>	<b>138</b>

## List of Figures

Figure 1. 1 Schematic of the immunological synapse.....	18
Figure 1. 2 Chemical structure of PNMP random terpolymer .....	22
Figure 1. 3 Schematics of immunological synapse array surface pattern .....	26
Figure 2. 1 Synthesis of o-nitrobenzyl methacrylate (o-NBMA).....	31
Figure 2. 2 <sup>1</sup> H NMR spectra of o-NBMA.....	36
Figure 2. 3 A representative <sup>1</sup> H NMR spectra of PNMP comprised of 36% o-NBMA, 40% MMA, and 24% PEGMA by weight. ....	37
Figure 2. 4 Photorearrangement of PNMP terpolymer .....	39
Figure 2. 5 Aqueous solubility of as-cast and UV-exposed thin films of PNMP terpolymers with compositions listed in Table 2. 1.....	40
Figure 2. 6 Trends in the pH-dependent solubility of exposed PNMP thin films as the amount of PEGMA is increased for approximately constant 60 wt% or 35 wt% o- NBMA.....	42
Figure 2. 7 Dissolution of exposed thin films of Polymer L at 4°C in various pHs and temperatures. ....	46

Figure 3. 1 Biotinylation of hydroxyl termini of PEGMA.....	50
Figure 3. 2 Two component patterning of proteins on a surface using a negative-tone photoresist. ....	57
Figure 3. 3 Grayscale fluorescence intensity images of glass substrates patterned using a film of PNMP terpolymer L. ....	58
Figure 3. 4 Chemical structure of terpolymer H', and its mechanism for <i>in situ</i> polyelectrolyte bilayer formation. ....	62
Figure 3. 5 UV exposure time vs. remaining terpolymer H' film thickness. ....	62
Figure 3. 6 UV-exposed, developed, and methylene blue-stained photoresist surface .....	63
Figure 3. 7 pH-dependent solubility of the UV-exposed photoresist. ....	64
Figure 3. 8 Schematic procedure of dual streptavidin patterning using positive-tone biotinylated photoresist. ....	66
Figure 3. 9 Chemical structure of PNMP before and after UV exposure, and schematic structure of patterned surface shown in Figure 3. 8B. ....	67
Figure 3. 10 Fluorescent microscopy of dual streptavidin patterned surface.....	68
Figure 3. 11 Specific (biotin-mediated) and nonspecific streptavidin binding to photoresist surfaces.....	71
Figure 3. 12 Immobilization and visualization of biotinylated monoclonal antibodies.....	74



Figure 3. 13 Immobilization and visualization of ICAM-1/Fc chimera. ....	75
Figure 3. 14 Measurement of patterned ICAM-1 surface stability. ....	78
Figure 4. 1 Schematic of immunological synapse array surface pattern.....	80
Figure 4. 2 Various surface densities of anti-CD3 detected by Cy-2-coupled anti-hamster antibody. ....	86
Figure 4. 3 Percentage of T cells adhering on various surfaces in 20 minutes. ....	88
Figure 4. 4 Instant velocity of two representative T cells on ICAM-1 surfaces and anti- LFA-1 surfaces. ....	89
Figure 4. 5 Time lapse images of T cells on ICAM-1 surfaces and anti-LFA-1 surfaces..	90
Figure 4. 6 Fabrication of immunological synapse arrays. ....	93
Figure 4. 7 Cell morphology and calcium signaling (tracked by fura fluorescence ratio) as single OT-II CD4 <sup>+</sup> T cells contact a control or anti-CD3-presenting activation site of a synapse array. ....	95
Figure 4. 8 Representative instantaneous velocities and average fura ratios of two different single T cells encountering activation sites on immunological synapse surfaces.....	96
Figure 4. 9 5C.C7 T cells interacting with titrated surface densities of anti-CD3 immobilized in 6 $\mu\text{m}$ -diameter activation sites. ....	98

Figure 4. 10 Time-averaged FURA ratio (20 min - 40 min) as a measure of calcium signaling in 5C.C7 T cells that stably interacted with 6 $\mu$ m-diameter activation sites bearing titrated surface densities of anti-CD3.....	98
Figure 4. 11 T cell localization to activation sites 30 min after seeding on immunological synapse surfaces presenting arrayed spots of anti-CD3 vs. control surfaces bearing arrayed spots of a control IgG. ....	100
Figure 4. 12 Time-lapse image sequence depicting a 5C.C7 CD4+ T cell undergoing cell division on a synapse array surface.....	101
Figure 4. 13 IL-2 and IFN- $\gamma$ production by OT-II CD4+ T cell blasts incubated on surfaces for 48 hrs. ....	103
Figure 4. 14 Normalized IL-2 secretion by T cells cultured on ‘focal’ synapse arrays as a function of activation site diameter or anti-CD3 density within activation sites.....	103
Figure 5. 1 Representative tubulin staining of a T cell migrating on an ICAM-1 surface.	108
Figure 5. 2 Representative TCR and phosphotyrosine (pY) immunostaining of a T cell migrating on an ICAM-1 surface. ....	108
Figure 5. 3 The immunological synapse formed in T cells interacting with 6 $\mu$ m focal activation sites.....	110

Figure 5. 4 Representative micrographs of the immunological synapse formed by a T cell interacting with a 2 $\mu$ m activation site. ....	111
Figure 5. 5 Synapse array patterns template T cell surface receptor and intracellular signaling molecule accumulation at the cell-surface contact site. ....	113
Figure 5. 6 T cell responses to ‘focal’ vs. ‘annular’ anti-CD3 activation sites. ....	116
Figure 5. 7 IL-2 and IFN- $\gamma$ secreted by 5C.C7 T cells cultured on focal vs. annular activation site patterns after 48 hrs.....	118
Figure 5. 8 Time average (20-40 min) FURA ratio of T cells on focal and annular activation sites.....	119
Figure 5. 9 Subcellular localization of TCR and cytoplasmic phosphotyrosine (pY) in T cells interacting with ‘focal’ and ‘annular’ anti-CD3 activation sites.....	120
Figure 5. 10 Th1/Th2 polarization of primed 5C.C7 T cells used in our studies revealed by intracellular cytokine staining followed by flow cytometry analysis. ....	121
Figure 6. 1 Nanoparticle patterned surfaces for T cell activation. ....	126
Figure 6. 2 Schematic representation of nanoparticle patterned surfaces for studying the effect of nanoscale ligands segregation.....	127

## List of Table

Table 2. 1 Composition and molecular weight of PNMP random terpolymer ..... 33

# Acknowledgment

First of all, I would like to thank my thesis advisor, Professor Darrell J. Irvine, for his patience, advice, and encouragement. I struggled a lot at the beginning because I started without having any lab experience and background in biology. He guided me with patience, and waited until I figured out things and made those work. He has been and will be a great mentor for my scientific career; I learned how to set challenging but tractable problems and how to approach those problems with different angles from others. I am also grateful for his great care on everything; in particular, spending a lot of time in correcting my manuscripts and slides for presentation. Thanks to his hard training, I could significantly improve skills for presenting my work.

I would also like to thank my thesis committee members, Professors. Robert Cohen, Paula Hammond, and David Schauer for their helpful comments and guidance. In particular, I am very grateful to Prof. Cohen for being supportive from the beginning of my graduate student years.

I would like to thank all the people in Irvine group. I greatly enjoyed interacting with people from diverse background. In particular, I am grateful to Siddhartha Jain for his friendship, help and insightful suggestion for experiments. We have spent so much time together, so I cannot imagine my MIT life without him. I was fortunate to have a very smart and motivated UROP, Joshua Katz. He made significant contribution in synthesizing and characterizing various compositions of PNMP terpolymers and developing a negative-tone photoresist for protein patterning. I greatly appreciate his hard working.

I am deeply thankful to Dr. Sangyong Jon for teaching me the synthesis of o-nitrobenzyl methacrylate, which turned out to be the most critical part for my thesis. I thank Jim Daley in nano structure lab and Fred Cote in student machine shop for helping me building up benchtop lithography setups.

I would like to thank Juhyun Park, my classmate of PPST and also my roommate, Heejae Kim, and Daeyeon Lee who have spent most of my outside lab life together. Also I would like to thank people whom I interacted a lot in my early MIT life and who helped me settling down at MIT: Jane Park, Daehee Hwang, Jiehyun Seong, Gyoo Yeol Jung, Ilsoon Lee, Hongwoo Kwon, Yoo Yeon Won, Young Hwan Kwon, and Sungjee Kim.

Special thanks have to go for Professor Kookheon Char, my undergraduate mentor, for

his consistence guidance and support.

Finally, I would like to thank my family, my mother, sister, and brother in law, for their love and support. Without them, I could not be here. This thesis is dedicated to my father who encouraged me to pursue Ph.D., and taught me the importance of hard working. You deserve to get credits for whatever I have achieved in here, and I will accomplish in the future.

This work is supported by DuPont-MIT alliance and Arnold and Mabel Beckman Foundation.

# 1 Background and Thesis Scope

## 1.1 Microengineering of cellular microenvironments

Cellular functions such as adhesion, migration, differentiation, gene expression, growth and death are determined by integrating signals from the outside of cells with the genetic codes existing inside cells. Although local microenvironments including extracellular matrix (ECM), soluble factors, ECM-bound factors, and neighboring cells have significant influences on cellular processes,<sup>1-4</sup> sorting out the role of each signaling cue on cellular functions is extremely difficult due to the complex nature of *in vivo* environments. To overcome this, researchers conduct *in vitro* cell culture with signaling molecules either homogeneously coated on tissue culture plates or dissolved in cell culture media. However, in many cases, not only the signaling cues but also their spatial distribution plays a critical role in controlling cellular behavior.

To address this complexity, microscale patterns of proteins immobilized on surfaces can be used to dissect the role of spatial organization in the signals transferred to cells from

the extracellular matrix or other cells.<sup>5-7</sup> By presenting ligands in a spatially defined manner from a synthetic substrate, cell functions such as life or death,<sup>8</sup> adhesion and migration,<sup>9,10</sup> cell division,<sup>11</sup> receptor clustering and membrane compartmentalization,<sup>12</sup> and differentiation<sup>13</sup> can be controlled, and the role of physical patterns of cell- or extracellular matrix-derived signals on cell responses can be elucidated. Studies of this type have to date primarily focused on cell responses to a single signaling or adhesion protein patterned into defined regions, surrounded by a ‘background’ that lacks protein.<sup>8-10,12,13</sup> However, surfaces comprised of multiple signaling proteins patterned into distinct regions on cellular and sub-cellular length scales would be useful for the study of the complex, spatially organized receptor-ligand interactions that occur in many cell-cell and cell-extracellular matrix contacts.<sup>14-18</sup>

## **1.2 T Cell Activation and the Immunological Synapse**

T cell activation is a crucial initial step in the adaptive immune response. Antigen-stimulated T cells combat invading microbes including bacteria and viruses by either organizing the actions of effector cells through the secretion of directive cytokines or directly killing infected host cells. Given their critical role in developing immunity, understanding and controlling of T cell activation is extremely important in preventing



autoimmune diseases as well as eliminating foreign pathogens.

The interactions between T cells and antigen presenting cells (APCs) during T cell activation provide a stunning example of the types of complex cell-cell interactions mentioned above. T cells are activated when their T cell receptors (TCRs) recognize and engage antigenic peptides displayed on the surface of APCs. Upon TCR engagement with its cognate p-MHC, migrating T cells stop and change from a characteristic hand-mirror morphology to a rounded shape.<sup>19,20</sup> This change in migration and shape coincides with intracellular calcium mobilization,<sup>19,21-23</sup> which continues several hours for full T cell activation.<sup>24</sup> Antigen recognition induces the polarization of the T cell's microtubule organizing center (MTOC)<sup>25</sup> and formation of an immunological synapse.<sup>14,18</sup> The immunological synapse (IS) is a highly organized supramolecular structure found at the interface of T cell-APC conjugates. The 'mature' IS formed by T cells encountering high densities of agonist peptides is composed of a central cluster of TCRs engaging foreign peptide-Major Histocompatibility Complex (MHC) molecules on the APC surface, surrounded by a concentric ring of T cell integrins, particularly Lymphocyte Function-Associated Antigen-1 (LFA-1), binding APC Intercellular Adhesion Molecule-1 (ICAM-1) adhesion receptors in the periphery of the contact region.<sup>14,18</sup> (Figure 1. 1)

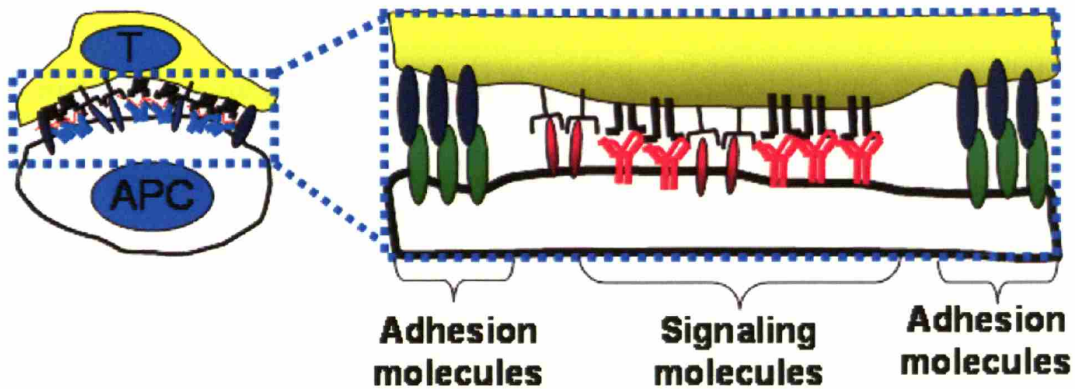


**Figure 1. 1 Schematic of the immunological synapse**

Intriguingly, this ‘mature IS’ structure is only one of several supramolecular organizations observed in T cell-APC communication: inverse patterns of receptor clustering (i.e., signaling receptors clustered peripherally, around a central accumulation of adhesion receptors) have been observed in the first few minutes of T cell activation prior to formation of a mature IS;<sup>14,26,27</sup> T cells encountering low (but fully activating) densities of foreign peptides show diffuse receptor clustering in the interface;<sup>28-30</sup> immature T cells exhibit multifocal clusters of receptors during interactions with APCs during positive selection,<sup>31,32</sup> and naïve T cell-dendritic cell conjugates have been reported to form only nanoscale clusters of receptors in their synapse.<sup>33</sup>

### **1.3 Scope of Current Work**

Motivated by this phenomenological diversity in synapse structures, there is great interest in understanding how different patterns of receptor and intracellular signaling molecule clustering at immune cell-cell interfaces may impact lymphocyte functional responses.<sup>34,35</sup> For example, Mossman et al., using patterned lipid bilayers where T cell ligands were confined to micron-scale ‘corrals’, showed that initial TCR signaling could be altered by preventing central clustering of TCR.<sup>36</sup> However, this work focused on early time point events (less than an hour after TCR triggering) such as TCR clustering, calcium influx, and phosphorylation of tyrosine in TCRs at the single cell level. It would be desirable to correlate these early single cellular events with longer term T cell responses such as proliferation and cytokine secretion in a bulk population level.

The hypothesis of this thesis is that the role of the immunological synapse structure in directing T cell functions can be dissected by using engineered surfaces designed to ‘replace’ the APC and present multiple protein ligands to T cells in fixed physical patterns mimicking (or not) the organization observed in native synapses. The first half of this work focuses on developing new patterning strategies for patterning multiple proteins in large areas with high fidelity so that bulk population assays as well as single cell microscopy can be performed with these patterned surfaces. The second goal of this work

is to investigate T cell responses to these patterned surfaces and determine the effect of ligand spatial patterning on T cell activation.

### 1.3.1 Developing a New Strategy for Patterning Multiple Proteins on Surfaces

Micron-scale patterns of proteins immobilized on surfaces are used in a broad range of applications, including proteomics arrays, biosensors, bioMEMs and microfluidic devices, and studies of cell-substrate interactions.<sup>5-7,37</sup> Recently, there have been a number of advances in methods for protein patterning over large areas (reviewed by Blawas and Reichert<sup>37</sup>). Notable examples include approaches based on photolithography,<sup>38,39</sup> photochemical immobilization,<sup>40-44</sup> and soft lithography.<sup>6,45-47</sup> However, with several exceptions,<sup>38,40,42-44,46,48</sup> the majority of reported patterning methods have focused on the immobilization of only one protein within select areas surrounded by a “blank” background. It is of significant interest to be able to pattern multiple protein components into defined, segregated locations on surfaces at micron length scales. Such surfaces can be used to mimic the complexity of the extracellular environment of tissues in well-defined, reproducible conditions, or stimulate cells via microscale arrangements of protein signals mimicking their interactions with other cell types *in vivo*.<sup>14-18</sup> High-resolution multicomponent patterning will also enable the creation of biosensors and protein

microarrays for proteomics that detect and identify more complex samples and require smaller sample sizes.<sup>49,50</sup> However, many challenges to multicomponent patterning of proteins exist due to their fragile nature, making them susceptible to harsh solvents, ultraviolet radiation, or dehydration, conditions common to established materials patterning technologies.<sup>37</sup>

Previously studied strategies to micropattern multiple proteins into distinct, arbitrary domains over large surface areas include the use of photomasking with a polymer film followed by film ‘lift-off’,<sup>38</sup> soft lithography with repeated stamping of proteins<sup>45</sup> or topographically-tiered microstamps,<sup>46</sup> or photochemical immobilization.<sup>40,42,43,48</sup> Each of these approaches has advantages and limitations. Approaches based on photomasking substrates followed by ‘lift off’ leverage well-developed existing technology from the microelectronics industry, but require dehydration of protein in the presence of a protectant (e.g., sucrose or trehalose) and exposure to organic solvents, which may lead to loss of protein activity.<sup>38</sup> Soft lithography methods have been widely demonstrated for protein patterning, but also generally require drying of protein solutions to ‘ink’ the poly(dimethylsiloxane) stamps used in this process.<sup>45,46</sup> Photochemical approaches utilizing caged biotin or photo-activated reactive groups readily permit multicomponent protein patterning under milder conditions, but may be limited by nonspecific protein

adsorption to unpatterned regions,<sup>40,43</sup> low efficiency of the photochemical reaction,<sup>42,48</sup> lack of control over immobilized protein orientation,<sup>42,44</sup> and/or have limited resolution due to photoexposure through a liquid solution layer.<sup>42,44</sup>

In an attempt to address some of the limitations encountered in the few studies on multicomponent protein patterning, we developed novel photoresist polymers that can be processed under mild conditions. Comb-architecture random terpolymers containing *o*-nitrobenzyl ester moieties (poly(*o*-nitrobenzyl methacrylate-co-methyl methacrylate-co-poly(ethylene glycol) methacrylate), PNMP) were synthesized to meet this goal (Figure 1.

2). The pH dependent solubility of PNMP terpolymers before and after UV exposure was fully investigated. Based on the physicochemical properties of PNMP terpolymers, two different methods for multicomponent protein patterning were developed.

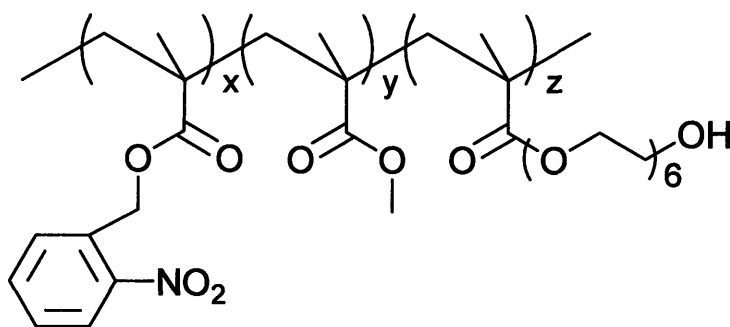


**Figure 1. 2 Chemical structure of PNMP random terpolymer**

### **1.3.2 Current Strategies for Visualizing T Cell Activation and the Potential Role of Patterned Surfaces as a Tool for the Study of T Cell Triggering**

Recent developments in novel microscopy techniques have dramatically extended our understanding of T cell antigen recognition and T cell-APC interactions from the level of single-molecule dynamics inside or on the surface of T cells to the level of cellular dynamics inside intact secondary lymphoid organs such as lymph nodes (LNs).<sup>51-56</sup>

Two-photon laser scanning microscopy has been extensively used to monitor the motility of lymphocytes,<sup>57-59</sup> T cell activation by specialized antigen presenting cells called dendritic cells (DCs),<sup>60-63</sup> and T cell-B cell interactions<sup>64</sup> in intact LNs. T lymphocytes rapidly crawl through the T-zone of LNs with average velocities of  $\sim 10 \mu\text{m}/\text{min}$ .<sup>57,58</sup> When they encounter DCs presenting their target antigens, they undergo new phases of behavior: first, they gradually slow down with transient contact with DCs, then form stable contact with DCs, regain their motility, and undergo several cell divisions.<sup>61,62</sup> Even though this deep tissue imaging technique allows global cellular behavior to be visualized in the physiological context, the short durations of contiguous observation possible ( $< 60$  min),<sup>57,60,61</sup> and limited resolution for observing subcellular scale molecular dynamics<sup>52,62,65</sup> limit the information that is currently obtained.

In vitro studies using wide field epifluorescence or confocal laser scanning

microscopy have provided useful alternatives for studying T cell activation under relatively well-defined and well-controlled conditions with better spatiotemporal resolution than *in vivo* tissue imaging. By observing interactions between antigen-pulsed APCs and T cells or planar lipid bilayers containing agonistic p-MHC and ICAM-1 with video microscopy, or fixed T cell-APC conjugates with deconvolution microscopy, the spatiotemporal distribution of receptors, signaling molecules, and cytoskeletal components related to TCR triggering have been studied in detail. The greatest advantage of such *in vitro* T cell studies is the capability to correlate early cellular or molecular events to late-term T cell responses such as proliferation and cytokine production.<sup>24,26,28,66-68</sup> However, the spatiotemporal resolution is limited by the diffraction of light and the time required for z-sectioning in 3-D imaging, thus single molecular dynamics or video rate observation of receptors or cytoplasmic components tracking has only been achieved in a few exceptional cases.<sup>29,69</sup>

Recent studies using total internal reflection fluorescence microscopy (TIRFM) have revealed a striking new view of TCR signaling.<sup>70-73</sup> Using this novel microscopy technique, the dynamics of nanoscale protein clusters below the resolution of far field microscopy were imaged at video rates, and their role in TCR signaling was elucidated in great detail. This technique can provide the best spatiotemporal resolution, but can be



only used to monitor membrane proximal regions of cells on planer surfaces where the TIRF evanescent wave of light can excite fluorophores (~200nm from the interface). For this reason, either planer supported bilayers<sup>71,72</sup> or anti-CD3 coated coverslips<sup>70,73</sup> have been used as surrogates for APCs.

Together, advances in optics and image analysis software have enabled the field of T cell biology to directly observe and analyze many molecular and cellular events in T cell activation at multiple time and length scales. However, there remain gaps between each approach to be integrated into a larger picture, partly due to difficulties in directly comparing results obtained from different experimental setups. In that sense, it is desirable to build in vitro systems that capture essential features of in vivo microenvironments while remaining compatible with a broad range of in vitro assays including new microscopy techniques as well as conventional biochemical and cellular analysis.

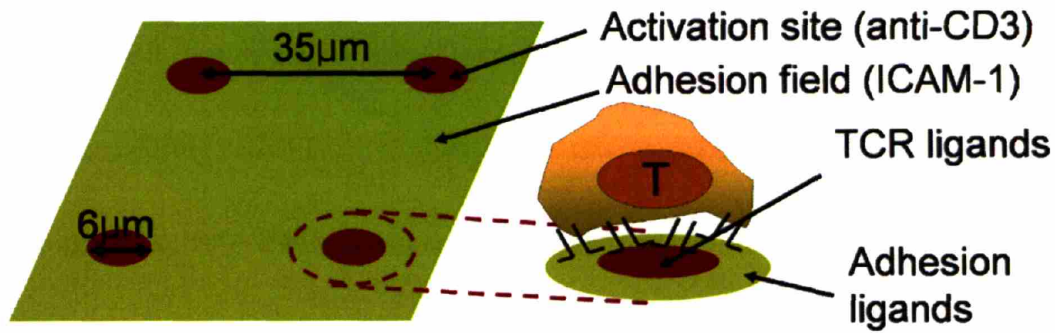


**Figure 1. 3 Schematics of immunological synapse array surface pattern**

As a new tool complementary to the experimental systems just described, we have used the protein patterning technology developed as part of this work to create the immunological synapse arrays schematically shown in Figure 1. 3. These arrays are composed of ‘activation sites’ containing immobilized TCR ligands in defined geometries, surrounded by immobilized adhesion proteins in an ‘adhesion field’. Photolithography techniques developed for patterning two component proteins are readily applicable to fabricate these patterned surfaces over large areas with high fidelity. The square array of activation sites surrounded by an adhesion field depicted above provides a crude mimic of discrete APCs surrounded by other cells within lymph nodes.<sup>74</sup> T cells seeded onto such a surface would initially polarize and migrate on the adhesion field, mimicking their migration within lymph nodes in search of antigen.<sup>57,61</sup> T cells encountering an activation site would be presented with a defined physical distribution of ligand; for the ‘mature IS’ protein pattern shown in Figure 1. 3, the responding cell would ‘see’ a concentric

distribution of TCR ligands and adhesion ligands mimetic of the receptor organization on the APC surface during native T cell triggering. Unlike intact LN tissue imaging, long term tracking of T cells ( $> 1\text{hr}$ ) is possible in this model system. Also, TIRFM, which provides the best spatiotemporal resolution among current state of art microscopy techniques, is readily applicable since it is a planer surface-based system. Moreover, the majority of common complementary experimental tools including those of biochemistry, cell biology, and imaging can be used in this model system.

In this thesis, we first tested whether we could reproduce responses observed at in vitro T cell-APC or T cell-APC surrogates studies including halt migration, calcium mobilization, synapse formation, proliferation, and cytokine secretion with our protein patterned surfaces to convince that the immunological synapse arrays. Then, we changed the geometries of the activation sites and investigated how T cell responses such as synapse structure, cellular dynamics, and cytokine production can be affected by the spatial distribution of TCR ligand.

### **1.3.3 Outline of the Thesis**

The experimental work carried out to fulfill the objectives discussed in sections 1.3.1 and 1.3.2 is presented in Chapters 2 through 5 of this thesis. Chapter 2 describes the

synthesis of aqueous-processible photoresist terpolymers and their composition-dependent solubility in water as a function of pH. Chapter 3 presents two different approaches using photoresist polymers described in Chapter 2 to fabricate dual streptavidin-patterned surfaces, and describes strategies to incorporate commercially available biotinylated or Fc fused proteins on these patterned substrates. In Chapter 4, the positive tone dual streptavidin patterning technique and commercially available ligand immobilization strategies discussed in Chapter 3 are integrated to fabricate the immunological synapse arrays. Cellular level T cell responses on fabricated surfaces such as migration, calcium influx, morphology, and cell division are described. In Chapter 5, assemblies of subcellular components including receptors, cytoplasmic signaling proteins, and the cytoskeleton of T cells interacting with synapse surfaces patterned with various ligands and different geometries of activation sites are described. Differences in cellular dynamics and subcellular organization were correlated with the functional outcome of T cell activation on these surfaces by measuring cytokine secretion by the responding cells. The thesis closes with a summary of conclusions gathered in this work and a discussion of important future directions.

## **2 Synthesis and Characterization of o-Nitrobenzyl Methacrylate Containing Photoresists for Multi-component Protein Patterning**

Photolithography is a technique primarily developed to pattern metallic or inorganic materials for the fabrication of electronic or electromechanical devices. Even though photolithography is a well-established technology for fabricating micron or submicron size features, its usage in patterning organic or biological materials has been limited due to the harsh processing conditions, in particular during the developing (typically performed by organic solvents or strong base solutions with sonication) and etching (highly reactive or corrosive species are used) steps of photolithographic processes. In this chapter, the synthesis and physicochemical properties of polymers designed to circumvent these harsh processing conditions are described. Their application in multicomponent protein patterning will be discussed in the subsequent chapters.

## 2.1 Materials and Methods

### Materials

2-Nitrobenzyl alcohol, triethylamine, methyl methacrylate (MMA), poly(ethylene glycol) methacrylate (PEGMA,  $M_n=475$  Da), 2,2'-azobisisobutyronitrile, and 4-methoxyphenol were purchased from Sigma-Aldrich. Methacryloyl chloride was purchased from Lancaster Synthesis. Except as noted, all materials were used as received. Solvents were reagent grade or better.

### Synthesis and Characterization of Photoresist Terpolymers

*o*-Nitrobenzyl methacrylate (*o*-NBMA) was synthesized as previously reported (Figure 2. 1).<sup>75-77</sup> Briefly, 2-nitrobenzyl alcohol was dissolved in dichloromethane to a concentration of 50mg/mL with a stoichiometric amount of triethylamine. The sample was placed on ice and purged with nitrogen. Methacryloyl chloride was added dropwise with vigorous stirring, and the reaction was allowed to proceed for 15 hr at 4°C. *o*-NBMA was recovered by removal of the solvent and purified by silica-gel chromatography with 1:5 ethyl acetate:hexane vol:vol as a loading and running solvent.

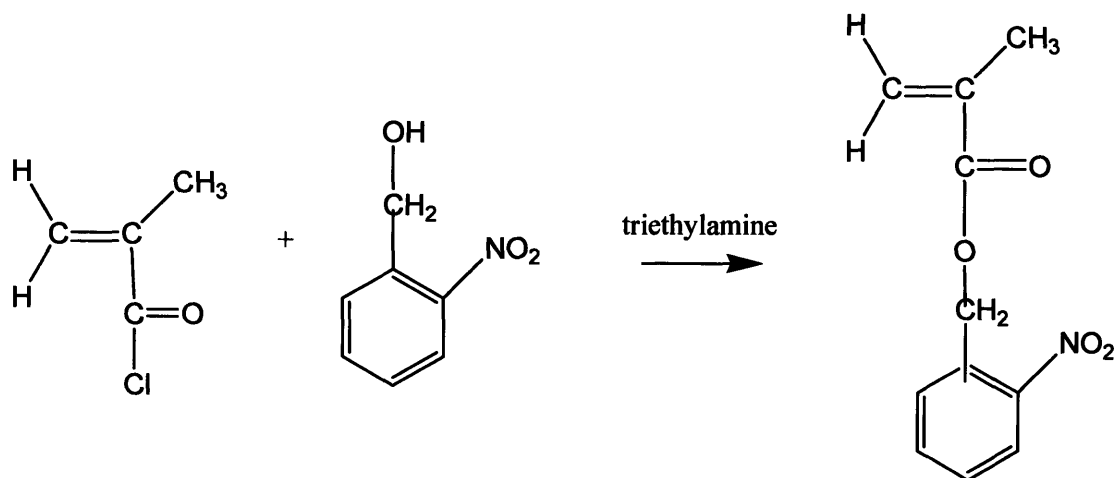


**Figure 2. 1** Synthesis of *o*-nitrobenzyl methacrylate (*o*-NBMA).

PNMP terpolymers were prepared by free radical co-polymerization of MMA, *o*-NBMA, and PEGMA in ethyl acetate or tetrahydrofuran. Monomers were mixed in different weight ratios to a total concentration of 30 mg/mL, purged with nitrogen for 15 min, and polymerized by the addition of 2,2'-azobisisobutyronitrile at a concentration of 300  $\mu$ g/mL. Polymerization was allowed to proceed at 64°C for 18 hr. The reaction was quenched by the addition of 4-methoxyphenol (5 wt% of the monomer feed) and then purified by sequential precipitations in hexane and diethyl ether. Solvent was removed from the polymers under vacuum at 60°C until dry, as determined by proton NMR.

Molecular weights of the terpolymers were determined by gel permeation chromatography (Viscotek GPCmax system with two G4000 HR columns and one G5000 HR column), and

$^1\text{H}$  NMR spectra were recorded on a Varian Unity 300MHz or Mercury 300MHz instrument in deuterated chloroform (Cambridge Isotope Laboratories) to assess polymer purity and final composition. A summary of the entire series of terpolymer compositions synthesized and their characterization data is provided in Table 1; specific compositions in the series have been labeled by capital letters for ease of reference.



**Table 2. 1 Composition and molecular weight of PNMP random terpolymer**

Sample	Solvent	Feed Composition (wt%)			Measured Composition (wt%)			$\bar{M}_n$	$\bar{M}_w$	PDI
		o-NBMA	PEG MA	MMA	o-NBMA	PEG MA	MMA			
A	THF	60	0	40	74.08	---	25.92	3776	6421	1.70
B	THF	60	10	30	61.22	7.02	31.77	11776	26757	2.27
C	THF	60	20	20	69.05	16.50	14.45	5722	11360	1.98
D	EtAc	60	30	10	57.52	27.30	15.19	8564	13470	1.57
E	THF	60	40	0	65.22	34.78	---	5850	12926	2.21
F	THF	40	0	60	58.49	---	41.51	5668	12017	2.12
G	EtAc	50	20	30	46.06	11.32	42.62	7193	15855	2.21
H	EtAc	40	20	40	39.00	10.00	51.00	13607	20589	1.51
I	EtAc	40	40	20	34.72	30.79	34.49	8268	15367	1.86
J	THF	30	60	10	32.78	58.84	8.38	7195	13360	1.86
K	THF	40	60	0	47.39	52.61	---	6277	12568	2.00
L	EtAc	30	70	0	29.77	70.23	---	6076	9725	1.60
M	THF	20	80	0	31.05	68.95	---	6800	11504	1.69
N	EtAc	25	50	25	19.32	41.50	39.18	8720	16416	1.88
O	EtAc	25	20	55	26.49	22.06	51.46	7714	13873	1.80
P	THF	20	0	80	24.20	---	75.80	8146	20079	2.46
Q	EtAc	100	0	0	100	---	---	6570	12443	1.89

## **Thin Film Dissolution Measurements.**

All studies relating to thin films were performed using single crystal silicon wafers. Silicon wafers were cleaned prior to use by washing in aqueous detergent with sonication, followed by rinsing with deionized water and drying under vacuum.

PNMP thin films were prepared by spin-coating 30 mg/mL solutions of polymer in dichloroethane (filtered with 200nm PTFE syringe filters) onto single crystal silicon substrates at 2000 rpm using a Model P6700 Spincoater from Specialty Coating Systems Inc. (Indianapolis, IN). Films were dried overnight under vacuum, followed by exposure to ultraviolet radiation (UVP Model UVG-54, Upland, CA;  $\lambda=254\text{nm}$ ,  $2250 \mu\text{W}/\text{cm}^2$ ) for 20 min, yielding the polyelectrolyte product (Figure 2. 4).

The immediate (within 5 min) solubility of the films was determined by sequential immersion in 150mM phosphate-citrate buffers of pH 5.0, 5.5, 6, 6.2, 6.4, 6.6, 6.8, 7.0, 7.4 and 8.0 in increasing order, until the film was visibly removed from the silicon by dissolution. After each wash, the film was rinsed with deionized water and dried with compressed air to visualize changes in the film thickness.

To examine the role of temperature, dissolution kinetics of UV-exposed films of polymer L were determined at 4°C, 23°C, and 37°C in phosphate-buffered saline (PBS, 10 mM phosphate) at a constant pH of 6.0. Similarly, to assess the effect of pH, polymer L

thin film dissolution experiments were carried out at a fixed temperature of 4°C, using phosphate buffers adjusted to pH's 6.0, 7.4, or 10.15. Films were incubated in 5 mL of PBS for times of 1, 5, 10, 15, 30, or 60 minutes, quickly rinsed, and dried with compressed air. Remaining film thicknesses were measured using a Gaertner Ellipsometer (Skokie, IL).

## 2.2 Synthesis of o-NBMA and PNMP

O-nitrobenzyl methacrylate was synthesized by reacting 2-nitrobenzyl alcohol with methacryloyl chloride in the presence of triethylamine (7.68ml) in dichloromethane (

Figure 2. 1) and purified by silica gel chromatography. The resulting <sup>1</sup>H NMR (Varian 300 MHz, CDCl<sub>3</sub>) spectrum was δ 1.99 (s, 3H), δ 5.60 (s, 2H), δ 5.65 (s, H), δ 6.2 (s, H), δ 7.62 (m, 3H), δ 8.10 (d, H) (Figure 2. 2).

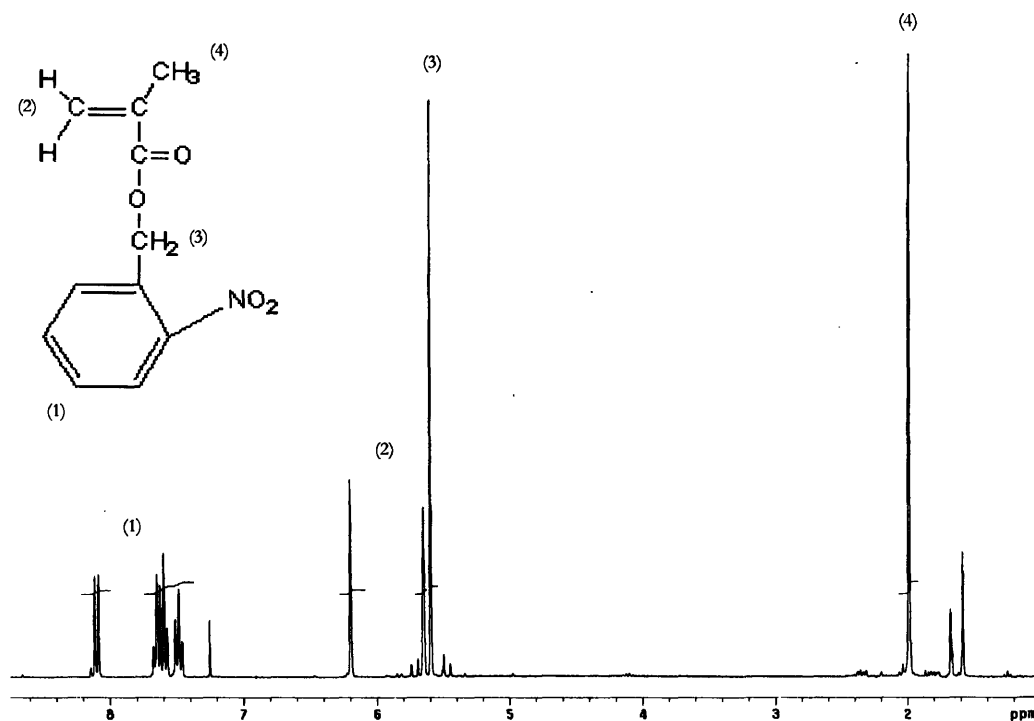


**Figure 2.2** <sup>1</sup>H NMR spectra of o-NBMA.

We synthesized a series of PNMP terpolymers covering a wide range of the ternary composition space of o-NBMA:MMA:PEGMA. Polymers were characterized by NMR spectroscopy (a representative <sup>1</sup>H NMR spectra is shown in Figure 2.3) and gel permeation chromatography to assess their purity, composition, and molecular weight distributions. A list of the photoresist polymers synthesized and their physical characterization is given in Table 2.1. Because monomer composition alone was a large variable space to explore, we sought to minimize variation of terpolymer molecular weight in these studies. As is

evident from the data in Table 1, we sought to confine our studies to terpolymers with relatively low molecular weights in the range ~5-10 KDa and PDIs ~1.5-2.0.

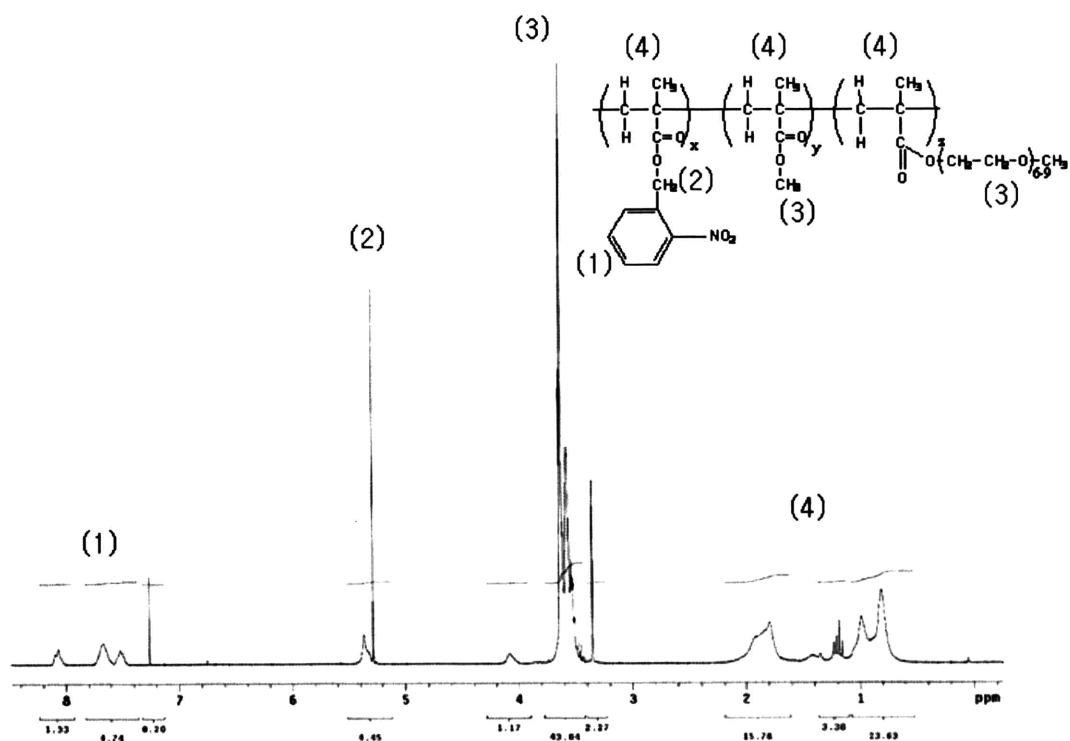


**Figure 2. 3 A representative <sup>1</sup>H NMR spectra of PNMP comprised of 36% o-NBMA, 40% MMA, and 24% PEGMA by weight.**

## 2.3 Composition Dependence of UV-Exposed Photoresist Film

### Solubility

Reactions initiated by ultraviolet exposure of the oNBMA moiety yield free methacrylic acid groups attached to the polymer backbone (Figure 2. 4). This photochemical change alters the solubility behavior of PNMP thin films due to changes in both the interaction between the terpolymer chains and between the polymer and solvent. To examine how the composition of the terpolymer controls its solubility behavior, we analyzed trends in the dissolution behavior of thin films of the entire series of terpolymers reported in Table 2. 1. In these experiments, the immediate solubility (measured over 5 min) of PNMP thin films (thicknesses 130-170 nm) in aqueous phosphate buffers as a function of pH at 20°C was assayed by visual inspection. The results are summarized in the ternary composition diagrams of Figure 2. 5. Each terpolymer is denoted by a circle at the appropriate point in the triangular composition space; the color of each circle denotes the threshold buffer pH above which rapid complete dissolution of thin films of that composition was observed.

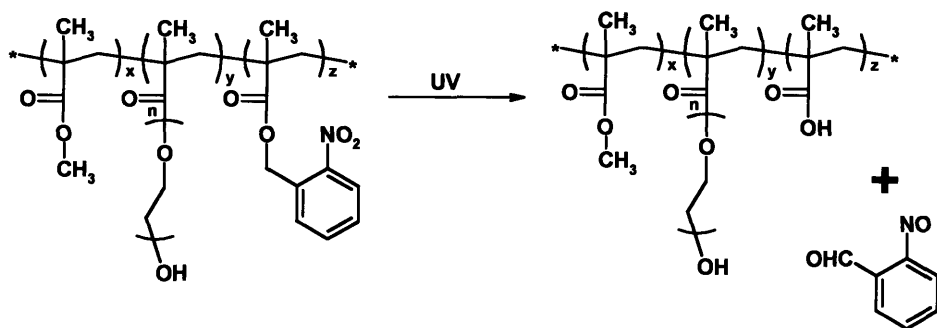


**Figure 2. 4 Photorearrangement of PNMP terpolymer**

We first examined the solubility of as-cast, non-irradiated PNMP thin films (Figure 2. 5A). As expected, the unexposed terpolymers, bearing the largely nonpolar o-nitrobenzyl protecting groups and lacking any strongly ionizable components, showed no aqueous solubility except for terpolymer compositions with relatively high PEGMA contents. The three water-soluble compositions examined here (polymers K, L, and M) showed no pH-dependence to their solubility, and dissolved in buffers with pH ranging from 2 to 10. We have sketched a hypothetical phase boundary separating the aqueous-insoluble compositions (region I) from aqueous-soluble compositions (region II); this boundary is shown stretching toward a composition of 50:50 wt:wt MMA:PEGMA along the lower plot axis, as prior studies have shown that poly(MMA-r-PEGMA) forms water-soluble polymers at approximately this composition.<sup>78,79</sup>

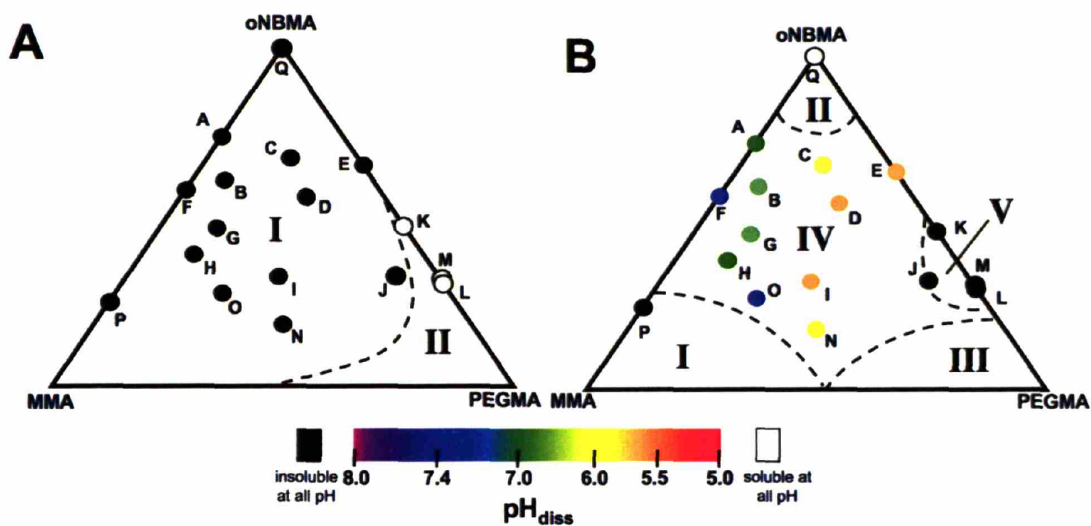


**Figure 2.5** Aqueous solubility of (A) as-cast and (B) UV-exposed thin films of PNMP terpolymers with compositions listed in Table 2. 1. Relative distances of each point from the triangle vertices denote the weight fraction of each component in the terpolymer; colors indicate the critical pH ( $pH_{diss}$ ) at which rapid complete dissolution of thin films immersed in 150 mM phosphate-citrate buffer was observed. The dashed lines denote hypothetical boundaries between regions of distinct solubility behavior.

After UV exposure, the solubility behavior of PNMP thin films was dramatically altered. To aid discussion, on Figure 1B we have superimposed hypothetical boundaries separating the composition space into five regions of solubility behavior observed for the UV-exposed thin films. In terpolymer compositions with a high MMA content (region I), the hydrophobicity of the methyl methacrylate groups was expected to dominate the film properties; in agreement with this notion, UV-exposed films of terpolymer P with a MMA content of 75 wt% were insoluble in aqueous buffers regardless of pH. In contrast, poly(o-NBMA) homopolymer (region II) rapidly dissolved in aqueous solutions across a



range of pH's after UV exposure. This result was expected, based on the known solubility behavior of poly(methacrylic acid)—the product of UV-exposed poly(o-NBMA).<sup>80</sup>

Similarly, terpolymers composed of very high contents of PEGMA (placed in region III) are expected to be entirely water-soluble, independent of the buffer pH, analogous to poly(PEGMA).<sup>81,82</sup>

In addition to these readily understood properties at the extremes of composition space, we found two other regions of solubility behavior at intermediate compositions. For terpolymers in region IV, the aqueous solubility of UV-exposed PNMP films exhibited a threshold pH for dissolution. The color scale shown in Figure 1B indicates the critical pH required for rapid film dissolution ( $\text{pH}_{\text{diss}}$ ). Below  $\text{pH}_{\text{diss}}$ , films were stable, while above this threshold value films dissolved within seconds. The solubility of these films depends on at least two competing factors, namely, the relative hydrophobicity (determined by the MMA content), and the pH-dependent degree of ionization of the deprotected methacrylic acid groups. As the pH is raised, ionization of the MAA groups on the PNMP chains will lead to fewer intermolecular hydrogen bonds and increased intra- and inter-chain ionic repulsion (discussed further below), favoring dissolution of the film. The threshold pH for dissolution of films in region IV was seen to vary across the composition diagram; for fixed fractions of o-NBMA, PNMP terpolymers with more MMA exhibited a higher  $\text{pH}_{\text{diss}}$  than

terpolymers with more PEGMA. This trend is illustrated by the data in Figure 2. 6, where the threshold pH for dissolution of the UV-exposed films is plotted as a function of PEGMA content for terpolymers with fixed amounts of o-NBMA (~35 or 60 wt%).

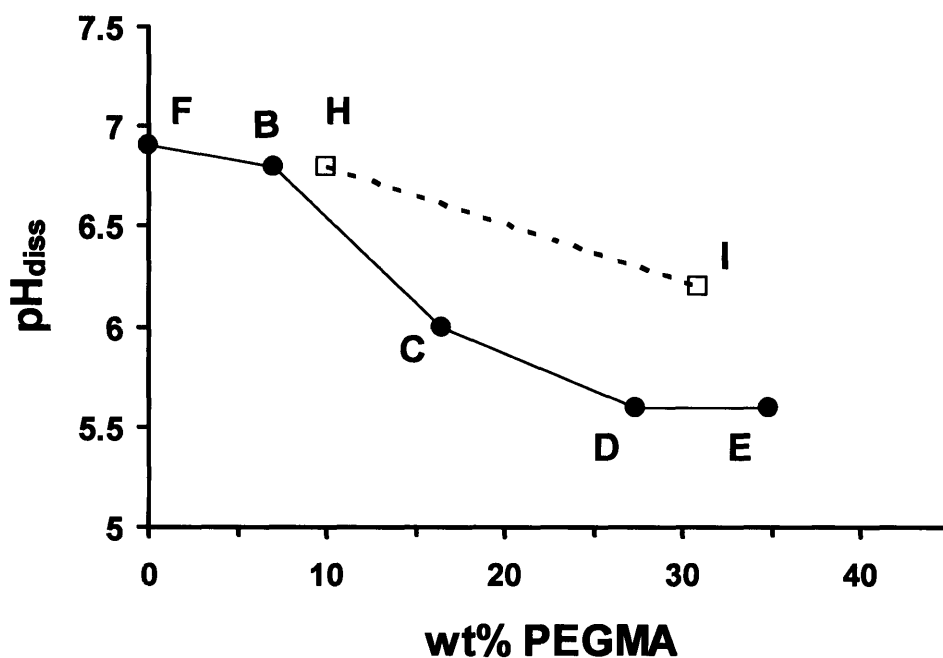


**Figure 2. 6 Trends in the pH-dependent solubility of exposed PNMP thin films as the amount of PEGMA is increased for approximately constant (□) 60 wt% or (•) 35 wt% o-NBMA. Experiments performed in triplicate, testing pH in small-unit intervals (0.2-0.5 units) all returned the values shown.**

Because the UV-exposed PNMP terpolymers have both MAA and PEGMA repeat units, the potential for significant intra- and inter-molecular hydrogen bonding exists. PMAA has been shown to complex with various Lewis bases, including N-isopropylacrylamide<sup>83</sup>

and vinyl(pyrrolidone).<sup>84</sup> These hydrogen bonding interactions are pH-dependent due to the weakly acidic nature of PMAA ( $pK_a \sim 6.5$ ).<sup>80,85</sup> Notably, a number of prior studies have characterized H-bonding interactions between MAA-containing polymer chains and PEG in the context of poly(MAA-g-PEGMA) hydrogels<sup>86-88</sup> and intra-molecularly between PMAA and PEG.<sup>89-92</sup> Peppas and coworkers have demonstrated the use of PMAA-PEG hydrogen bonding to amplify the collapse of pH-responsive P(MAA-g-PEGMA) hydrogels, where deswelling of the gel at low pH due to de-ionization of MAA and subsequent expulsion of counter ions/water is coupled to the onset of interchain hydrogen bonding.<sup>87,88,93</sup> In the present PNMP films immersed in low pH buffers, protonated methacrylic acid groups of the exposed PNMP chains should be capable of significant hydrogen bonding among themselves or with surrounding PEG and MMA repeat units, which will favor insolubility of the film. In a somewhat analogous experimental situation, multilayer self-assembled thin films comprised of alternating layers of PEG and PMAA have been shown to disintegrate in aqueous solutions above a critical pH; in these systems, FTIR analysis of thin films permitted direct demonstration of the importance of hydrogen bonding in this threshold solubility phenomenon.<sup>90,91</sup> Although this work and other prior studies have demonstrated infrared spectroscopy as a means to characterize the degree of hydrogen bonding in thin films,<sup>87,90-92</sup> we found that the composition of the PNMP

terpolymers precluded clear, quantitative evaluation of the amount of hydrogen bonding in these films, due to the many overlapping signals in the carbonyl and ether stretching regions of the IR spectrum of these materials.

The ability of ether oxygens in the PEGMA side chains to hydrogen bond with protonated MAA groups complicates the role of increased PEGMA content on the solubility of PNMP films: increased PEGMA content in the terpolymer chains favors film dissolution due to the hydrophilic nature of the PEG side chains, while simultaneously providing more sites for hydrogen bonding with available MAA groups (promoting film stability).

Interestingly, we found that for terpolymer compositions in region V, hydrogen bonding of the MAA groups to the PEG side chains impeded dissolution of UV-exposed thin films across a wide range of pH. In the short term ( $t < 5$  min), exposed polymer films of approximate composition (wt:wt) 35% o-NBMA and 65% PEGMA were entirely insoluble across the pH range 2-10 at 20°C. As shown in Figure 1A, polymers K, L and M were water soluble prior to UV exposure, indicating that for a narrow range of terpolymer compositions, a solubility transition on UV exposure opposite that of the majority of composition space can be observed: polymers K, L and M transition from initially water-*soluble* to water-*insoluble* over limited time periods (kinetically stable), ranging from minutes to days depending on the solution conditions (discussed below). Polymer J, which

we show on the border of regions IV and V, was a composition that was water insoluble in the as-cast state, but also exhibited transient film stability after UV exposure.

The transient stability of UV-exposed thin films with compositions in region V was revealed by experiments measuring the kinetics of film dissolution as a function of temperature and pH. To examine the role of temperature, dissolution kinetics of UV-exposed films of polymer L were determined at 4°C, 23°C, and 37°C in phosphate-buffered saline (PBS, 10 mM phosphate) at a constant pH of 6.0. Similarly, to assess the effect of pH, polymer L thin film dissolution experiments were carried out at a fixed temperature of 4°C, using phosphate buffers adjusted to pH's 6.0, 7.4, or 10.15. Films were incubated in 5 mL of PBS for times of 1, 5, 10, 15, 30, or 60 minutes, quickly rinsed, and dried with compressed air. Remaining film thicknesses were measured using a Gaertner Ellipsometer (Skokie, IL). Figure 2. 7 shows the dissolution kinetics of UV-exposed thin films of polymer L over time at 4°C, when exposed to phosphate buffered solutions of three different pH's (Figure 2. 7A) and at constant pH with varying temperature (Figure 2. 7B). Each film had a measured initial thickness of ~160 nm. The dissolution rate of these films increased with increasing pH and temperature, as expected if hydrogen bonding is responsible for the observed transient film stability; at pH 6.0 and 23 or 37°C, films were completely dissolved within thirty minutes. Notably, these measurements reveal that the

half-life of UV-exposed films of polymer L can be modulated ~7-fold from ~13 min to 90 min by simply moving from pH 7.4 to pH 6.0 at a constant temperature of 4°C. In summary, PNMP thin films over the majority of composition space are water-insoluble but become soluble at a critical pH upon UV exposure, while for a narrow range of compositions, a reverse transition from initial solubility to kinetic stability is observed.

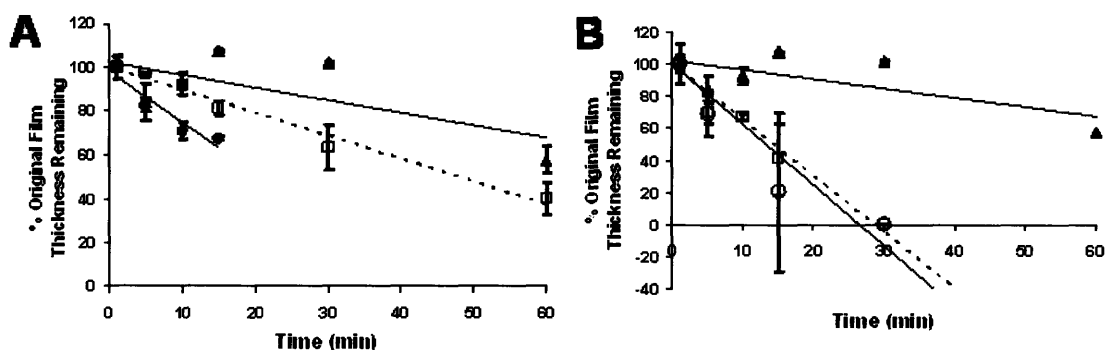


**Figure 2. 7 (A) Dissolution of exposed thin films of Polymer L at 4°C in PBS adjusted to (●) pH 10.15, (□) pH 7.4, and (▲) pH 6.0. (B) Dissolution of exposed thin films of Polymer L in PBS pH 6.0 at (▲) 4°C, (□) 23°C, and (○) 37°C. Note that the 30 min points for 23°C and 37°C overlap at zero thickness. Measurements shown are averages of triplicate samples ± S.E.M. Lines shown are a guide to the eye.**

### **3 Two-component Photolithographic Protein Patterning under Mild Aqueous Conditions**

The temperature- and pH-dependent solubility of UV exposed PNMPs described in the last chapter enables these polymers to be used as photoresists that can be processed under extremely mild aqueous conditions. Polymers in region V of the terpolymer composition space (Figure 2. 5B) can be used as a ‘negative-tone’ photoresist, which becomes insoluble in a developing solution upon UV exposure, due to their transient insolubility in water upon UV exposure. On the other hand, a ‘positive-tone’ photoresist, which dissolves in a developing solution after UV exposure, can be developed tuning polymers in region IV of the terpolymer composition diagram (Figure 2. 5B). Building on these results, in this chapter two different methods for dual-streptavidin patterning based on the physicochemical properties of PNMP polymers studied in detail in Chapter 2 are presented based on negative- and positive-tone lithography, respectively. Each approach requires different types of substrates for patterning, thus these two different approaches are useful in

complementary applications. We demonstrated the patterning processes followed by general strategies for immobilizing commercially available proteins on the patterned surfaces.

### **3.1 Materials and Methods**

#### **Materials**

Succinic anhydride, N-methylimidazole, 4-dimethylaminopyridine (DMAP), N,N'-Dicyclohexylcarbodiimide (DCC), 1,4-dioxane, 3-aminopropyl-triethoxy-silane (APTS), poly(allylamine) hydrochloride (PAH,  $M_w \sim 70,000$ ), and poly(acrylic acid) (PAA,  $M_w=250,000$  Da) were purchased from Sigma-Aldrich. EZ-link Biotin-PEO-amine and 1-ethyl-3-(3-dimethylaminopropyl)carbodiimide hydrochloride (EDC), 2-Hydroxyazobenzen-4'-Carboxylic Acid(HABA) and avidin were purchased from Pierce. Texas-Red- or Alexa-Fluor 647-conjugated streptavidin (SAv-TR and SAv-AF647, respectively) were purchased from Molecular Probes. Fluorescein isothiocyanate (FITC)-labeled SAv and anti-ICAM-1 (clone 3E2) were purchased from BD Bioscience. Anti-Human Fc $\gamma$  polyclonal antibody was purchased from R&D Systems.



## Synthesis and Biotinylation of Photoresist Terpolymers

Polymer L synthesized and characterized in Chapter 2 was used as negative-tone photoresist. For a positive-tone photoresist, a PNMP terpolymer with composition o-NBMA: MMA: PEGMA = 43: 35: 22 by weight (characterized by  $^1\text{H}$  NMR) was synthesized by free radical polymerization described in Chapter 2. This terpolymer had a molecular weight of 9,600 Da and polydispersity index of 1.78 (determined by GPC). This polymer belongs in region IV of the terpolymer composition diagram (Figure 2. 5B), which exhibits pH-dependent solubility in water upon UV exposure. This polymer is designated hereafter as polymer H' since it has similar composition and pH-dependent solubility as polymer H.

Hydroxyl termini of PEGMA units in the polymer H' were carboxylated for further functionalization (Figure 3. 1). Briefly, the photoresist polymer (9 g) and succinic anhydride (5.52 g) were added to a three-neck flask with condenser, and 250 ml anhydrous dichloroethane was cannulated. The photoresist polymer was observed to quickly dissolve while the succinic anhydride remained suspended in the solvent. The mixture was degassed 15 minutes by bubbling nitrogen, then N-methylimidazole (72  $\mu\text{l}$ ) was added dropwise with stirring. The reaction was carried out for 15 hours at 65 °C. The carboxylated photoresist was purified by sequential precipitations in diethyl ether and 5

vol% aqueous HCl. The polymer was washed 18 hours by stirring in 5 vol% aqueous HCl, recovered by filtration, and dried at 60 °C *in vacuo*.

The carboxylated photoresist polymer was biotinylated by coupling amine-PEO-biotin to the carboxylic acid groups of the modified photoresist terpolymer. Carboxylated photoresist (2 g), biotin-PEO-amine (30 mg), DMAP and DCM (19 ml) were added to a round-bottom flask. DCC (20 mg) was dissolved in 1ml of DCM and immediately added dropwise to the reaction mixture while stirring. The reaction mixture was stirred for 18 hours at room temperature, and the resulting biotinylated polymer was recovered by precipitation in diethyl ether.

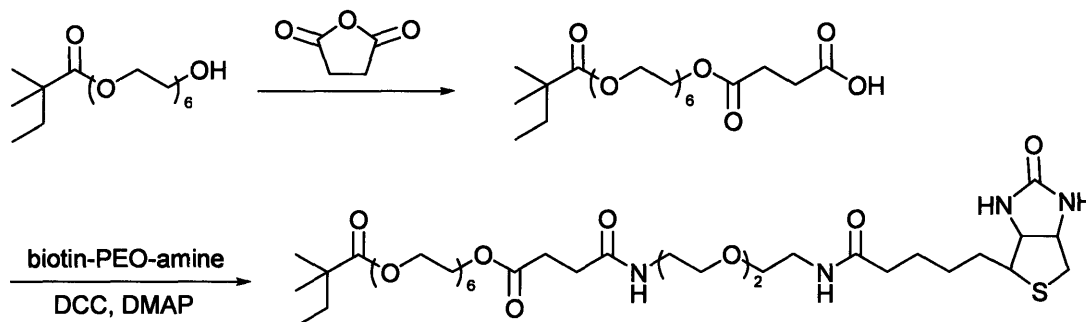


**Figure 3. 1 Biotinylation of hydroxyl termini of PEGMA.**

Biotinylation was confirmed by detecting specific binding of FITC-labeled streptavidin (SAv-FITC) to thin films of the functionalized photoresist. Biotinylated or

non-biotinylated (carboxylated) photoresist films were prepared by spincoating on glass coverslips. Each substrate was incubated in SAV-FITC solution (5  $\mu\text{g}/\text{ml}$  in PBS) for 30 min, followed by rinsing with water. Bound SAV-FITC was detected on each surface by measuring fluorescence intensity using a Zeiss epifluorescence microscope equipped with a Roper Scientific CoolSnap HQ CCD camera. The ratio of background-corrected fluorescence from films of biotinylated film PR to non-biotinylated PR was  $\sim 60$ .

### **Substrate Preparation**

Either single crystal silicon wafers (for film thickness measurements) or #1 glass coverslips (for microscopy) were used for substrates. Substrates were cleaned by either concentrated sulfuric acid or 10M sodium hydroxide, and subsequently coated with either PAH or APTS to introduce positive charge on the surfaces.

For PAH coating, substrates were immersed in concentrated sulfuric acid overnight, rinsed with copious amount of deionized (DI) water, dipped in PAH solution (1mg/ml, pH=4.5) 30 min, washed with DI water, and dried by air blowing. For APTS coating, substrates were sequentially etched with 10M aqueous sodium hydroxide (10 min sonication), washed with ethanol (5 min sonication), and finally incubated in a 1 wt% aqueous dilution of the APTS at 20°C (30 min). The silane solution was stirred for 20 min

prior to incubation with the substrates and passed through a 200 nm Nylon filter. After rinsing with DI water, the aminosilane-conjugated slides were dried at 95°C under vacuum. For the protein patterning with negative-tone photoresist, APTS-coated substrates were further functionalized by adsorption of PAA and conjugation of biotin to a fraction of the adsorbed PAA acid groups. Briefly, PAA was adsorbed to the silanized substrates by incubation of the slides for 20 min in a 1 wt% solution of the polymer in deionized water followed by water rinsing. Biotin was conjugated to the PAA-coated substrates by incubation of the coverslips in an aqueous solution of biotin-PEO-amine (500 µg/mL) and EDC (5 mg/mL) for 4 hr. EDC activation simultaneously provided covalent coupling of the adsorbed PAA to the underlying aminosilane layer. All substrates were stored at 20°C until used.

### **Protein Patterning with a Negative-tone Photoresist**

Biotinylated, PAA-modified substrates were prepared as described above. PNMP terpolymer (Polymer L) was spincoated onto the substrates from a 30 mg/ml solution in either dichloroethane or water. Following a 20 min UV exposure ( $\lambda=254$  nm, 2250  $\mu\text{W}/\text{cm}^2$ ) through a TEM grid as a crude photomask (TedPella; Redding, CA), the slide was briefly rinsed with DI water, dissolving the unexposed regions of the PNMP film and

exposing biotin groups conjugated to the underlying PAA. Alexa-Fluor 647-conjugated streptavidin (SAv-AF647) diluted to 1  $\mu\text{g}/\text{mL}$  in PBS pH 6.0 was incubated over the surface for 30 min at 4°C. Dissolution of the UV-exposed regions of terpolymer film remaining on the substrate was achieved by transferring the slide to 37°C in PBS, pH 7.4. After 2 hr, the slide was removed and rinsed with PBS. Finally, SAv-TR was diluted to 1  $\mu\text{g}/\text{mL}$  in PBS pH 7.4 and allowed to bind to the slide for 30 min at 20°C. The slide was rinsed one final time with PBS.

### **Protein Patterning with a Positive-tone Photoresist**

Biotinylated PNMP terpolymer (polymer H', o-NBMA: MMA: PEGMA = 43: 35: 22 by weight , Mn = 9,600 Da and PDI = 1.78) dissolved in 1,4-dioxane (3 wt%) was spincoated onto the substrates. A PNMP thin film was irradiated through a TEM grid, developed with PBS, re-exposed in the absence of a photomask. SAv-TR was deposited (10  $\mu\text{g}/\text{ml}$  in PBS pH 6.0, 30 min at 4°C), followed by washing with pH 7.4 PBS, and finally SAv-FITC, the second SAv, was immobilized (10  $\mu\text{g}/\text{ml}$  in PBS pH 6.0, 30 min at 4°C) by using the newly exposed biotin groups.

## **Fluorescence Microscopy**

Fluorescence images of the patterned surfaces were acquired on a Zeiss Axiovert 200 microscope equipped with a Roper Scientific CoolSnap HQ CCD camera and processed with Metamorph software.

## **HABA Assay**

HABA solution was prepared by adding 24.2 mg HABA and 0.1 ml of 1 M NaOH to 9.9 ml of DI water. If HABA did not completely dissolve, another 0.1ml of 1 M NaOH was added. HABA solution was filtered with 0.2 $\mu$ m syringe filter to remove small aggregates and stored at 4°C. HABA/avidin solution was prepared by adding 2 mg of avidin and 120  $\mu$ l of HABA solution to 3.88 ml of PBS. Absorbance at 500 nm ( $A_{500}$ ) of 180 $\mu$ l HABA/avidin solution was recorded ( $A_{500}$  of HABA/avidin solution should be 0.9-1.3). Then, 20  $\mu$ l of biotinylated protein solution (typically 0.5-1.0 mg/ml in PBS) was added to a HABA/avidin solution containing cuvette. Equilibrium  $A_{500}$  of HABA/avidin/sample solution was recorded and divided by 0.9 to correct dilution by protein solution. By subtracting dilution-corrected  $A_{500}$  of HABA/avidin/sample from  $A_{500}$  of HABA/avidin, the contribution of  $A_{500}$  change by biotinylated sample was calculated. This value was calibrated by known concentration of biotin-PEO-amine

solution (typically, 10  $\mu\text{M}$ , 2.5  $\mu\text{M}$ , and 1  $\mu\text{M}$ ), and number of biotin per each protein was calculated.

### **3.2 Dual Streptavidin Patterning Using Negative-tone Photoresist**

As described in Chapter 2, thin films of polymers K, L, and M were rapidly soluble ( $t < 1$  min) in water, but after UV exposure their rate of dissolution was significantly decreased and modulated by mild shifts in temperature and pH. We harnessed this tunable rate of dissolution to pattern two proteins on a surface in predefined patterns, following the procedure outlined in Figure 3. 2. In this approach, an aminosilane-coated glass substrate was modified with a high density of biotin groups by adsorbing poly(acrylic acid) to the surface followed by covalent conjugation of biotin-PEG-amine to the acid groups of the PAA (Figure 3. 2, step a); simultaneously, acrylic acid groups of the PAA were covalently linked to the surface amines. This provided a thin hydrophilic layer of biotin groups presented on short PEG tethers (2-3 ethylene glycol units per tether) on the substrate. This surface was then overlaid with a thin film of PNMP (polymer L) by spincoating. The PNMP film was patterned by UV exposure through a mask (steps b, c). On subsequent rinsing with deionized water (step d), the unirradiated regions immediately dissolved, exposing the underlying biotin layer, while the irradiated portions of the film were retained.

At this stage, a first protein (SAv-AF647) was immobilized via the available biotin groups, by incubation of the substrate in a PBS pH 6.0 protein solution at 4°C—a pH and temperature chosen to retard dissolution of the UV-exposed masking film remaining on the surface (step e). The 30 min incubation of SAv-AF647 with the substrate was observed to be sufficient for full saturation of the exposed biotin molecules. The substrate was then moved to a bath of PBS, pH 7.4 at 37°C to accelerate the dissolution and removal of the remaining exposed portions of the original PNMP film (step f). After 2 hrs, the slide was removed and a second protein (SAv-TR) was immobilized to the previously masked biotin groups within the UV-exposed regions of the substrate (step g). Note that starting at step d, the surface remained fully hydrated during processing.



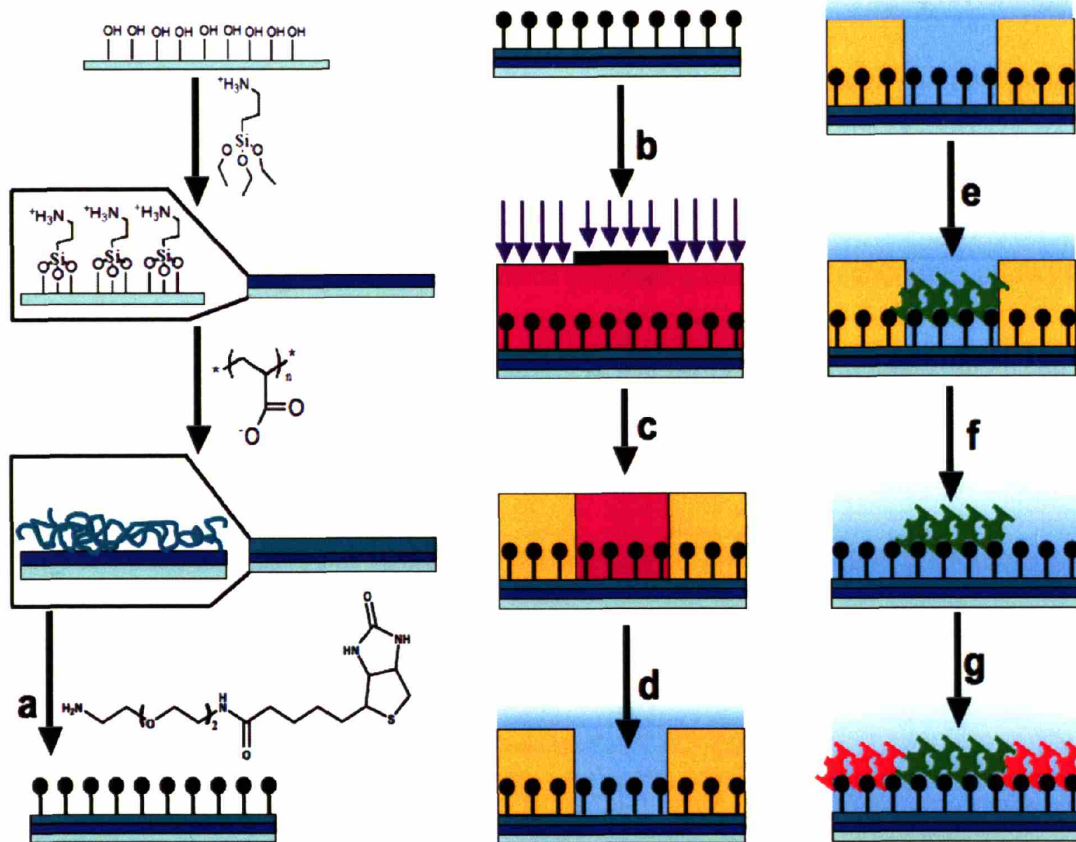


**Figure 3. 2 Two component patterning of proteins on a surface.** Glass slides are first functionalized by grafting 3-aminopropyl-triethoxysilane and adsorbing poly(acrylic acid) (left column). Labeled arrows: (a) EDC coupling of biotin-PEG-NH<sub>2</sub> to PAA in water. (b) Spincoating of polymer L from dichloroethane or water. (c) UV irradiation through photomask. (d) Removal of unexposed polymer by rinsing with water. (e) Conjugation of Streptavidin-AlexaFluor 647 in PBS, pH6.0 at 4°C. (f) Removal of exposed polymer by incubation in PBS, pH 7.4 at 37°C. (g) Conjugation of Streptavidin-Texas Red in PBS, pH 7.4 at 20°C.

Representative fluorescence images of two-component protein patterns achieved by this process are shown in Figure 3. 3. Each protein was successfully isolated to its target domain, as seen by the intensity contrast between the target and non-target regions for both

proteins. The pattern shown was obtained for a PNMP thin film cast by spincoating from dichloroethane. Interestingly, because polymer L is water-soluble prior to UV exposure, we were able to obtain surface protein patterns of similar quality using PNMP films prepared by spincoating aqueous solutions of polymer L onto glass substrates, allowing organic solvents to be disposed with altogether in the film processing/patterning (data not shown). While we show here immobilization of two different streptavidin molecules, it is straightforward to extend this strategy to pattern two different biotinylated molecules, using streptavidins as protein bridges to the surface, as previously demonstrated by Sundberg et al.<sup>40</sup>

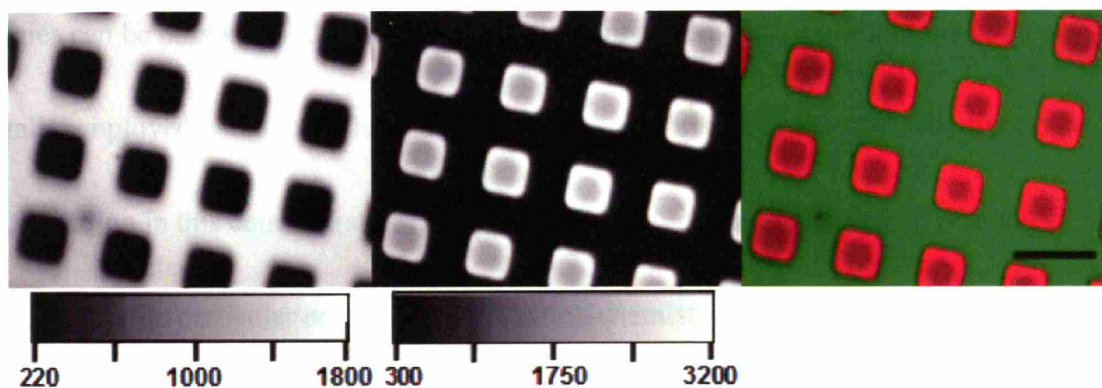


**Figure 3.3** Grayscale fluorescence intensity images of glass substrates patterned using a film of PNMP terpolymer L. (A) SAV-AF, immobilized first, and (B) SAV-TR, immobilized second after masking film lift-off (grayscale meters denote fluorescence intensity scale). (C) False-color overlay of fluorescence images from A and B. Scale bar = 50  $\mu\text{m}$ .

The procedure we have developed allows protein processing to be carried out entirely in the aqueous phase at a range of pH and temperatures that are compatible with living and biological systems. For the simple binary pattern shown here, ultraviolet radiation was used only once, prior to the immobilization of any protein. Additionally, the entire process can be completed within a few hours, allowing for same-day fabrication and utilization, and patterning can be achieved with inexpensive benchtop contact printing methods.

Patterning with PNMP terpolymer L requires that the substrate must not exhibit a positive surface charge, in order to avoid electrostatic interactions between the exposed polymer and surface and ensure complete removal of the resist from the surface during development, exposing the surface-bound biotin molecules. However, a variety of strategies can be pursued to alter surface charge that may allow this methodology to be generally employed. While we have utilized biotin-streptavidin interactions for protein immobilization in this demonstration, the photolithographic strategy described here does not depend on the particular protein immobilization chemistry used, and could be adapted to other covalent or non-covalent immobilization schemes.

### **3.3 Dual Streptavidin Patterning Using Positive-tone Photoresist**

Photolithographic process described in the previous section using PNMP terpolymer L

overcame many limitations of conventional photolithography processes for patterning proteins. However, high PEGMA contents (typically > 50% by weight), an essential element for transient physical crosslinking of polymer thin film upon UV exposure by hydrogen bonding formation between PEG and carboxylic acid, significantly reduce the glass transition and mechanical stiffness of this terpolymer. As a result, this photoresist is not compatible with vacuum contact printing necessary for fabricating small features (< 10 $\mu$ m). To deal with this issue, we developed an alternative approach using a terpolymer in region IV of the PNMP composition diagram (Figure 2. 5B) taking advantage of these materials' pH-dependent solubility. A PNMP terpolymer H', described in Materials and Methods section as a positive-tone photoresist, was used for this new method.

### **In Situ Polyelectrolyte Bilayer Formation**

In typical photolithographic processes, a photoresist is used only as a selectively-removable physical barrier for transferring 2D patterns present in a mask to a substrate. Here we took advantage of the polyelectrolyte nature of the UV-exposed photoresist to combine development of the water-soluble photoresist with *in situ* electrostatic self-assembly, by using a cationic substrate to capture polyanions generated at the film-substrate interface by the photochemical reaction (Figure 3. 4). PAH was adsorbed on glass

coverslips or silicon substrates (dry thickness 3 nm), and a 130 nm thick film of photoresist polymer was subsequently spin-coated over the polycation monolayer. photoresist films were then exposed under a UV lamp (254 nm, 2.25m W/cm<sup>2</sup>) for various times and rinsed with PBS for 1 minute. The thickness of dried films (measured by ellipsometry) after UV exposures longer than 10 min was 6-10 nm, a thickness characteristic of single polyelectrolyte bilayers,<sup>95,96</sup> indicating dissolution of the majority of the polymer but retention of a layer significantly thicker than the initial PAH film (Figure 3. 5). We hypothesized that this remaining film was a polyelectrolyte bilayer formed *in situ* at the photoresist/PAH interface by electrostatic cross-linking of newly-formed carboxylic acid groups to amines on the PAH during UV exposure. To test this hypothesis, photoresist-coated substrates were UV-exposed for 15 minutes through a TEM grid as a crude photomask, rinsed with PBS, then dipped in a solution of cationic methylene blue dye. Only UV-exposed regions were stained (Figure 3. 6), suggesting that a polyelectrolyte bilayer with a net negative surface charge had formed between photogenerated polyanions and the underlying polycation.

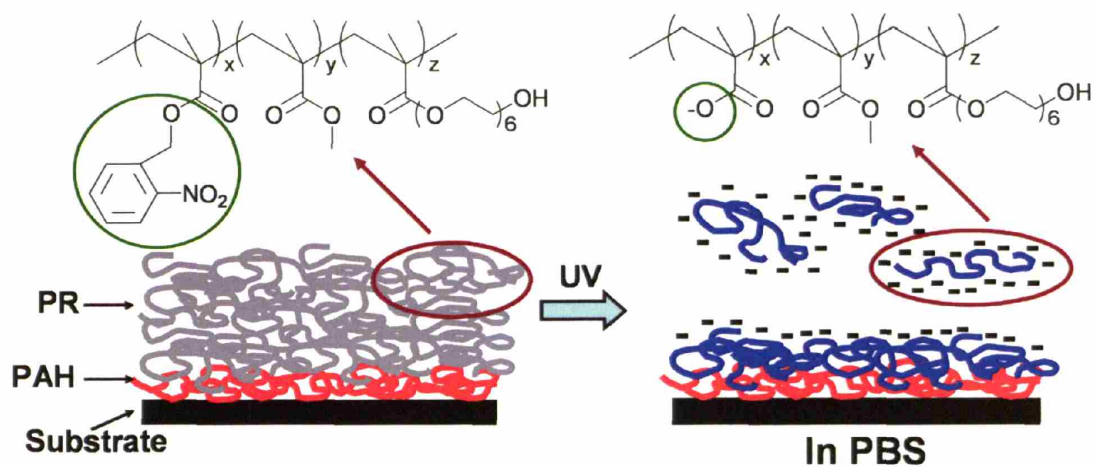


Figure 3. 4 Chemical structure of terpolymer H', and its mechanism for *in situ* polyelectrolyte bilayer formation.

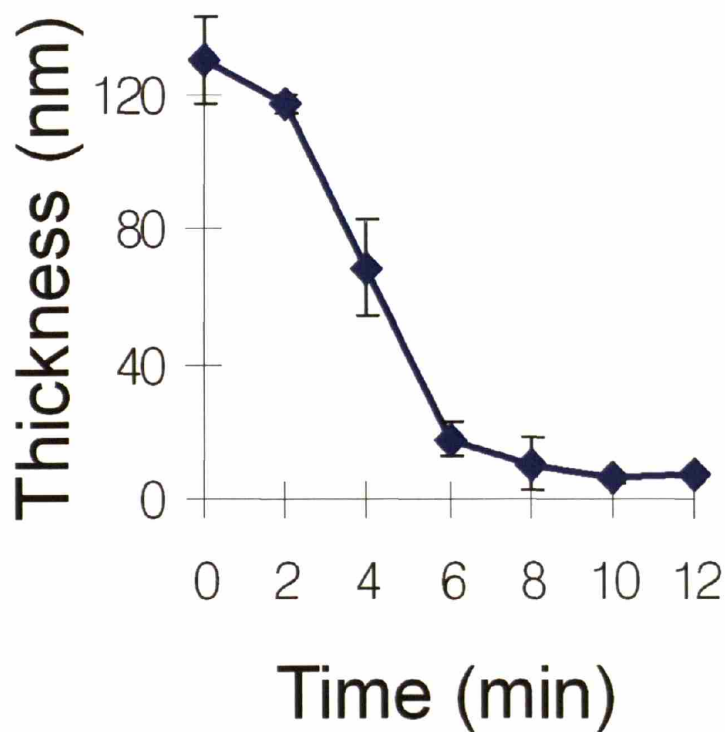
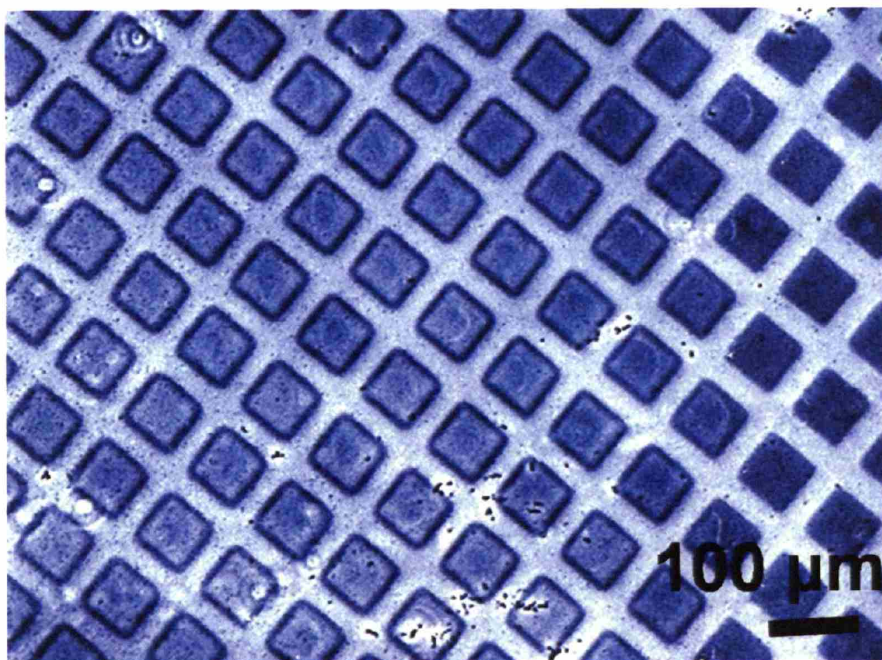


Figure 3. 5 UV exposure time vs. remaining terpolymer H' film thickness.



**Figure 3. 6** UV-exposed, developed, and methylene blue-stained photoresist surface

### **pH Dependent Solubility of UV-exposed Terpolymer H'**

The degree of ionization of weak polyelectrolytes is sensitive to pH, and thus the stability of a polyelectrolyte film in aqueous buffers can likewise exhibit pH dependence.<sup>91,97</sup> Protonation of the carboxylic acid groups on our UV-exposed photoresist at reduced pH made the polymer insoluble in acidic aqueous buffers. As shown in Figure 3. 7, photoresist-coated substrates exposed to UV for 15 min followed by rinsing with phosphate buffer (10mM sodium phosphate) for 1 minute exhibited dramatically different

final thicknesses depending on the pH of the buffer solution. At low pHs, the UV-exposed films were stable in phosphate buffer. However, at a pH above 6.6, UV-exposed films dissolved to a constant thickness (6~10 nm) characteristic of the polyelectrolyte bilayer structure.

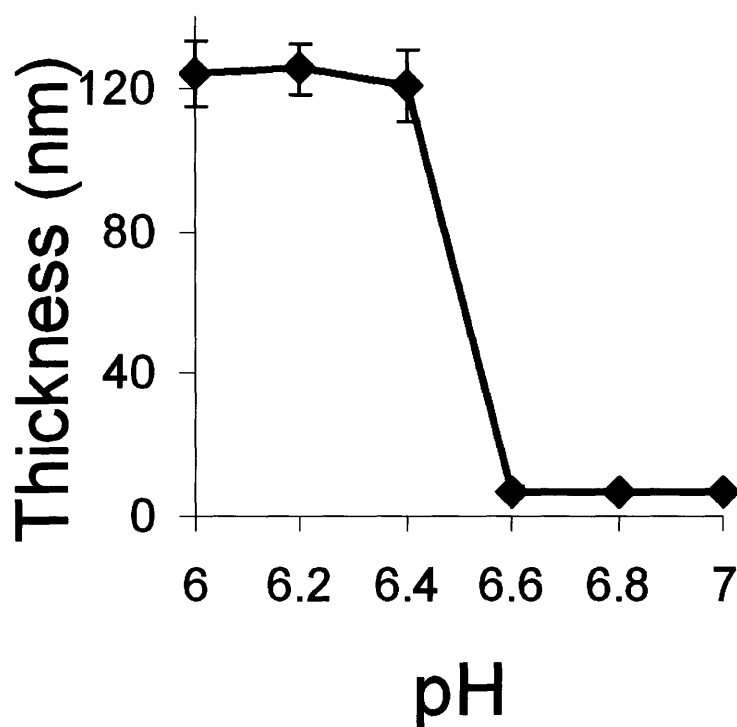


**Figure 3. 7 pH-dependent solubility of the UV-exposed photoresist.**

### **Dual SAv patterning**

The unique combination of characteristics outlined above – chemical patterning on UV exposure, and pH-sensitive aqueous development – can be exploited to create



multicomponent patterns of surface-immobilized proteins without exposing the proteins to UV irradiation or any solvents other than gentle near-neutral biological buffers. Using the biotinylated PNMP terpolymer H', assembly of two different fluophore-coupled proteins (Texas-Red-conjugated streptavidin (SAv-TR) and fluorescein isothiocyanate-conjugated streptavidin (SAv-FITC)) was achieved following the scheme shown in Figure 3. 8: A photoresist film spincoated atop a PAH monolayer was exposed to UV through a photomask (Figure 3. 8A) and developed by rinsing with PBS (Figure 3. 8B). In this step, a thin layer of the exposed polyelectrolyte resist remains bound to the cationic substrate (Figure 3. 9). Next, the substrate was re-exposed to UV without a photomask (Figure 3. 8C), and streptavidin Texas-Red (SAv-TR) in pH 6.0 PBS was adsorbed (Figure 3. 8D). Since the UV-exposed photoresist is not soluble in pH 6.0 PBS, the masking film of UV-exposed photoresist remained intact during this step, and SAv-TR bound to the entire surface (data not shown). By subsequently washing the surface with pH 7.4 PBS, the exposed photoresist film masking the 'background' was dissolved, removing SAv-TR on that region and exposing underlying biotin groups in the retained polyelectrolyte bilayer (Figure 3. 8E). Finally, SAv-FITC was adsorbed on the newly exposed region (Figure 3. 8F).

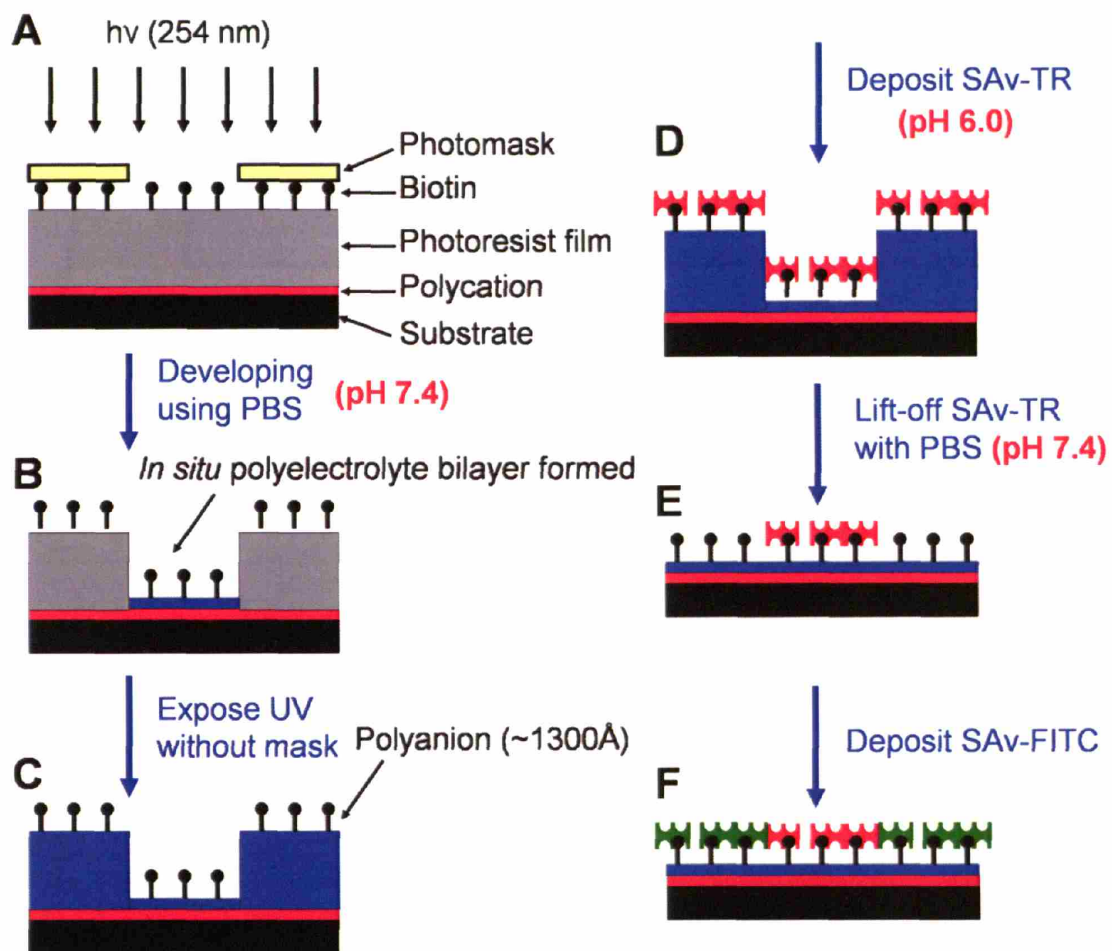


**Figure 3. 8** Schematic procedure of dual streptavidin patterning using positive-tone biotinylated photoresist. The chemical structure of the PNMP photoresist and film after UV exposure and development (B) is further illustrated in Figure 3. 9.

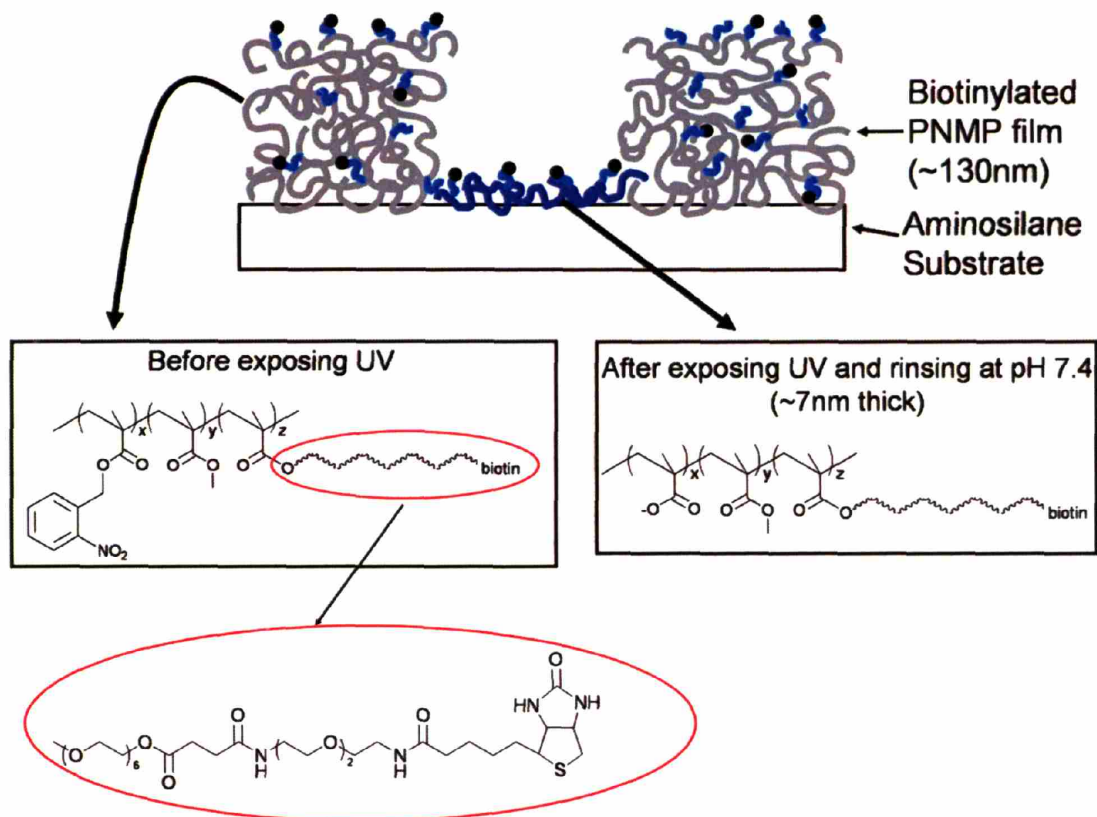


**Figure 3. 9** Chemical structure of PNMP before and after UV exposure, and schematic structure of patterned surface shown in Figure 3. 8B. The patterned film schematic illustrates the presence of biotinylated PNMP side chains throughout the PNMP thin film. When UV-exposed regions are developed with near-neutral PBS, the bulk of the film dissolves, except for a thin molecular layer of the resist copolymer, which remains electrostatically bound to the underlying aminosilane substrate.

Fluorescence micrographs of a typical surface prepared by this process are shown in Figure 3. 10. Figure 3. 10A and B were taken from the same surface with excitation/emission filters matching Texas-Red and FITC, respectively; Figure 3. 10C shows an overlay of the two images. The red- and green-channel images show the clear segregation of the two proteins to their respective regions.

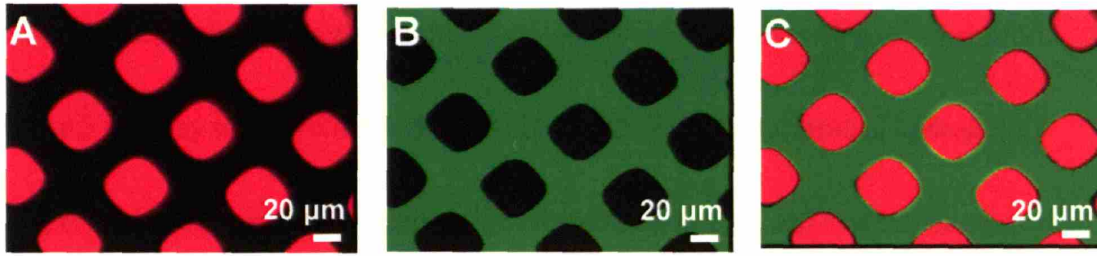


**Figure 3. 10** Fluorescent microscopy of dual streptavidin patterned surface. (a) SAV-TR fluorescence, (b) SAV-FITC fluorescence, (c) overlay.

Protein binding to the dual-patterned surface shown in Figure 3 was analyzed using fluorescence intensity measurements. The fluorescence contrast of protein (average ratio of the background-corrected fluorescence intensity from the protein-bearing regions to the intensity from the ‘clear’ regions) in the first region (SAV-TR shown in Figure 3a and the overlay Figure 3c) was  $5.74 \pm 0.74$ , while that of protein patterned into the second region (SAV-FITC, Figure 3b and 3c) was  $4.82 \pm 1.10$ . These measured contrasts compare well with other quantitative reports of patterning single proteins on glass<sup>43</sup> or silicon.<sup>39</sup> The similar values of contrast measured for the first protein (patterned by a lift-off step which makes any cross-contamination of the protein outside its target region unlikely) and the second protein suggests that the degree of cross-contamination is small.

### **Non-specific Binding Assay**

In any protein immobilization strategy, protein may bind to a surface by both specific

mechanisms (i.e., designed covalent bonding or ligand-receptor binding) and nonspecific mechanisms (e.g., by uncontrolled hydrophobic/van der Waals associations, hydrogen bonding, or ionic bonding to the surface). For the present photoresist system, these avenues of protein binding are schematically illustrated in Figure 3. 11: streptavidin may be specifically bind to surfaces by the high affinity binding of the protein to biotin groups presented at the ends of PEG tethers of the photoresist (Figure 3. 11A) or may nonspecifically adsorb directly to the various chemical moieties available at the photoresist surface (Figure 3. 11B). To measure the relative amounts of specific and non-specific protein bound to patterned biotinylated photoresist films, we quantified the fluorescence from Texas-Red-labeled streptavidin (SAv-TR, Molecular Probes) immobilized on patterned surfaces. Biotinylated photoresist films on PAH-coated glass coverslip substrates were exposed with a grid pattern as illustrated in Figure 3. 8A –C. Labeled streptavidin ( $0.2\mu\text{M}$  in PBS pH 6.0) was then incubated 30 min over patterned surfaces prepared as in Figure 3. 8D, and the ‘background’ of the pattern was cleared by lift-off using pH 7.4 PBS (Figure 3. 8E). To measure nonspecific binding, surfaces were alternatively immersed in  $0.2\mu\text{M}$  solutions of SAv-TR (in PBS pH 6.0) that had been pre-incubated with  $200\mu\text{M}$  biotin-PEO-amine for 1 hour on ice to block its biotin-binding pockets. Samples were then imaged on a Zeiss Axiovert 200 epifluorescence microscope

equipped with a Roper Scientific CoolSnap HQ CCD camera and 40X oil immersion objective (NA 1.3). The resulting fluorescence micrographs for surfaces incubated with SAV-TR or blocked SAV-TR are shown in Figure 3. 11C and D, respectively. Background fluorescence was measured on each sample prior to incubation with streptavidin. The amount of non-specific binding was estimated by comparing the background-corrected average fluorescence intensity of surfaces exposed to blocked or unblocked streptavidin. The fluorescence intensity from blocked SAV-TR surfaces was only  $6.6 \pm 3.0\%$  of the fluorescence intensity from surfaces patterned with the unblocked protein. In addition to reducing nonspecific protein binding due to formation of a PEG 'brush',<sup>98,99</sup> ligands tethered by PEG linkers are known to have greater biological activity than physically adsorbed ligands<sup>100</sup> due to the dynamic nature of the PEG linker in solution and the reduced possibility of denaturation by direct physical contact with the underlying surface.

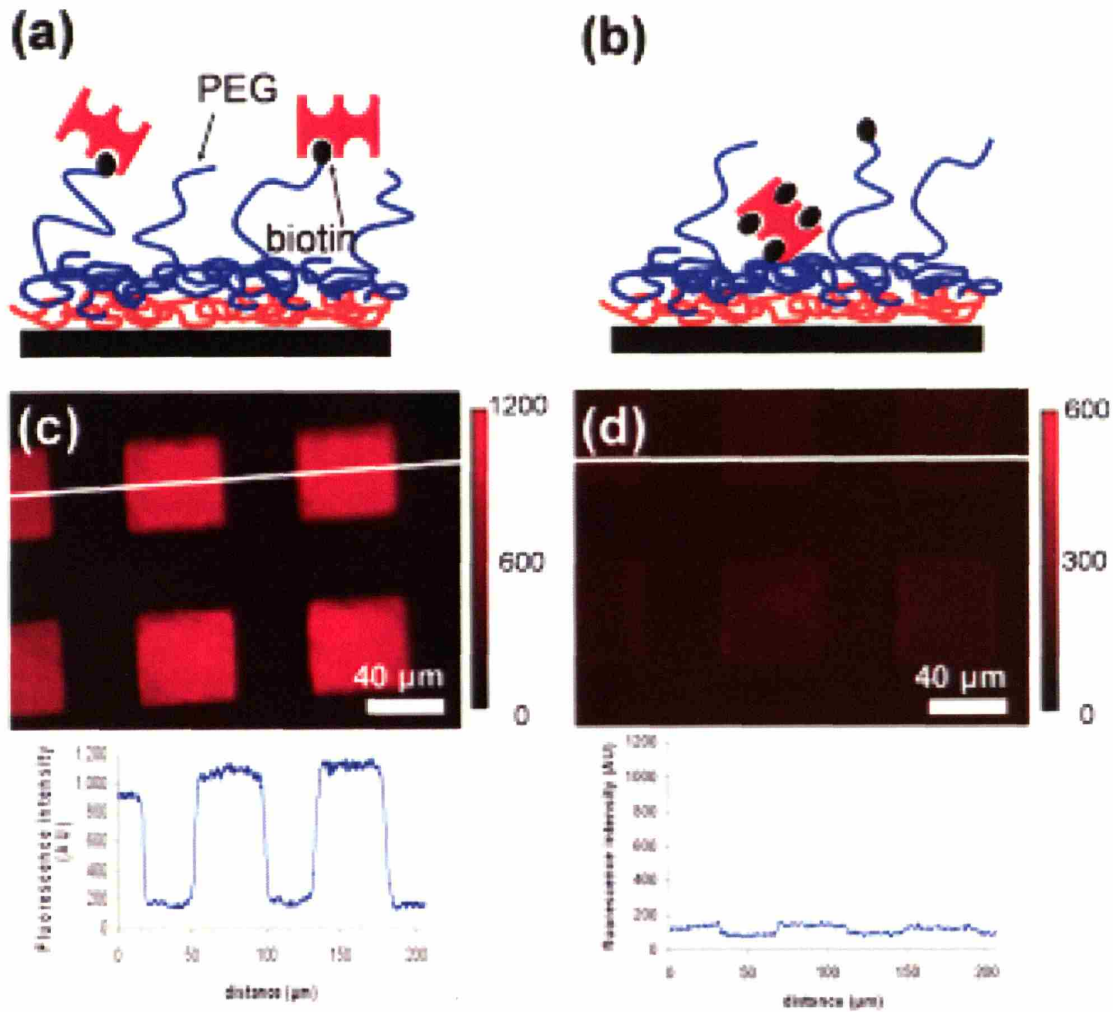


**Figure 3. 11 A and B. Schematic of specific (biotin-mediated) (A) and nonspecific (B) streptavidin binding to photoresist surfaces. C and D. Fluorescence images and corresponding fluorescence intensity linescans of surfaces patterned with SAv-TR (C), or blocked SAv-TR (D). Note the different intensity scales used in the two fluorescence images to make the weak pattern definition observed in the case of nonspecific binding visible to the eye.**

### Positive-tone Patterning Strategy Conclusions

By utilizing the unique combination of photo- and pH-sensitivity of the described photoresist, 2-component protein patterning was achieved under conditions which avoid

exposing proteins to conditions outside the narrow range of physiological pH, ionic strength, and temperature where their stability is greatest. Singly-biotinylated proteins (some available commercially) are readily prepared by recombinant DNA technology, and using the process outlined in Figure 3. 8, such proteins can be readily immobilized into two different regions of a substrate with high fidelity by simply incubating the surface with each protein following streptavidin in steps 4 (Figure 3. 8D) and 6 (Figure 3. 8F). This patterning strategy should have resolution limits similar to standard photolithography; we have been able to fabricate surfaces with 2  $\mu\text{m}$  features using simple benchtop vacuum contact printing methods (demonstrated in subsequent chapters). Further, patterning of multiple protein arrays in 2D patterns should be readily achieved using contact aligners common in the silicon processing industry by step-and-repeat patterning.<sup>43</sup>

### **3.4 Protein Ligand Immobilization on streptavidin patterned surfaces**

In previous sections, we have discussed two different strategies for two-component streptavidin patterning. These streptavidin patterned surfaces can be general platforms for presenting proteins or other biological ligands via streptavidin-biotin binding, one of the most popular interactions in bioconjugation chemistry due to its extremely high affinity and



avidity ( $K_d \sim 10^{-15}M$ ).<sup>101</sup> Biotinylated proteins are commercially available, or readily prepared by using biotinylation reagents reacting with the surface amines of proteins.

Another commercially available prosthetic group on recombinant proteins is fusions of the Fc region of human IgG molecules. In this section, we demonstrate approaches for immobilizing biotinylated or Fc-fused proteins; however, these methods can be readily extended to other functional groups. The stability of these ligands non-covalently attached to patterned surfaces was also analyzed.

### **Biotinylated Antibody Immobilization and Visualization**

Commercially available biotinylated antibodies were directly immobilized on SAV-bearing patterned surfaces by SAV-biotin bridges (Figure 3. 12). Since commercially available biotinylated antibodies contained 5-12 biotins per molecules (determined by HABA assay), biotins unbound to the surface SAV could be accessed by additional soluble SAVs (Figure 3. 12C). These excess biotins available on the surface-tethered antibodies could be utilized for visualizing the surface-immobilized antibodies: Fluorescent SAV-AF647 was adsorbed on SAV presenting surfaces (Figure 3. 12A) or biotinylated antibody-immobilized surfaces (Figure 3. 12B) and the fluorescence intensity from each condition was compared. The fluorescence from biotinylated antibody-bearing surfaces ( $2715 \pm 52$ ,

arbitrary unit) was about eight times greater than that from SAV-only surfaces ( $321 \pm 32$ , arbitrary unit).

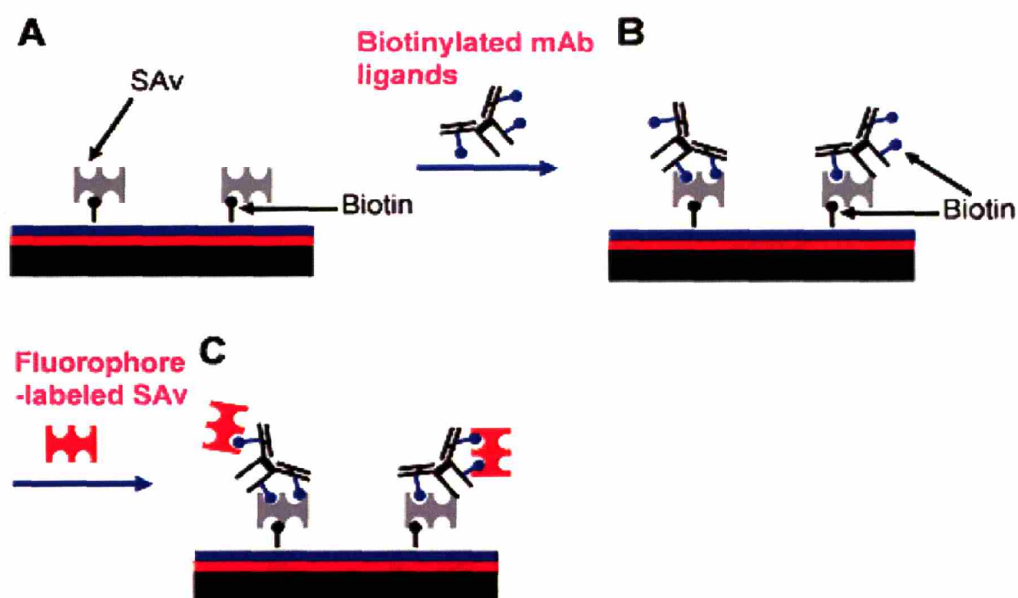


Figure 3. 12 Immobilization and visualization of biotinylated monoclonal antibodies.

### Fc Fusion Recombinant Proteins Immobilization

Many native protein ligands are commercially available in the form of chimeric proteins fused with the Fc region of human IgG. In this study, we used Fc fusion recombinant ICAM-1 (ICAM-1/Fc), but this strategy can be generally applied to other Fc fusion proteins. First, biotin-conjugated anti-human Fc antibodies were attached to patterned surfaces (Figure 3. 13B), and subsequently ICAM-1/Fc molecules were

immobilized by antibody-antigen interactions (Figure 3. 13C). Successful surface tethering of the ICAM-1/Fc chimera was confirmed by detection with a FITC-conjugated anti-ICAM-1 antibody as shown in Figure 3. 13D.

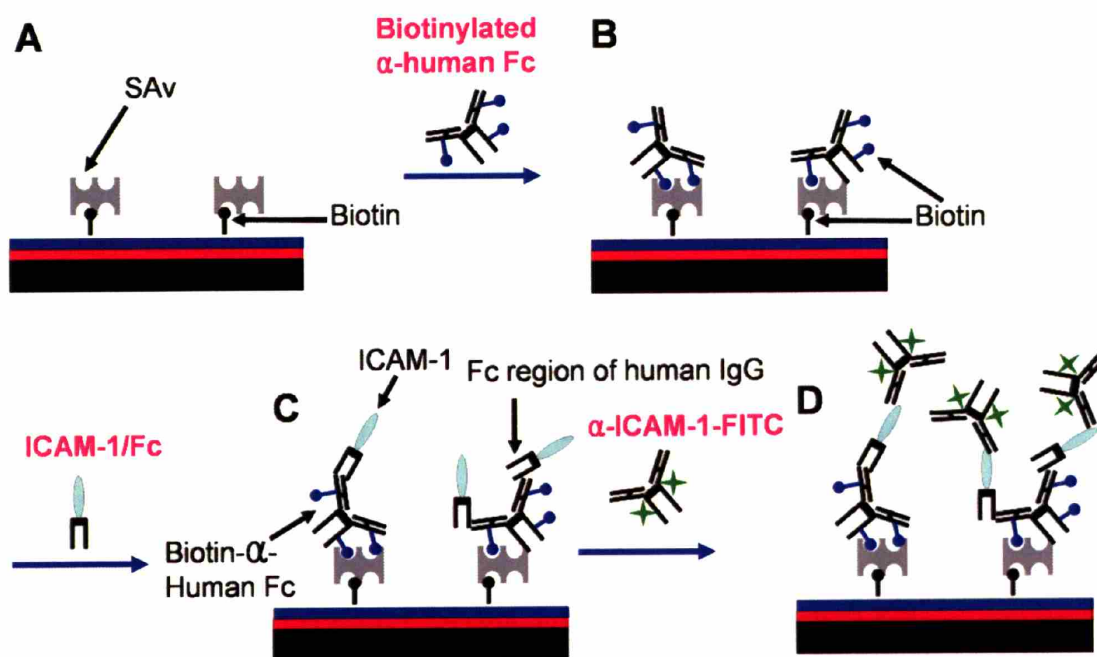


Figure 3. 13 Immobilization and visualization of ICAM-1/Fc chimera.

### Stability of Non-covalently Immobilized Ligands

Since the strategies just described immobilized ligands to patterned surfaces via non-covalent interactions, we next analyzed their stability. Streptavidin-biotin interactions have an extremely low  $K_d$  ( $\sim 10^{-15}M$ ), which corresponds to a half-life of weeks.<sup>101</sup> However, in the case of antigen-antibody interactions,  $K_d$  can vary from  $10^{-5}M$  to  $10^{-12}M$ .<sup>102</sup>

Given the much lower affinity of these interactions, the dissociation rate of ICAM-1/Fc from polyclonal anti-Human Fc surfaces was assayed using FITC-conjugated anti-ICAM-1 and fluorescence microscopy. Biotinylated anti-human Fc $\gamma$  was patterned in a square array of 6 $\mu$ m spots via the procedure outlined in Figure 3. 8: For protein assembly in pH 6.0 buffer, SAV was bound to the biotinylated patterned resist (10  $\mu$ g/ml, 30 min), followed by biotinylated anti-Fc (10  $\mu$ g/ml, 30 min). The anti-Fc proteins were then tagged with Alexa 647-conjugated SAV (10  $\mu$ g/ml, 30 min), to provide a normalized measure of the amount of ICAM-1/Fc binding sites per spot in the array (Figure 3. 14A, left panel). Finally, by increasing the pH to 7.4, the UV-exposed PNMP in the pattern background region was removed (Figure 3. 8E), and the background region was blocked with 10 $\mu$ g/ml SAV in blocking buffer (PBS pH 7.4 containing 2 wt% bovine serum albumin and 0.05 wt% tween 20). To measure the kinetics of ICAM-1 release from these surfaces, ICAM-1 was loaded on patterned anti-Fc-bearing slides at staggered time-points by incubation of the slides in 5  $\mu$ g/ml ICAM-1/Fc in blocking buffer for 30 min (Figure 3. 14A, middle panel). Surfaces were then rinsed and immediately incubated in PBS pH 7.4 at 37°C for a defined release time  $t$  ranging from 0 to 24 hrs. After 24 hours total 'release time', each of the ICAM-1-loaded substrates were washed 3X and incubated with FITC-conjugated anti-ICAM-1 (10  $\mu$ g/ml in blocking buffer, 30 min at 4°C). After rinsing with PBS 5X, both

FITC and Alexa fluorescence images were acquired for each sample and the ratios  $I_{FITC}/I_{Alexa\ 647}$  of the green to far red fluorescence intensities from the patterned spots (after background subtraction) were computed. Calculation of the intensity ratio normalized for small differences in the amount of ICAM-1 binding sites (and thus initial amounts of ICAM-1 loading) on different spots of the array. The fraction of ICAM-1 remaining bound to the surface pattern as a function of time was calculated as:

$$\text{Fraction ICAM - 1 remaining} = \frac{\left( \frac{I_{FITC}}{I_{Alexa}} \right)_t}{\left( \frac{I_{FITC}}{I_{Alexa}} \right)_{t=0}},$$

where the numerator represents the intensity ratio after a release time  $t$  and the denominator the intensity ratio for freshly prepared ICAM-1-loaded surfaces. This relationship for the fraction of surface-bound ICAM-1 as a function of time is plotted in Fig. 8B. The half-life of ICAM-1 binding obtained by fitting this data to an exponential decay was 55 hours.

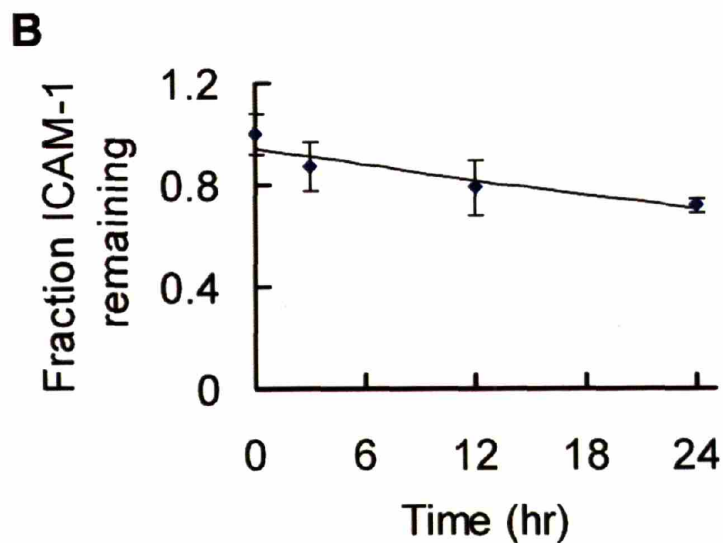
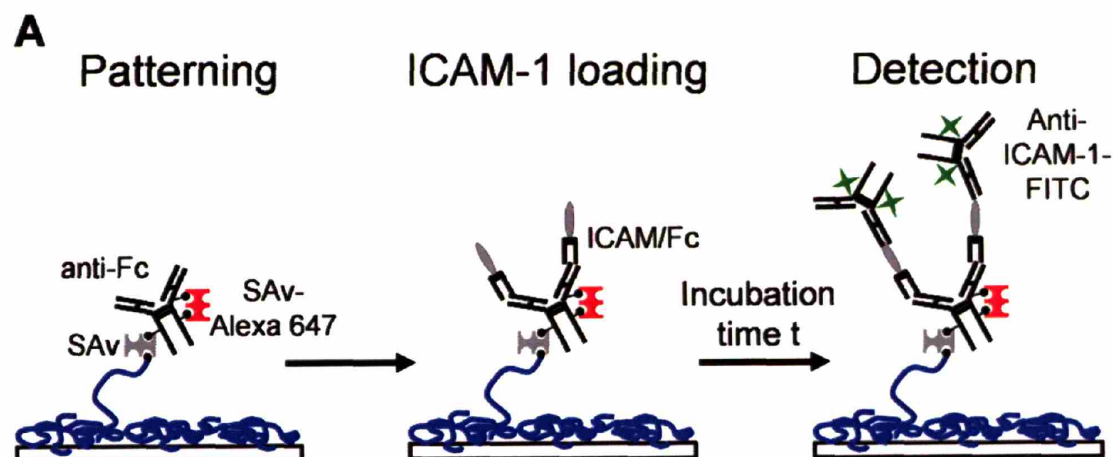


**Figure 3. 14 Measurement of patterned ICAM-1 surface stability. (A) Schematic of labeling and detection procedure for assaying the stability of immobilized ICAM-1. (B) Fraction of surface-bound ICAM-1 remaining as a function of time, as determined by the fluorescence ratio  $[I_{\text{FITC}}/I_{\text{Alexa-647}}]_t/[I_{\text{FITC}}/I_{\text{Alexa-647}}]_{t=0}$  for ICAM-1-loaded patterned surfaces incubated at 37°C in PBS pH 7.4. Data shown are ave  $\pm$  stdev of 5-6 independent samples at each time-point.**

## **4 Fabrication of ‘Immunological Synapse Arrays’ and T Cell Responses to These Patterned Surfaces**

In this chapter, the fabrication of ‘immunological synapse arrays’ using the positive-tone photolithographic strategy developed in Chapter 3 and the cellular responses of T cells on the fabricated surfaces are presented. The immunological synapse arrays mimic the local microenvironments of lymph nodes where sparsely distributed antigen presenting cells (APCs) displaying foreign peptides on their MHC molecules are surrounded by other cells expressing high levels of adhesion molecules to promote T cell motility. As schematically shown in Figure 4. 1, the immunological synapse arrays are composed of a square array of ‘activation sites’ that present T cell receptor (TCR) ligand surrounded by an ‘adhesion field’ presenting immobilized adhesion ligand. The activation sites were patterned with diameters less than the diameter of T cells (~10  $\mu\text{m}$ ), and thus the spatial distribution of TCR ligands and adhesion ligands that a T cell recognized on an activation

site would have a distribution mimicking the mature synapse structure formed on APCs.

First, to recapitulate the highly motile nature of T cells in vivo, we tested two different ligands of LFA-1, a T cell integrin molecule, and their effect on T cell adhesion and migration was compared. Using the optimal ligand, ICAM-1, we next fabricated immunological synapse arrays by combining the patterning and ligand immobilization methods discussed in Chapter 3 and characterized. Then, the responses of T cells on the synapse surfaces were studied by video microscopy and Enzyme-Linked Immunosorbent Assay (ELISA). T cell responses from early activation events including migration halt and calcium mobilization to late activation events such as synapse resolution, cell division, and cytokine secretion were demonstrated.

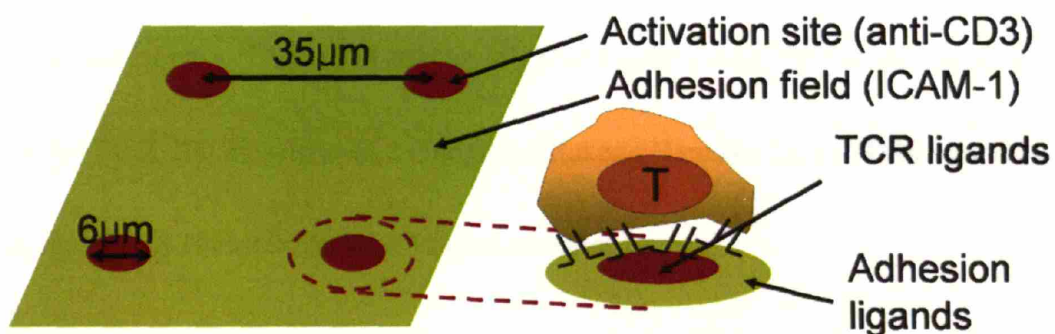


Figure 4. 1 Schematic of immunological synapse array surface pattern.



## 4.1 Materials and Methods

### Materials

PNMP was synthesized, biotinylated and characterized as described in Chapter 2. This resist material is a random terpolymer with composition o-nitrobenzyl methacrylate (o-NBMA):methyl methacrylate (MMA):poly(ethylene glycol) methacrylate (PEGMA) = 36:37:27 by weight, number average molecular weight: 6,500 g/mol, and polydispersity index of 1.78.

Proteins used for surface patterning and visualization were as follows: biotinylated anti-CD3 $\epsilon$  (145-2C11; BD bioscience), recombinant mouse ICAM-1/Fc chimera (R&D systems, ICAM-1 fused with the Fc-region of Human IgG), polyclonal biotinylated goat (or mouse) anti-human IgG Fc $\gamma$  (Jackson ImmunoResearch), streptavidin-Alexa 647 (Molecular Probes), <sup>125</sup>I-labeled streptavidin (GE Health Care), FITC-conjugated anti-ICAM-1 (3E2; BD biosciences), biotinylated Rat and Hamster IgGs (BD bioscience), Cy2-conjugated anti-Hamster (Jackson Immunoresearch).

### Preparation of cells

OT-II (Jackson Laboratories)<sup>103</sup> and 5C.C7 (Taconic)<sup>104</sup> CD4<sup>+</sup> T cell blasts were prepared by stimulation of splenocytes from transgenic mice with 100 $\mu$ g/ml of ovalbumin

(for OT-II) or 1 $\mu$ M of moth cytochrome c peptide (amino acids 88-103, ANERADLIAYLKQATK; for 5C.C7). Cells were maintained in complete RPMI medium (RPMI-1640 medium with 10% FCS, 2mM L-glutamine, 50 $\mu$ M  $\beta$ -mercaptoethanol, penicillin and streptomycin) and used on days 5-7.

### **Time-lapse microscopy**

Time-lapse fluorescence microscopy was performed on a Zeiss Axiovert 200 epifluorescence microscope equipped with a heated stage (maintaining 37°C and 5% CO<sub>2</sub>) and a Roper Scientific CoolSnap HQ charge-coupled device (CCD) camera. T cells were loaded with the intracellular Ca<sup>++</sup> indicator fura-2 AM (Molecular Probes) by incubation with 20  $\mu$ M fura for 20 min at 37°C, to permit simultaneous morphology and intracellular Ca<sup>++</sup> imaging<sup>21</sup>. Activation sites of the patterns were visualized by Alexa 647-SAv bound to the activation site anti-CD3 molecules. For each experiment, fura-loaded T cell blasts were seeded onto patterned synapse arrays and time-lapse microscopy was immediately initiated, with images recorded in 35 sec intervals for 40 min. At each time interval, 4 images were recorded in rapid succession (in a 4 sec time span): differential interference contrast (DIC), fura fluorescence (340nm and 380nm excitation), and activation site fluorescence. Images were acquired using METAMORPH software (Universal Imaging) and

analyzed using either METAMORPH or VOLOCITY (Improvision).

### **Fabrication of immunological synapse arrays**

Glass coverslips (VWR, 24×50mm) were cleaned by 10M NaOH and silanized by 3-aminopropyl triethoxysilane (APTS) following a procedure described in section 3.1 to create a positively-charged surface layer. Biotinylated PNMP was dissolved in 1,4-dioxane (3 wt%) and spincoated on APTS-modified coverslips to obtain ~130 nm thick films. Immunological synapse arrays were prepared on PNMP-coated coverslips using a photolithography-based technique we previously described in section 3.3 for patterning multiple mono-biotinylated proteins. The arrays are based on segregated patterns of immobilized biotinylated anti-CD3 and ICAM-1/Fc fusion proteins. PNMP thin films on cationic glass substrates prepared as described above were first exposed to UV irradiation through a photomask for 20 min, and developed by rinsing with pH 7.4 PBS to define the regions that would become activation sites. Next, the substrate was re-exposed to UV without a photomask, priming the background regions of the resist film for dissolution. The removable plastic sidewalls of a commercial eight-well chambered coverslip (Lab-Tek permanox slides, Nunc, well area: 0.8 cm<sup>2</sup>) were then attached to the partially-processed patterned coverslip using Superflex Clear RTV Silicone (Henkel Loctite Corp.) and cured

for 24 hr at 20°C, to create culture wells with the patterned glass substrate serving as a base. Before ‘erasing’ the background film region, SAV (10 µg/ml) and biotinylated anti-CD3 (or biotinylated isotype control antibody, 5 µg/ml) were sequentially incubated over the surface for 30 min each in PBS pH 6.0 at 4°C, binding to the available surface-tethered biotin groups (step (iv)). (As an estimate of the binding capacity of biotinylated PNMP films, the density of SAV coupled to PNMP surfaces measured using <sup>125</sup>I-labeled SAV was ~ 4,000 molecules/µm<sup>2</sup>; however, this value likely overestimates the density of active anti-CD3 and ICAM-1 sites on the surfaces.) Excess free biotin groups remaining on the tethered anti-CD3 were blocked by sequential incubation with SAV (10 µg/ml, 30 min) and biotin-PEO-amine (Pierce EZ-link, 10 µg/ml, 30 min, at 4°C). The exposed PNMP film masking the ‘background’ (and protein bound to it) was then dissolved by immersing the protein-conjugated surface in pH 7.4 PBS (step (v)). Though the bulk of the masking PNMP film dissolved, the cationic substrate electrostatically retained a thin layer of biotinylated PNMP on the surface. Using these freshly exposed biotin groups, the ‘adhesion field’ was functionalized by sequential assembly of SAV (10 µg/ml, 30 min), biotinylated anti-human Fc (10 µg/ml, 30 min), and ICAM-1/Fc (5 µg/ml, 30 min) at 4°C (step (vi)).

The density of TCR ligands (anti-CD3 antibody) was varied by mixing biotinylated anti-CD3 with biotinylated irrelevant antibodies (Rat IgG, BD Bioscience) in different

ratios during deposition. Surfaces with three different surface densities (100%, 20%, and 4%) of anti-CD3 were prepared. The relative density of anti-CD3 was measured by using Cy2-labeled anti-hamster antibody as described below. Anti-CD3 and Rat IgG patterned surfaces were incubated with 10  $\mu\text{g/ml}$  Cy2-conjugated anti-hamster antibody in PBS containing 0.02 wt% of Tween 20 at room temperature for 30 min, rinsed five times with PBS, and fluorescence intensities were recorded by fluorescence microscopy.

Background subtracted fluorescence intensities (arbitrary unit) plotted with the percentage of anti-CD3 showed a linear relationship (Figure 4. 2).

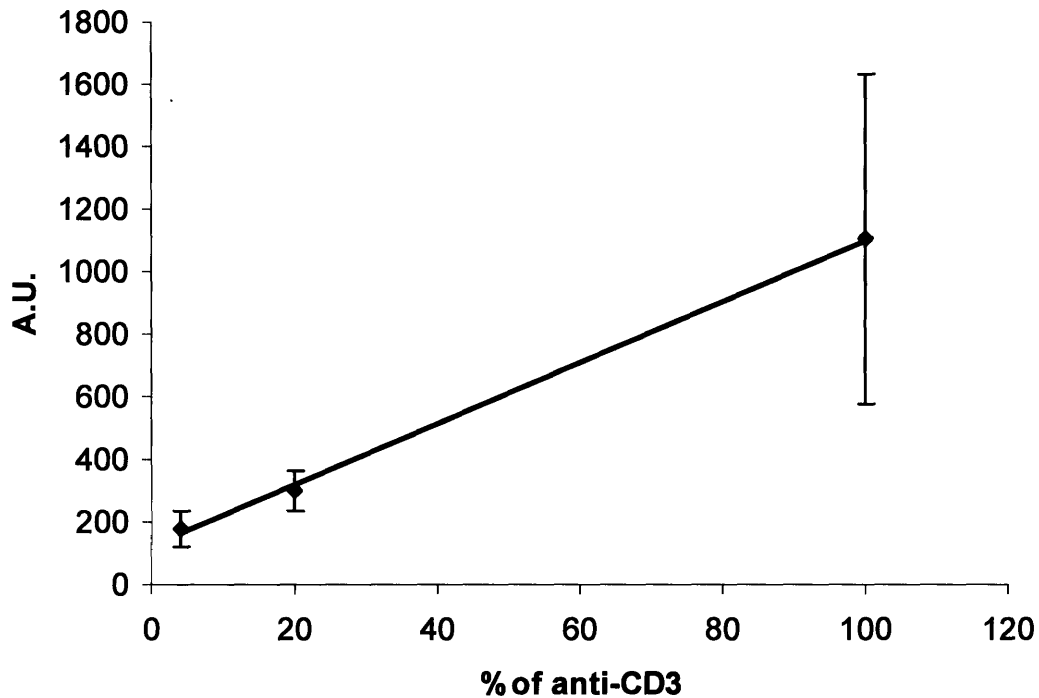


**Figure 4. 2** Various surface densities of anti-CD3 detected by Cy-2-coupled anti-hamster antibody. Error bars: stdev.

### **Enzyme-linked Immunosorbent assay (ELISA)**

The functional outcome of T cell interactions with patterned surfaces was assayed by measuring levels of IL-2 and IFN- $\gamma$  secreted into the culture supernatants by T cells. T cells ( $10^5$ ) were seeded on patterned substrates in 300 $\mu$ l of RPMI media and incubated at 37°C 5% CO<sub>2</sub> for 48 hrs; 100 $\mu$ l of supernatant was then collected from each sample for ELISA analysis of cytokine concentrations. For IL-2 ELISA, purified anti-IL-2 (JES6-1A12, BD Bioscience) and biotinylated anti-IL-2 (JES6-5H4, BD bioscience) were used for

a capturing and a detection antibody, respectively. An ELISA kit from R&D systems was used for IFN- $\gamma$  detection.

## 4.2 Control of T cell Adhesion and Migration

In order to find a proper adhesion ligand that induces physiological migration behavior of T cells, we tested two different adhesion ligands: ICAM-1, a native ligand of T cell integrin LFA-1, and anti-CD11a (M17/4; BD Bioscience), an antibody that binds to the  $\alpha$  chain of LFA-1.

ICAM-1 and anti-LFA-1 were immobilized by short molecular tether to the surfaces, as illustrated schematically in Figure 3. 12B and Figure 3. 13C, respectively. SAV- (Figure 3. 12A) and anti-human Fc- (Figure 3. 13B) presenting surfaces were used as negative controls. T cells were seeded onto surfaces presenting these ligands and imaged for one hour in 30 second intervals. T cells attached to the substrates were identified by video microscopy; cells that were not floating freely were scored as adherent. The percentage of cells adhering to the surfaces within 20 minutes was counted and plotted for each type of adhesion ligand (Figure 4. 3). Surfaces bearing ICAM-1 or anti-LFA-1 adhesion proteins showed significantly higher percentages of cells adhering on the surface (about 90%) relative to control surfaces (SAV, and anti-Human Fc presenting surfaces, 35% and 23%

respectively).

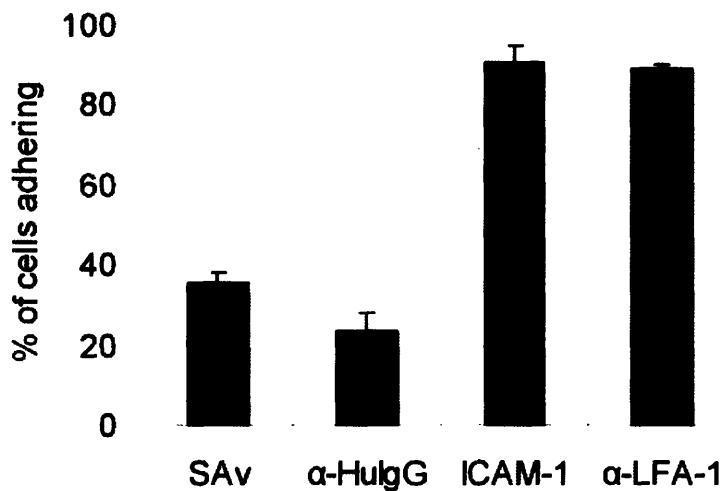


**Figure 4. 3 Percentage of T cells adhering on various surfaces in 20 minutes.  $\alpha$ -HuIgG denotes anti-Human IgG.**

Despite the similarity in the overall levels of adhesion promoted by both ICAM-1 and anti-LFA-1, the morphology and migratory behavior of T cells on these two different ligands was strikingly different. T cells seeded on ICAM-1 surfaces took on a characteristic ‘hand-mirror’ polarized morphology and migrated rapidly with an average velocity of  $\sim 10 \mu\text{m}/\text{min}$ , similar to previous reports where ICAM-1 was coated by adsorption on glass substrates<sup>20,105</sup> or T cells in LNs observed by two-photon microscopy<sup>57,58</sup> (instant velocities of two representative T cells are plotted in Figure 4. 4 as dashed lines and representative time lapse images are shown Figure 4. 5A). In contrast, T



cells on anti-LFA-1-presenting surfaces exhibited minimal translocation and maintained a largely unpolarized morphology (instant velocities of two representative T cells are plotted in Figure 4. 4 as solid lines and representative time lapse images are shown Figure 4.

5B).<sup>106</sup>

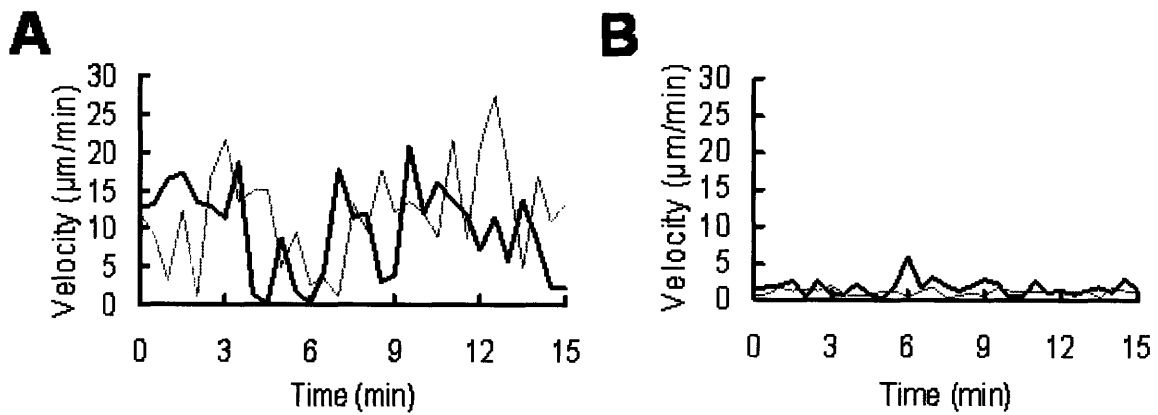


**Figure 4. 4 Instant velocity of two representative T cells on ICAM-1 surfaces (A) and anti-LFA-1 surfaces (B).**

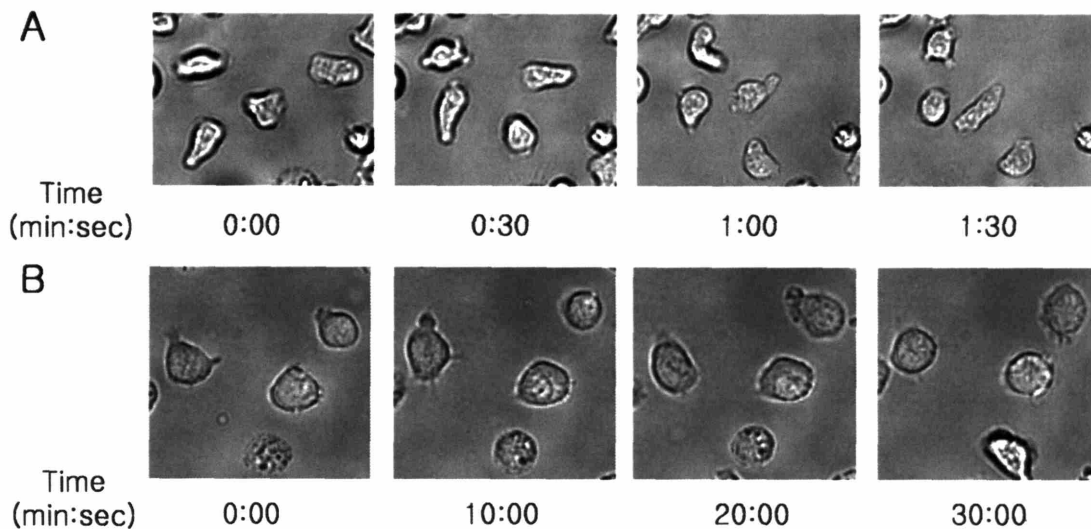


**Figure 4. 5 Time lapse images of T cells on ICAM-1 surfaces (A) and anti-LFA-1 surfaces (B).**

These results indicate that surfaces presenting tethered ICAM-1 combine high cell adhesion with high cell motility, as desired for promoting T cell ‘scanning’ of the artificial synapse arrays. The artificial ligand anti-LFA-1, on the other hand, tended to immobilize cells on the surface.

### **4.3 Fabrication of the immunological synapse arrays**

Having established an appropriate adhesion ligand to promote T cell migration on patterned surfaces, we next sought to present patterns of ‘activation sites’ on the substrates. We first sought to create arrays of ‘focal’ T cell activation sites, surrounded by a field of tethered adhesion molecules, as schematically illustrated in Figure 4. 1. An antibody

against the CD3 $\epsilon$  chain of the TCR complex<sup>107</sup> was tethered to surfaces within the activation sites, as a commonly employed surrogate for the T cell receptor's native ligand (peptide-MHC complexes),<sup>108,109</sup> while recombinant ICAM-1 was immobilized in the 'adhesion field'. We hypothesized that such surfaces would allow T cells engaging an activation site to ligate LFA-1 in a peripheral distribution around the central patch of TCR ligands, mimicking the microscale organization of the 'mature' immunological synapse.<sup>14,18</sup>

To create multicomponent protein patterns, PNMP thin films cast on cationic aminosilane glass substrates were UV exposed through a photomask to define the activation sites (Figure 4. 6 step (i)), followed by dissolution of the bulk of the film in the exposed regions by washing with phosphate-buffered saline (PBS, pH 7.4, step (ii)). In this step, a thin layer of the exposed polyelectrolyte resist remains bound to the cationic substrate to present biotin for further protein assembly. In step (iii), the film is exposed to UV without a mask, priming the background portions of the film (which will become the adhesion field) for dissolution. A first ligand is then immobilized over the entire surface (step (iv)) by incubation in a pH 6.0 solution; the exposed photoresist film masking the adhesion field regions does not dissolve at this slightly reduced pH. This is followed by a gentle 'erasure' of the remaining masking film by washing in PBS pH 7.4 (step (v)). As in step (ii), a thin molecular layer of biotinylated PNMP is retained on the substrate, providing

fresh biotin groups for a final step of backfilling with a second ligand (step (vi)). This procedure allowed segregated patterning of two ligands onto surfaces, keeping the immobilized proteins fully hydrated in near-neutral pH buffers during the surface processing. Biotinylated anti-CD3 in the activation sites was tethered via a streptavidin (SAv) bridge, while recombinant ICAM-1/Fc fusion proteins were immobilized via a biotinylated anti-Fc antibody and streptavidin (illustrated in the insets of Figure 4. 6A, steps (iv) and (vi)).

By blocking excess biotin groups of patterned anti-CD3 with Alexa-Fluor647-conjugated streptavidin and detecting immobilized ICAM-1 with a FITC-conjugated anti-ICAM-1 antibody, the final spatial distribution of the two ligands on the patterned PNMP surface was visualized. Representative fluorescence images depicting the spatial patterning of anti-CD3 (far red fluorescence) and the adhesion ligand ICAM-1 (green fluorescence) in a square array of circular activation sites 6  $\mu\text{m}$  in diameter are shown in Fig. 2B. As shown by the single-color and overlay images, the pattern fidelity and segregation of ligands to their respective domains by this approach was excellent. Though ICAM-1/Fc molecules were immobilized here via noncovalent antibody binding to the Fc portion of the fusion protein, the half life for release of immobilized ICAM-1/Fc from the surface was  $\sim 55$  hrs (Figure 3. 14), indicating that the ligand density changed only very

slowly over the time-courses studied in the experiments described below.

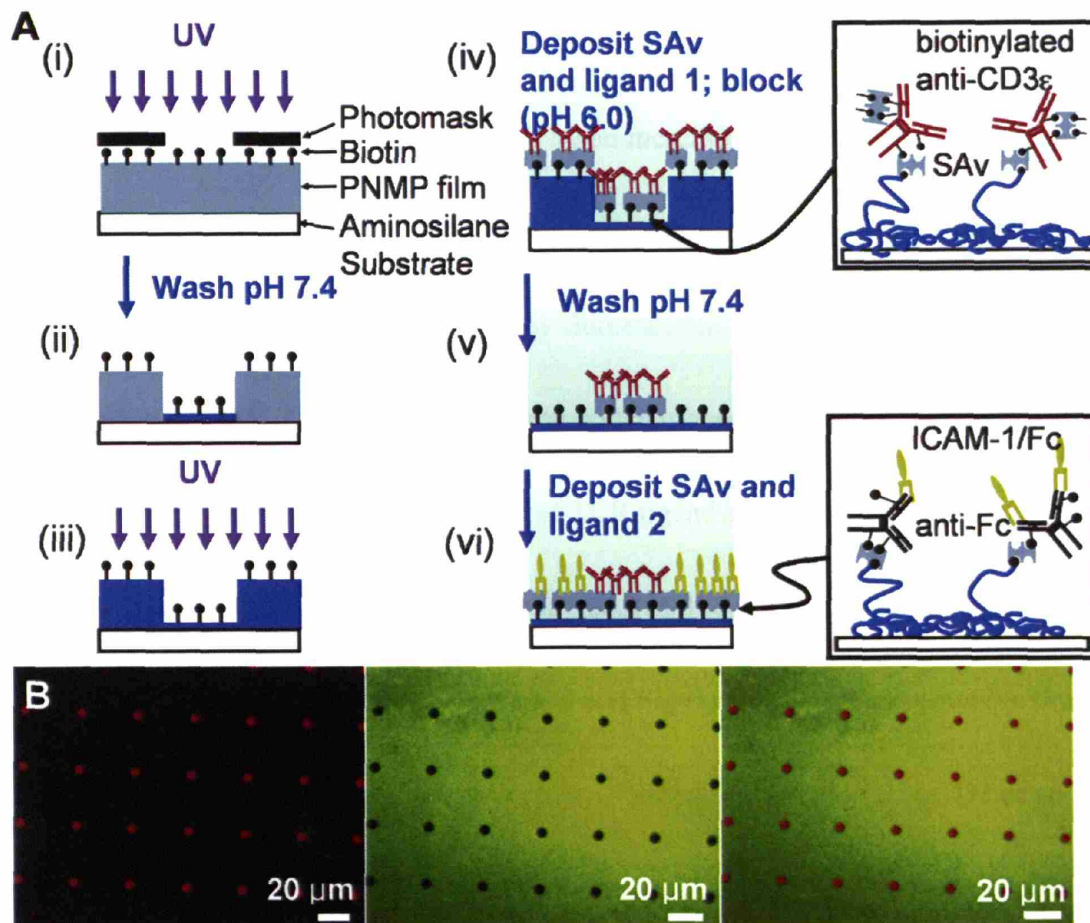


**Figure 4. 6** Fabrication of immunological synapse arrays. (A) Schematic procedure of surface patterning: Insets in steps (iv) and (vi) illustrate the structure of protein ligand linkages to the surface. (B) Fluorescence micrographs taken from one field of a two-component patterned surface: SAV-Texas red detecting biotinylated  $\alpha$ -CD3 (left panel),  $\alpha$ -ICAM-1-FITC detecting ICAM-1 (middle panel), and their overlay (right panel).

## 4.4 Early TCR signaling triggered by immunological synapse arrays

Motile T cells that encounter antigen-loaded APCs receive a ‘stop signal’ provided by TCR triggering,<sup>20</sup> which is closely followed by an increase in intracellular calcium levels driven by TCR signaling.<sup>21,22,110</sup> We confirmed that synthetic synapse arrays elicited a similar sequence of early T cell responses by fluorescence videomicroscopy analysis of murine primary CD4<sup>+</sup> T cell blasts interacting with surfaces patterned as shown in Figure 4. 6B. Importantly, the discrete presentation of TCR ligand in defined areas allowed T cells landing on the ‘adhesion field’ to adopt a polarized, motile pre-antigen-contact state prior to TCR triggering on activation sites (Figure 4. 4 and Figure 4. 5A). Representative time-lapse images of single T cell responses to synapse surfaces presenting anti-CD3 or an isotype control IgG from the activation sites are shown in Figure 4. 7A and B, respectively. T cells migrating on control surfaces passed through activation sites presenting isotype control antibodies without stopping or altering intracellular calcium levels (Figure 4. 7A). In contrast, migrating T cells that encountered an activation site presenting anti-CD3 stopped migration, changed from a polarized to rounded morphology, and elevated intracellular calcium (Figure 4. 7). Quantitation of the response of T cells to contact with activation sites by calculation of the cells’ instantaneous velocity and average fura ratio vs.

time showed the temporal proximity of the halt in migration and calcium elevation that occur coincident with activation site contact (illustrated in Figure 4. 8 for two representative single cells). Though the diameter of the anti-CD3 activation sites examined here (and in the majority of the studies described below) was significantly larger than the typical dimensions of cSMACs formed by T cells,<sup>14,18</sup> anti-CD3 activation sites with smaller diameters (4 $\mu$ m, 3 $\mu$ m, or 2  $\mu$ m) triggered qualitatively similar migration/halt and calcium responses (data not shown). Thus, the presentation of segregated patterned protein signals from these substrates elicited dynamic T cell migration and calcium signaling behavior mirroring responses observed with live T cell-APC interactions<sup>21</sup>.

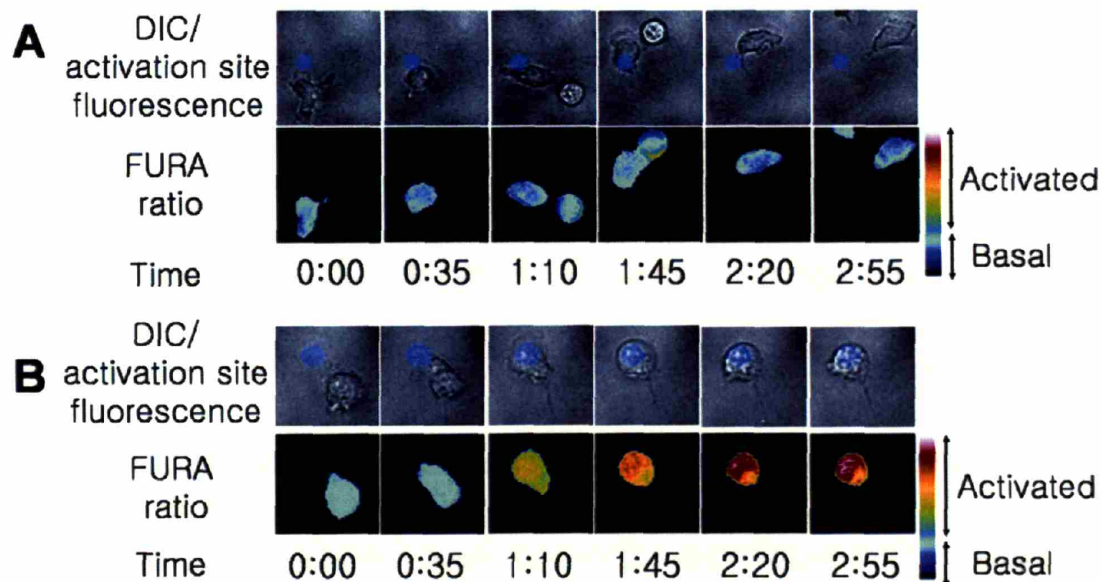


**Figure 4. 7** Cell morphology and calcium signaling (tracked by fura fluorescence ratio) as single OT-II CD4<sup>+</sup> T cells contact a control (A) or anti-CD3-presenting (B) activation site of a synapse array.

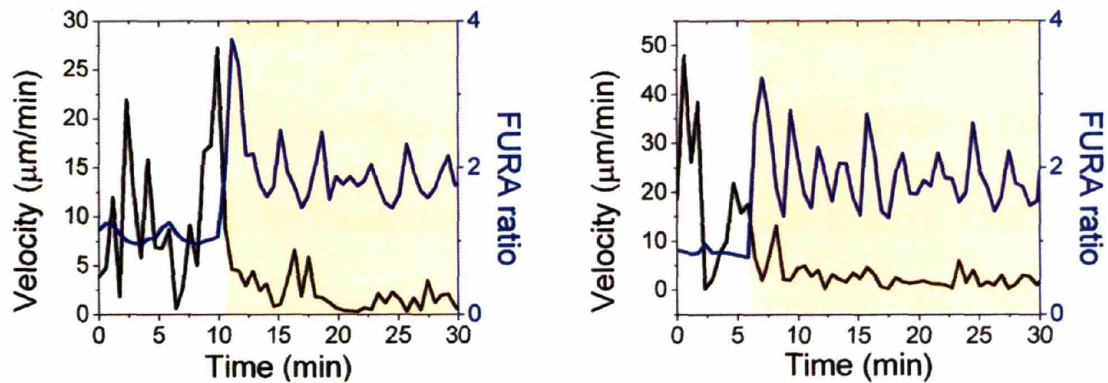


**Figure 4. 8 Representative instantaneous velocities and average fura ratios of two different single T cells encountering activation sites on immunological synapse surfaces. Left-hand edges of the orange-shaded regions denote the time-point of initial contact with the activation site. Traces show the near-simultaneous drop in T cell velocity and elevation of intracellular calcium levels coincident with contact of activation sites.**

Interestingly, the duration of interactions between T cell and activation sites was sensitive to the surface density of anti-CD3 on the activation sites (Figure 4. 9). When activation sites were occupied by maximal densities of anti-CD3 (order of  $\sim 1000$  molecules  $/\mu\text{m}^2$ ), more than 90% of T cells exhibited stable interactions (remaining on the activation sites more than 10 min with stable calcium mobilization) while only a fraction of T cells showed transient interactions (remaining on the activation sites for only a few min with transient calcium influx) or ignored the activation sites (did not stop migration or change in calcium levels). As the surface density of anti-CD3 decreased, more T cells made transient interactions with the activation sites, or ignored them. When the activation sites



were occupied by 100% of irrelevant antibodies (Rat IgG), all T cells ignored the activation sites and crawled over the surfaces with velocities and morphologies similar to T cells migrating on the ICAM-1 coated surfaces lacking activation sites (Figure 4. 4 and Figure 4. 5B). Time-averaged FURA ratios (over 10 min) of T cells stably interacting with the activation sites with various anti-CD3 densities are plotted in Figure 4. 10. For comparison, the mean time-averaged resting FURA ratio of T cells crawling on synapse surfaces comprised of activation sites with no anti-CD3 is included in the same figure. Surprisingly, calcium signaling in T cells that did stably interact with activation sites was strong at all 3 ligand densities.

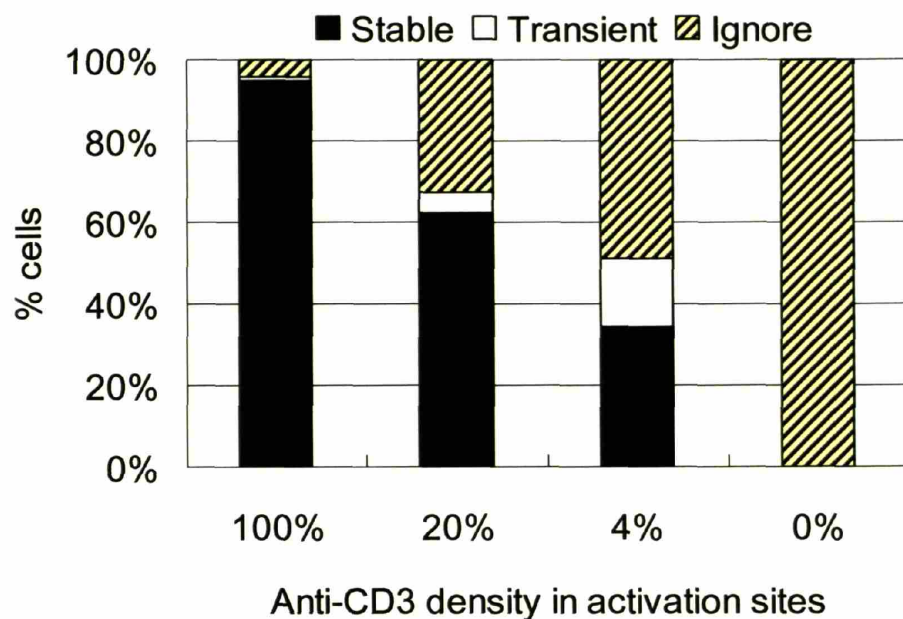


**Figure 4. 9** 5C.C7 T cells interacting with titrated surface densities of anti-CD3 immobilized in 6  $\mu\text{m}$ -diameter activation sites. Interactions are classified into three categories based on the duration of T cells remaining activation sites and stability of calcium mobilization; stable means longer than 10 min of interaction with stable calcium mobilization, transient means a few min of interaction with transient calcium influx, and ignore means no interaction or change in calcium levels.

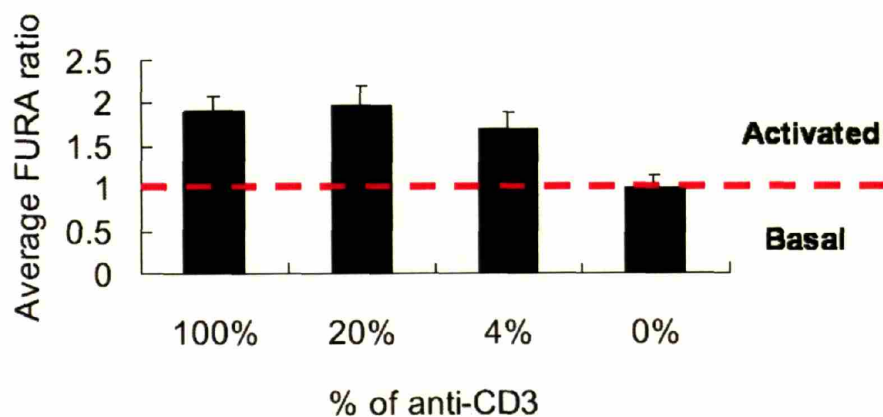


**Figure 4. 10** Time-averaged FURA ratio (20 min - 40 min) as a measure of calcium signaling in 5C.C7 T cells that stably interacted with 6  $\mu\text{m}$ -diameter activation sites bearing titrated surface densities of anti-CD3.

In addition to controlling T cell activation state, the segregated presentation of ‘stop’ (TCR ligand) and ‘go’ (ICAM-1) signals from patterned surfaces led to self-assembly of T cells on the array sites. T cells migrated randomly on synapse surfaces until activation sites were encountered; once triggered by an activation site, responding cells generally centered themselves over the activation site and maintained a long-lasting (~7-17 hrs) contact. Within 30 min at optimal T cell seeding densities (~1.5 cells seeded on the surface per activation site), the majority of the activation sites were occupied by single T cells (Figure 4. 11). Such cellular self-organization dictated by surface patterns could be used to prevent or promote cell-cell contacts as well as cell-substrate contacts.

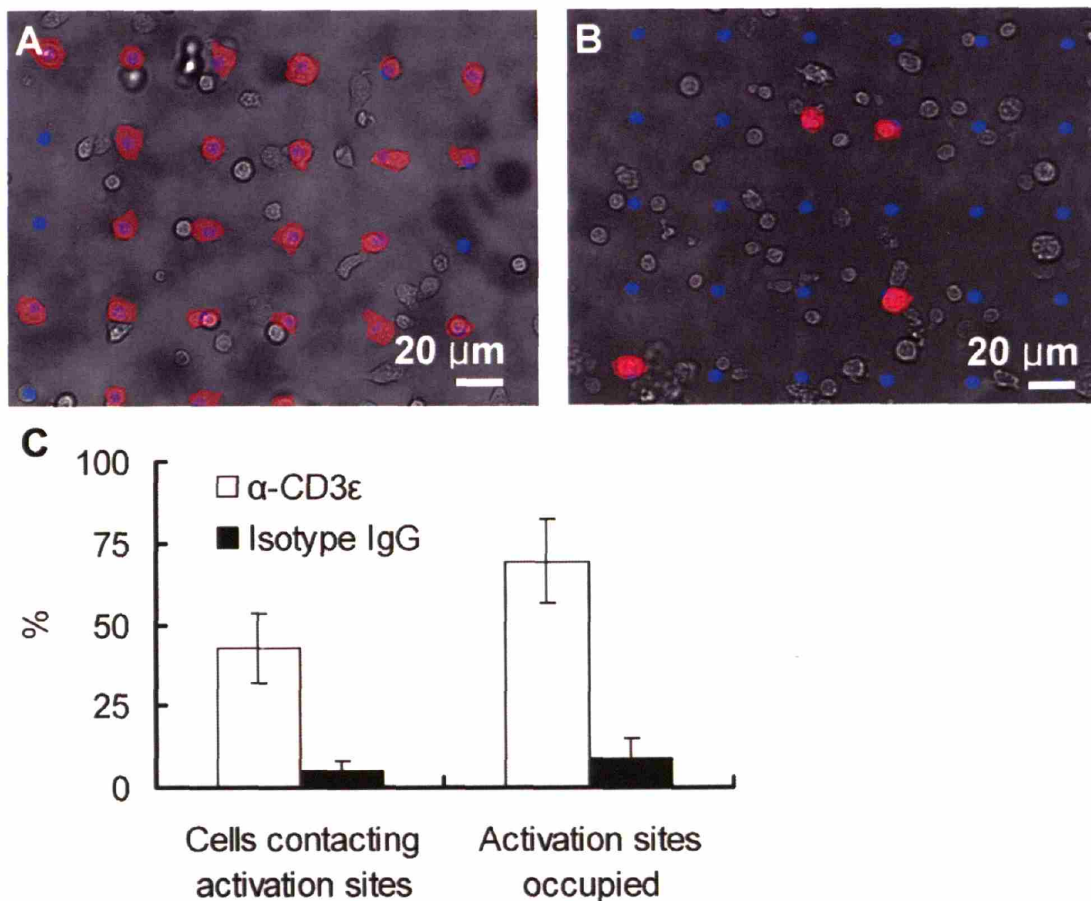


**Figure 4.11** T cell localization to activation sites 30 min after seeding on immunological synapse surfaces presenting arrayed spots of anti-CD3 vs. control surfaces bearing arrayed spots of a control IgG. Representative overlay micrographs of brightfield and activation site fluorescence images for patterned anti-CD3 surfaces (A) and control surfaces (B) are shown, with T cells localized to activation sites highlighted by a red false color overlay. (C) Percentages of cells contacting activation sites and percentages of sites occupied for anti-CD3 or control IgG activation sites are shown (ave  $\pm$  stdev).

## 4.5 Dynamics of T cells interacting with immunological synapse arrays at late times and end point functional responses

Using videomicroscopy, T cell division triggered by activation sites was directly

observed, as illustrated by the time-lapse image sequence of a T cell dividing on one of the array activation sites ~20 hrs post-seeding (Fig. 4A and Supporting video 3). Unlike uniformly-coated anti-CD3 substrates commonly used to elicit polyclonal T cell activation, here T cells can migrate away from the activation sites, as they can when interacting with discrete live APCs in vitro or in vivo. Interestingly, we observed that daughter cells formed after cell division were ignorant of activation sites, and rapidly migrated through TCR ligand-presenting regions with only transient pauses (~10 minutes) or without stopping at all for up to 3 hrs after cell division. This ignorance of activation sites by divided T cells may reflect a mechanism to allow activated T cells to exit from the T zone of lymph nodes to travel lymph node follicles, or peripheral tissues to carry out their effector functions without further arrest by contact with antigen-bearing APCs.

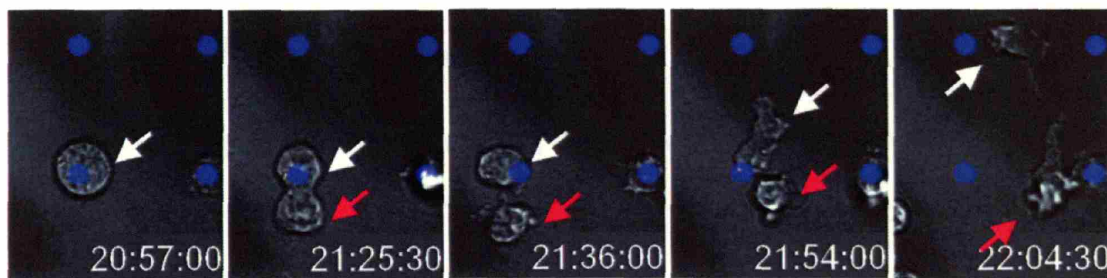


**Figure 4. 12** Time-lapse image sequence depicting a 5C.C7 CD4+ T cell undergoing cell division on a synapse array surface. Arrows track the original cell and resulting two daughter cells.

At the population level, we measured the secretion of the T cell growth factor

interleukin-2 (IL-2) and the effector cytokine interferon- $\gamma$  (IFN- $\gamma$ ) by T cells interacting with synapse arrays presenting patterned anti-CD3/ICAM-1 or control ligands (anti-CD3/SAv or isotype IgG/ICAM-1) in the activation site/adhesion field regions (Figure 4. 13). Higher levels of IL-2 and IFN- $\gamma$  production were seen on the anti-CD3/ICAM-1 surfaces than anti-CD3/SAv, possibly due to rapid T cell motility and subsequent encounter of T cells with activation sites and/or costimulation delivered from LFA-1 engagement of ICAM-1.<sup>111,112</sup> Negligible amounts of cytokine were produced by T cells cultured on isotype control IgG/ICAM-1 patterned surfaces. Cytokine production was also triggered by 3  $\mu$ m-diameter activation sites, and titration of the density of tethered anti-CD3 within 6  $\mu$ m-diameter activation sites revealed a dose-dependent response of IL-2 production with anti-CD3 density (Figure 4. 14).

Altogether, these results demonstrate that patterned synapse arrays can elicit full T cell functional responses, and allow single-cell dynamics of T cells over extraordinary time intervals and at times as late as the onset of cell division to be tracked.

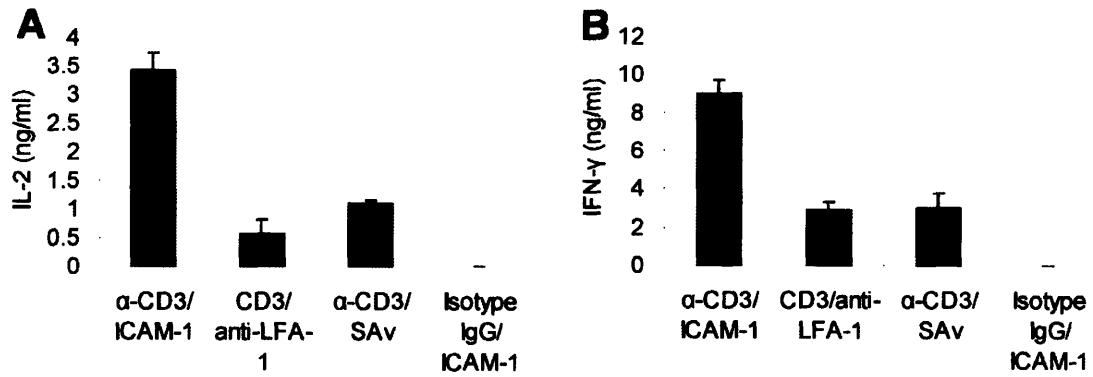


Figure 4.13 IL-2 (A) and IFN (B) production by OT-II CD4<sup>+</sup> T cell blasts incubated on surfaces for 48 hrs (Shown are ave  $\pm$  s.e.m. for one representative experiment of 3).

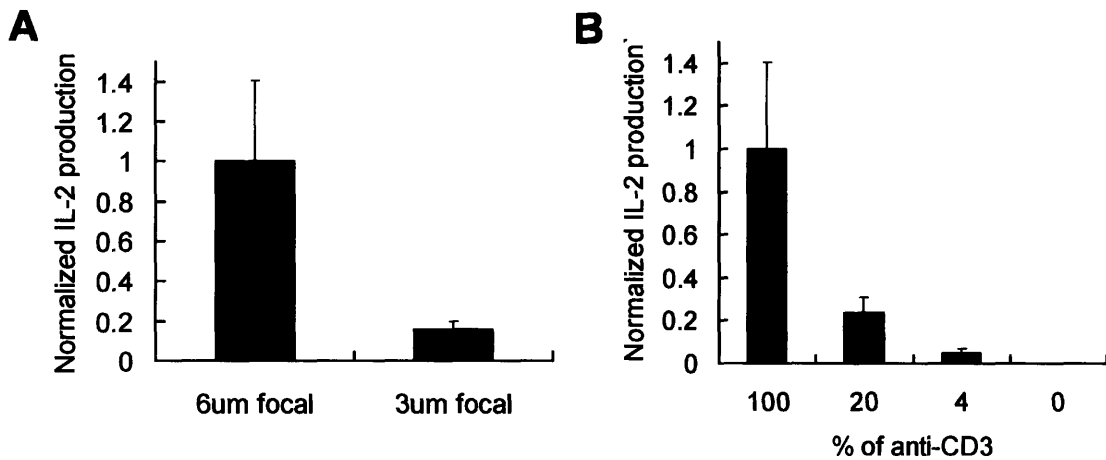


Figure 4.14 Normalized IL-2 secretion by T cells cultured on ‘focal’ synapse arrays as a function of (A) activation site diameter or (B) anti-CD3 density within activation sites. (A) 3  $\mu$ m-diameter activation sites, with one quarter the surface area of 6  $\mu$ m-diameter sites (and therefore, one quarter as much total anti-CD3 displayed to each T cell), triggered IL-2 production in T cells at correspondingly lower levels relative to 6  $\mu$ m-diameter anti-CD3 sites. (B) Ligand density was varied by mixing biotinylated anti-CD3 with biotinylated irrelevant antibody (Rat IgG) at different ratios (indicated by the percentages) during coupling to the activation sites; IL-2 production by T cells exhibited a dose-dependent response to the density of anti-CD3 presented.

## **5 Control of T cell activation by modulating immunological synapse formation in T cells**

In this chapter, T cell responses to immunological synapse arrays are further described in terms of molecular assembly occurring within T cells encountering different surface patterns. Further, we compare synapse formation, cellular dynamics, and cytokine secretion by T cells interacting with surfaces where a fixed quantity of ligand is displayed in two different physical patterns. The effects of adhesion ligands and TCR ligand geometry were investigated by early time point (10 to 30 min after seeding) immunostaining and late time point (48 h) secreted cytokine measurements. In particular, T cell responses on ‘focal’ and ‘annular’ geometry TCR ligand patterns surrounded by an ICAM-1 adhesion field, representative of ‘mature’ and ‘immature’ synapses, respectively,<sup>14,26</sup> were compared to test the importance of focal TCR ligand presentation in T cell triggering.



## 5.1 Materials and Methods

### Immunostaining

T cells were seeded on immunological synapse surfaces and incubated at 37°C, 5% CO<sub>2</sub> (for a phosphotyrosine staining, 10 min of incubation, and for all the other stainings, 20 min of incubation). Cells were then fixed, permeabilized, and stained as described elsewhere.<sup>113</sup> Briefly, cells were fixed in 3% paraformaldehyde in PBS for 15 min at 20°C, washed five times in PBS, permeabilized by 0.3% Triton X-100 in PBS for 10 min, rinsed five times in PBS, and subsequently blocked in serum containing RPMI medium for 5 min. Calcium/magnesium free Dulbecco's phosphate buffered saline (DPBS, VWR) containing 2% FCS was used for antibody staining of permeabilized T cells. For TCR, LFA-1, tubulin and phosphotyrosine (pY) staining, FITC- or CyChrome-conjugated anti-TCR $\beta$  (H57; BD Bioscience), PE-conjugated anti-CD11a (2D7; BD Bioscience), Cy3-conjugated anti- $\beta$ -tubulin (TUB2.1; Sigma), and FITC-conjugated anti-pY (4G10; Upstate Biotechnology) were used, respectively. For talin and PKC- $\theta$  staining, polyclonal rabbit anti-PKC- $\theta$  and goat anti-talin (Santa Cruz Biotechnology) were used as primary antibodies and Cy2-conjugated donkey anti-rabbit IgG and Texas-Red conjugated donkey anti-goat IgG (Jackson ImmunoResearch) were used as secondary antibodies. Fluorescence images of fixed cells on patterned surfaces were acquired by widefield epifluorescence optical

sectioning (25 individual planes, 0.5 $\mu$ m apart) using either a 100X NA 1.3 objective or a 63x NA 1.4 objective, to characterize protein clustering at the cell-substrate contact plane.

### **Intracellular cytokine staining**

Naïve 5C.C7 T cells were primed with peptide-pulsed splenocytes for 5 d, then restimulated for 6 h on anti-CD3-coated TC plates (5  $\mu$ g/ml, for 6 h at 37°C) in the presence of 1  $\mu$ g/ml anti-CD28 and Brefeldin A (Sigma, last 2 hrs) to prevent cytokine secretion. The cells were fixed, permeabilized, stained for the presence of intracellular cytokines (IL-2, IL-4, and IFN- $\gamma$ ), and analyzed by flow cytometry (BD FACScan) to assess their profile of cytokine production. For negative controls, T cells were incubated with excess amounts of anti-cytokine antibodies without fluorophores prior to staining to block intracellular cytokines. Antibodies used for staining are as follows: pure or PE-conjugated anti-IL-2 (JES6-5H4; BD Bioscience), pure or FITC-conjugated anti-IFN- $\gamma$  (XMG1.2; BD Bioscience), and pure or PE-conjugated anti-IL-4 (11B11; BD Bioscience).

## **5.2 Subcellular components distribution in T cells on the adhesion field**

Migrating T cells in lymphoid organs and peripheral tissues have a characteristic hand-

mirror or frying pan morphology; a leading edge bulb is mostly composed of the nucleus while a handle-shaped tail, a uropod, contains the majority of cytoplasm and the microtubule organizing center (MTOC).<sup>54,114</sup> Paradoxically, most of the T cell's TCRs distribute in the uropod even though the leading edge is much more sensitive to TCR ligands.<sup>19,115</sup> We confirmed these classical features of highly motile and polarized T cells by performing tubulin and TCR immunostaining of T cells migrating on ICAM-1-presenting surfaces. As shown in Figure 5. 1 and Figure 5. 2, T cells on ICAM-1 surfaces have characteristic hand mirror shapes (left panels of the Figure 5. 1 and Figure 5. 2) with the majority of TCRs (middle panel of Figure 5. 2) and MTOC (right panel of Figure 5. 1) located in the uropods. Interestingly, most of the phosphorylated tyrosine in migrating cells was observed in the uropods (right panel of Figure 5. 2), possibly due to clustering of phosphorylated motor proteins such as class II myosins that play a critical role in T cell motility and arrest.<sup>116</sup>

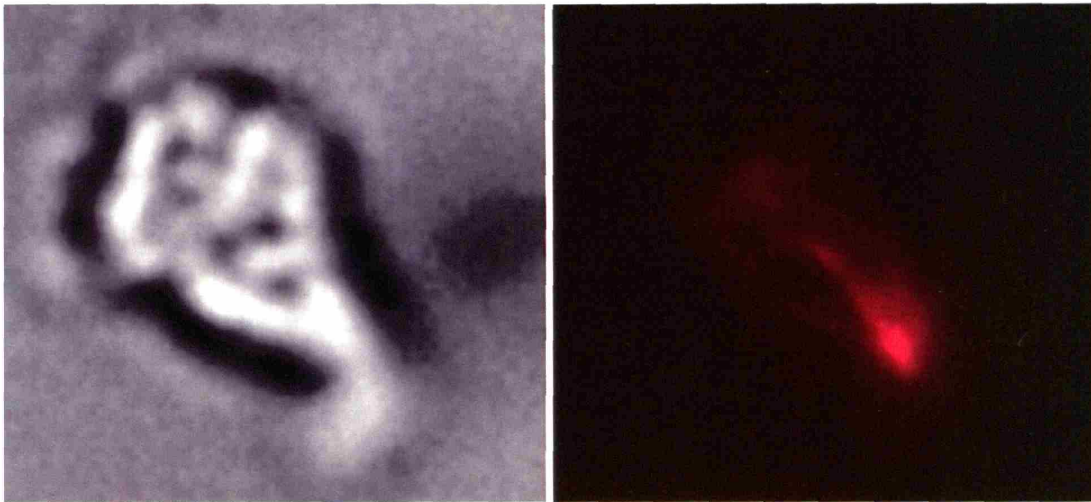


**Figure 5. 1** Representative tubulin staining of a T cell migrating on an ICAM-1 surface. DIC (left) and tubulin (right).

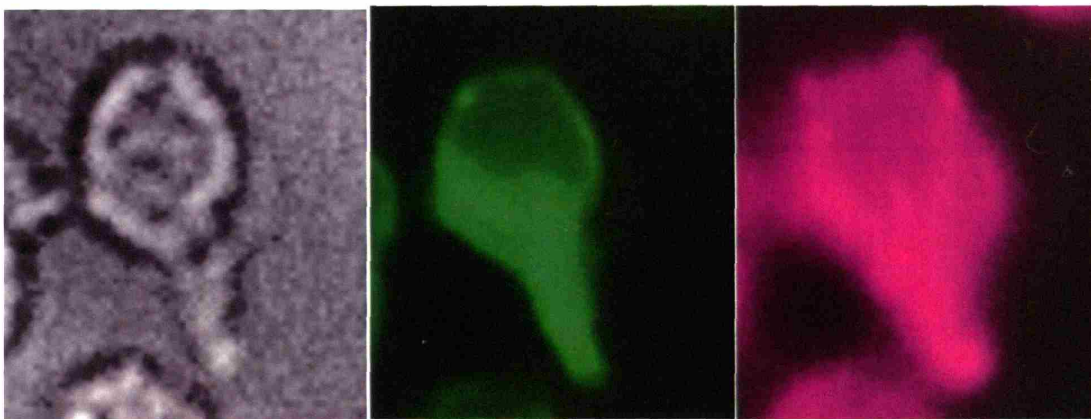


**Figure 5. 2** Representative TCR and phosphotyrosine (pY) immunostaining of a T cell migrating on an ICAM-1 surface. DIC (left), TCR immunostaining (middle) and pY immunostaining (right).

### **5.3 Modulating the Immunological Synapse Formation in T cells**

In live APC-T cell interactions, TCR triggering is followed by the clustering of receptor-ligand pairs in the T cell-APC interface, forming an immunological synapse.

Depending on the activation conditions, micron-scale physical patterning of a number of cell surface and intracellular signaling molecules accompanies this process. To determine if a similar IS structure would assemble in response to the presentation of tethered patterned ligands, we performed immunostaining on CD4<sup>+</sup> T cell blasts fixed after 20 min of interaction with patterns of ‘focal’ anti-CD3 spots surrounded by ICAM-1 or anti-LFA-1 (Figure 5. 3). In synapses formed between T cells and live B cells, the cytoskeletal protein talin enriches in a peripheral ring surrounding a central accumulation of the critical signaling molecule protein kinase C- $\theta$  (PKC- $\theta$ ).<sup>18</sup> In a similar manner, we observed focal clustering of PKC- $\theta$  centered over sites of patterned anti-CD3, surrounded by a ring-like accumulation of talin (Figure 5. 3A and B). On the cell surface, LFA-1 and TCR have been shown to cluster in a pattern similar to the concentric arrangement of talin and PKC- $\theta$  inside the cell;<sup>18</sup> we also observed this concentric arrangement of TCR and LFA-1 for T cells interacting with activation sites of synapse arrays (Figure 5. 3C and D). Similar structures were observed for activation sites displaying 25-fold lower densities of anti-CD3 (data not shown), and with smaller-diameter activation sites (as shown in Figure 5. 4 for 2 $\mu$ m focal sites).

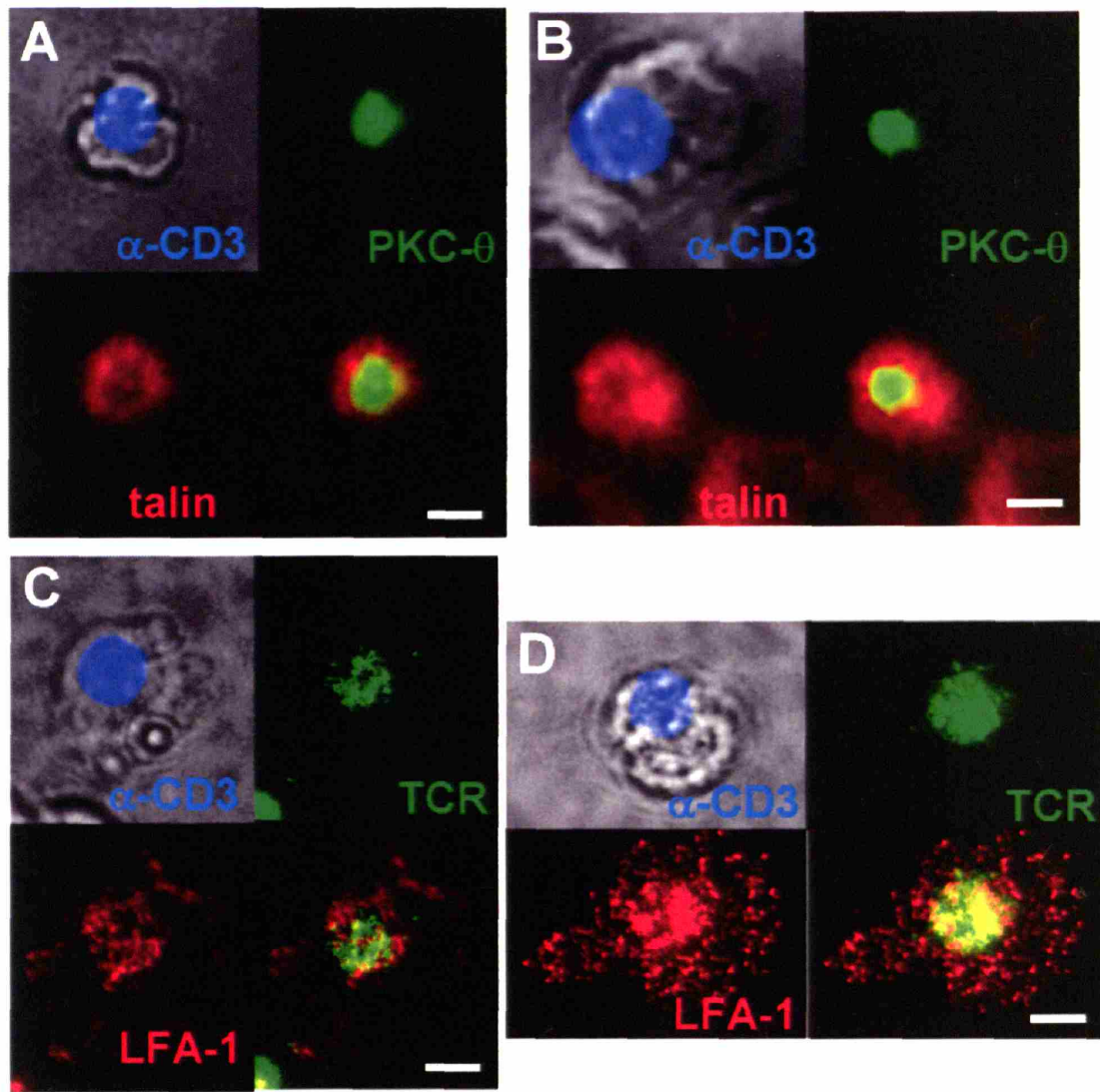
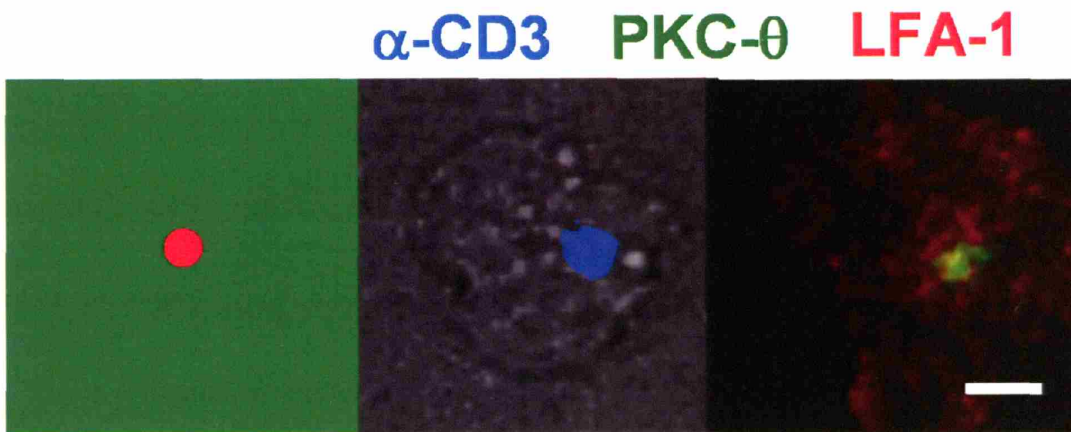


Figure 5.3 The immunological synapse formed in T cells interacting with 6 $\mu$ m focal activation sites. DIC/far red overlay (left top), green fluorescence (right top), red fluorescence (left bottom), and green/red overlay (right bottom). A. PKC- $\theta$  (green) /talin (red) staining of T cells on anti-CD3/ICAM-1 surface. B. PKC-  $\theta$  (green)/talin (red) staining of T cells on anti-CD3e/anti-LFA-1 surface. C. TCR (green)/LFA-1 (red) staining of a T cell on anti-CD3/ICAM-1 surface. D. TCR (green)/LFA-1 (red) staining of a T cell on anti-CD3/LFA-1 surface.



**Figure 5. 4 Representative micrographs of the immunological synapse formed by a T cell interacting with a 2 $\mu$ m activation site. A scale bar, 5  $\mu$ m.**

Clearly, a significant difference between T cell-live APC interactions and T cell-synapse array interactions rests with the mobility of the ligands presented; ICAM-1 and peptide-MHC complexes diffuse laterally in the membrane of the live APC but here we have immobilized these ligands on the surface by short molecular tethers. However, a powerful feature of this approach is the potential to use the fixed distribution of ligands to template an arbitrary organization of T cell surface receptors and thus probe the importance of specific physical patterns of receptor clustering on T cell functions, independent of changes in the total amount or quality of ligands presented to the T cell. We thus examined T cell responses to two additional types of immunological synapse arrays: ‘multifocal’ patterns of anti-CD3 patterned as four 2  $\mu$ m circles placed at the corners of a

square 6  $\mu\text{m}$  on a side, and ‘annular’ patterns of anti-CD3 with an outer diameter of 8  $\mu\text{m}$  and inner diameter of 4  $\mu\text{m}$  (Figure 5. 5). These activation site geometries were chosen to template T cell surface receptor clustering in patterns mimicking intermediate synapse structures observed prior to the formation of a mature IS.<sup>14,26,117</sup> In each case, the adhesion field was composed of immobilized ICAM-1. Immunostaining of T cells 20 min after seeding onto these altered synapse arrays revealed that the accumulation of both cell surface receptors and intracellular signaling molecules was impacted by the surface ligand pattern. As shown in Figure 5. 5A, PKC- $\theta$  clustered over each 2  $\mu\text{m}$  patch of TCR ligand on ‘quad’ patterns, with LFA-1 accumulating around each of these patches. Such multifocal PKC- $\theta$  clustering was observed in 53% of cells ( $n = 30$ ) on ‘quad’ patterned surfaces. On activation sites with an ‘annular’ geometry, PKC- $\theta$  clustered in coincidence with the annular activation patch in 25% of cells in full contact with the surface pattern (discussed further in 5.4). Strikingly, LFA-1 accumulated outside the anti-CD3 ring but was virtually excluded from the region of the interface inside the ring of surface anti-CD3, despite the presence of ICAM-1 in this region (Figure 5. 5).



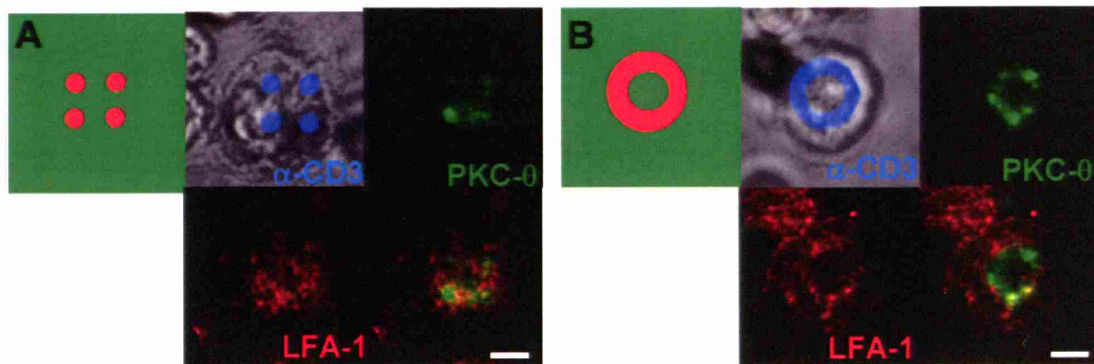


Figure 5.5 Synapse array patterns template T cell surface receptor and intracellular signaling molecule accumulation at the cell-surface contact site. Shown in each panel are schematics of the anti-CD3/ICAM-1 substrate pattern and representative immunofluorescence images at the cell-substrate contact plane of OT-II CD4<sup>+</sup> T cells fixed 20 min after seeding on synapse surfaces. (A) and (B) Immunostaining of (A) PKC- $\theta$  (green) and talin (red) or (B) TCR and LFA-1 on ‘focal’ anti-CD3 patterns. (C) and (D) Immunostaining of PKC- $\theta$  (green) and LFA-1 (red) on (C) ‘multifocal’ patterns (each anti-CD3 spot 2  $\mu$ m in diameter) or (D) ‘annular’ anti-CD3 patterns. Scale bars 5  $\mu$ m.

## 5.4 The Effect of Ligand Distribution on T Cell Activation

Having observed that surface ligand patterns could modulate T cell synapse assembly, we further investigated the behavior of T cells on ‘focal’ and ‘annular’ anti-CD3 patterned surfaces. First, we recorded the dynamics of T cell-surface interactions by videomicroscopy 30 min after seeding cells on ‘focal’ and ‘annular’ arrays. All T cells interacting with focal patterns of anti-CD3 centered themselves for full contact with the anti-CD3 circle, exhibited a rounded morphology, and made minimal membrane extensions away from the contact site. In contrast, the majority of T cells interacting with annular patterns made only partial contact with the anti-CD3 ring, exhibited a partially-polarized

morphology, and made dynamic membrane extensions away from the activation site: many cells continuously changed directions while maintaining a partial contact with the anti-CD3 ring. This unusual motion of T cells could be correlated with their polarization by performing tubulin immunostaining on fixed T cells. Figure 5. 6A and B show representative micrographs of T cells interacting with focal and ring anti-CD3 patterned surfaces, respectively. For both patterns, co-localization of the microtubule organizing center (MTOC) and PKC- $\theta$  over the anti-CD3 pattern was observed in ~90% of cells that exhibited significant clustering of PKC- $\theta$  (~80% of cells) at the cell-substrate interface (Figure 5. 6A and B). While T cells contacting focal patterns of anti-CD3 always covered the entire area of the activation site, the majority of T cells (64%) on ring patterns made only partial contact with activation sites. The morphology of PKC- $\theta$  accumulated by T cells contacting different patterns of anti-CD3 is summarized in Figure 5. 6. Most T cells that had partial contact with anti-CD3 rings showed focal clustering of PKC- $\theta$  co-localized with the MTOC at their points of contact with the activation site, as shown in the left panel of Fig. 6B. For a fraction of cells (25%) fully contacting anti-CD3 rings, PKC- $\theta$  assembled in an annular structure, as shown by the middle panel of Figure 5. 6B. Altogether, annular patterns of anti-CD3 appear to perturb the stable polarization of T cells. Helper T cells polarize PKC- $\theta$  and their MTOC toward APCs presenting agonist ligand,<sup>118</sup> and they can

also rapidly change the direction of polarization when a nearby stronger stimulus is detected.<sup>119</sup> It is possible that semi-motile T cells making only partial contact with annular activation sites may be in the process of continuously repolarizing their TCRs and signaling machinery around the annulus of ligand, seeking a focus of maximal stimulus.

Alternatively, the inability of T cells spread over the annular activation sites to focally cluster ligated TCRs may have frustrated the normal program of T cell activation.

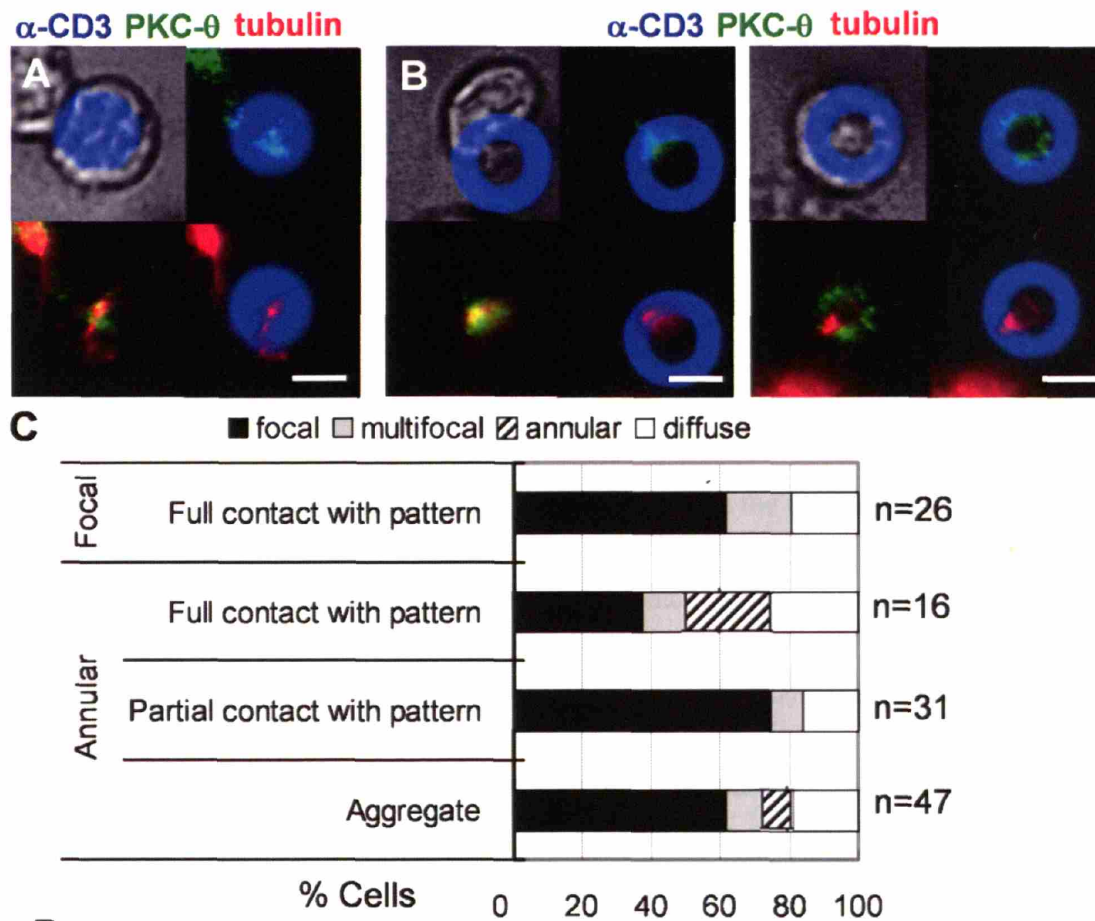


**Figure 5.6** T cell responses to 'focal' vs. 'annular' anti-CD3 activation sites. (A) and (B) Representative micrographs of 5C.C7 CD4<sup>+</sup> T cells interacting with focal and annular activation sites, respectively: overlay panels show DIC/activation site fluorescence (left top), PKC-θ/activation site fluorescence (right top), PKC-θ/tubulin (left bottom), and tubulin/activation site fluorescence (right bottom). Scale bars 5 μm. (C) Quantification of PKC-θ clustering morphologies.

To determine whether the altered early response of T cells to annular ligand patterns affected the functional outcome of T cell activation, several measures of the T cell response to 'annular' activation site patterns were compared to those obtained on 6 μm focal patterns.

IL-2 production (Figure 5. 7) and calcium signaling (Figure 5. 8) were not significantly affected by changing the physical display of anti-CD3 from focal sites to ring structures. Likewise, colocalization of phosphotyrosine with TCR, as a measure of TCR-associated signaling,<sup>36</sup> was similar for T cells responding to focal or annular activation sites (Figure 5. 9). In contrast, IFN- $\gamma$  secretion by T cells cultured on annular anti-CD3 patterns was greatly reduced compared to focal anti-CD3 patterns ( $p < 0.02$ , Figure 5. 9). Notably, the surface area of focal and annular activation sites (and thus the total amount of anti-CD3 encountered by the T cells) was comparable (ring patterns tested here had a 1.3-fold larger activation site area); thus, the reduction in IFN- $\gamma$  production cannot be ascribed to a lower density of available ligand on the annular pattern. The exact mechanism of this effect on cytokine production remains to be determined, but these results demonstrate that at least for the 5C.C7 transgenic CD4<sup>+</sup> T cells tested here, encounter with a non-focal display of TCR ligand may alter the program of T cell activation. Alternatively, 'annular' activation sites may have selectively activated a subpopulation of the primed T cell population; for example, Th1 and Th2 cells form different synapse structures and have different requirements for activation.<sup>120</sup> Though this alternative cannot be formally excluded, we found that on restimulation with anti-CD3-coated plates, a significant fraction of primed 5C.C7 T cells (as used for all of our studies) produced the Th1-associated cytokine IFN- $\gamma$

but only ~ 1% produced the Th2-associated cytokine IL-4 (data not shown), in agreement with earlier studies on 5C.C7 T cells.<sup>104</sup>

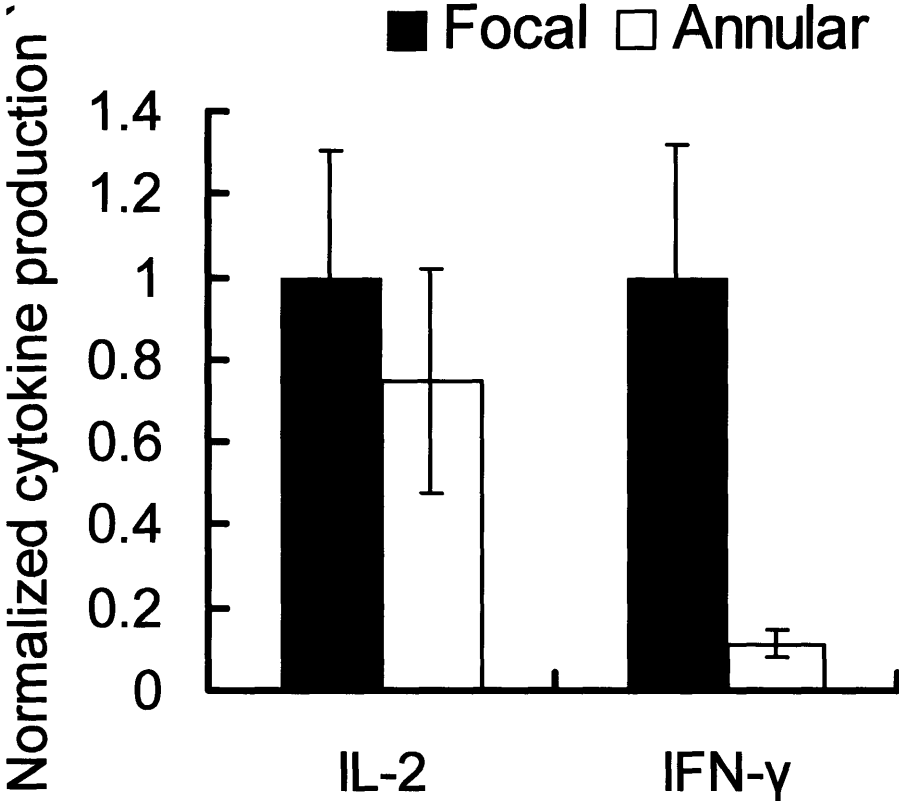


**Figure 5. 7 IL-2 and IFN-γ secreted by 5C.C7 T cells cultured on focal vs. annular activation site patterns after 48 hrs, normalized by cytokine concentrations secreted on focal patterns (ave ± s.e.m from 3 independent experiments).**

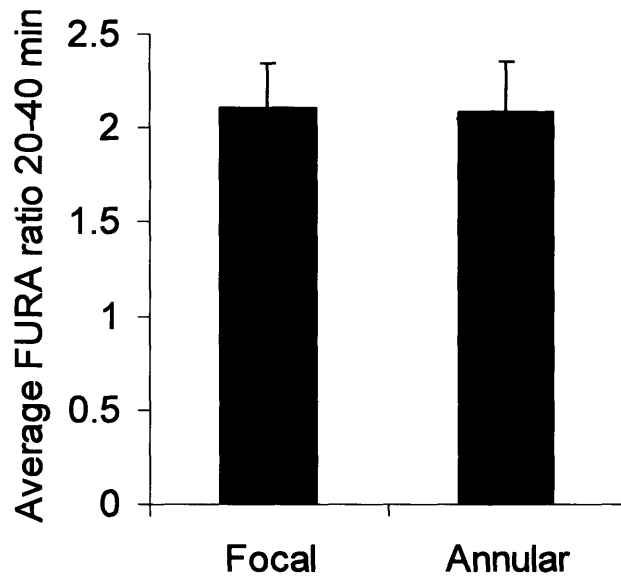


**Figure 5. 8 Time average (20-40 min) FURA ratio of T cells on focal and annular activation sites.**

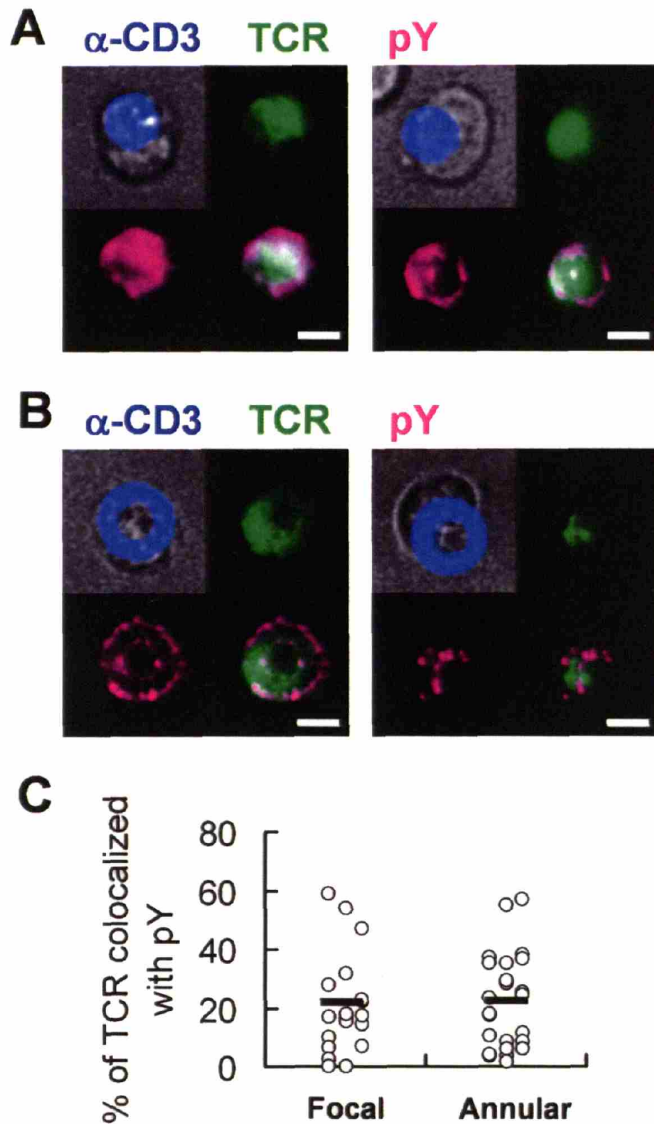


**Figure 5.9** Subcellular localization of TCR and cytoplasmic phosphotyrosine (pY) in T cells interacting with ‘focal’ and ‘annular’ anti-CD3 activation sites. T cells were fixed, permeabilized, and stained 10 min after seeding on synapse surfaces. (A) and (B) Representative micrographs of 5C.C7 CD4<sup>+</sup> T cells interacting with focal and annular activation sites, respectively: DIC/activation site fluorescence overlay (left top), TCR (right top), pY (left bottom), and TCR/pY overlay (right bottom). Scale bars, 5  $\mu$ m. (C) TCR-phosphotyrosine colocalization: TCR/pY immunostaining images were analyzed as described.<sup>36</sup> Average values are shown as solid bars (focal activation sites:  $n = 18$ , annular activation sites:  $n = 27$ ). Differences in the TCR/pY colocalization on focal and annular activation sites were not statistically significant ( $p = 0.99$ ).



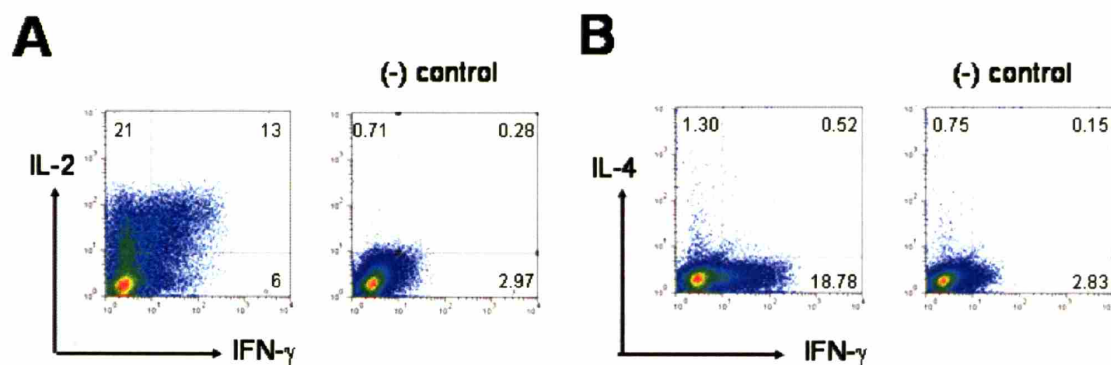


**Figure 5. 10** Th1/Th2 polarization of primed 5C.C7 T cells used in our studies revealed by intracellular cytokine staining followed by flow cytometry analysis. (A) IFN- $\gamma$  vs. IL-2. (B) IFN- $\gamma$  vs. IL-4. Numbers in each quadrant denote the percentage of cells falling in each region.

## **6 Conclusions and Future Work**

### **6.1 A Novel in vitro Platform for Studying Cell Biology**

In this thesis, we have demonstrated that events in T cell activation observed either in vivo or in vitro can be recapitulated on two-component protein patterned surfaces fabricated by photolithography using PNMP photoresist polymers. Moreover, this artificial in vitro model system enabled us to discover that altered TCR ligand distributions can affect the cytokine secretion of T cells.

The ability to pattern commercially-available proteins into defined, segregated regions while retaining activity makes the patterning strategy described here immediately applicable to a broad range of readily-available protein ligands of interest to many problems in cell biology. In contrast to many other techniques developed for protein patterning, where the preparation of large uniformly-patterned surfaces may be problematic, our patterned surfaces can be used for bulk population assays developed extensively in biochemistry and cell biology as well as microscopy study.

The immunological synapse arrays demonstrated in this thesis allow T cell responses to be monitored from initial signaling events occurring within seconds to proliferation and cytokine production occurring 20-30 hrs after the onset of activation, at the population or single-cell levels. Also, this model system captures the essential feature of antigen presentation in lymph nodes while allows many standard experimental tools for manipulating and assaying cells in vitro study to be applied. By combining many well-established conventional biology techniques for manipulating cellular functions including pharmacological treatment and genetic engineering such as gene knock-out and GFP-fusions with this artificially fabricated surface, many persistent problems in T cell biology can be tackled.

## **6.2 Issues for Future Work**

### **6.2.1 Effect of costimulation**

In this thesis, we mostly focused on two key signals for T cell activation: activation signals triggered by TCR ligation and adhesion signals mediated by the T cell integrin LFA-1. Another important signal in T cell activation is costimulation through the ligation of receptors such as CD28,<sup>121</sup> 4-1BB, and OX40<sup>122</sup> in T cells. In particular, CD28 plays a essential role in activating naïve T cells and augmenting T cell responses.<sup>123</sup> Also, there is

much evidence that CD28 is recruited into the center of the synapse upon TCR triggering.<sup>124-127</sup> Interestingly, CD28 has two different native ligands expressed on antigen presenting cells, B7-1 and B7-2, that can also bind to the T cell receptor cytotoxic T lymphocyte antigen-4 (CTLA-4) that is directed to the synapse in a TCR signaling strength-dependent manner after several hours of TCR signaling<sup>128</sup> and mostly attenuates activation signals.<sup>129-132</sup> It has also been proposed that B7-1 and B7-2 may have different affinity and avidity toward CD28 and CTLA-4,<sup>133</sup> which may indicate distinct roles for these molecules in tuning T cell activation.<sup>126,134</sup> It would be interesting to study the effect of B7-1 and B7-2 in T cell responses and compare those with anti-CD28 and anti-CTLA-4, which specifically bind to CD28 and CTLA-4 respectively. In particular, tracking the dynamics of T cells over long period of time by long-term video microscopy on different co-stimulatory ligands immobilized surfaces would provide a new insight to their role in T cell activation, synapse resolution, and late-term T cell behaviors.

### **6.2.2 Effect of nano-scale ligand segregation**

Recent total internal reflection fluorescence microscope studies have shown that nanoscale TCR clusters form at the periphery of the immunological synapse and translate toward the center to initiate<sup>71</sup> and maintain<sup>72</sup> TCR signaling. Also, it was demonstrated

that key signaling molecules in TCR signaling are physically associated by protein-protein interactions, forming pre-existing nanoscale clusters that might facilitate integration of signals.<sup>70</sup> The importance of TCR nanoclustering on TCR signaling can be straightforwardly tested by patterning TCR ligand bearing nanospheres on the activation sites of the immunological synapse arrays. Since the protein patterning technique described here is based on a ‘lift-off’ process under mild processing conditions, it can be readily extended to protein-coupled nanoparticle patterning. Promising preliminary results are shown in Figure 6. 1. SA<sub>v</sub> bearing quantum dots (Quantum Dot Corporation, Figure 6. 1A) or neutravidin conjugated polystyrene nanospheres (Molecular Probes, data not shown) were patterned on the surfaces by simply modifying the procedure shown in Figure 3. 8. Anti-CD3 immobilized nanosphere patterned surfaces induced calcium immobilization (data not shown) and TCR clustering (Figure 6. 1B) in T cells. With these promising results, it will be interesting to vary the size of cluster by varying particle sizes and see the effect of TCR cluster size on T cell activation.

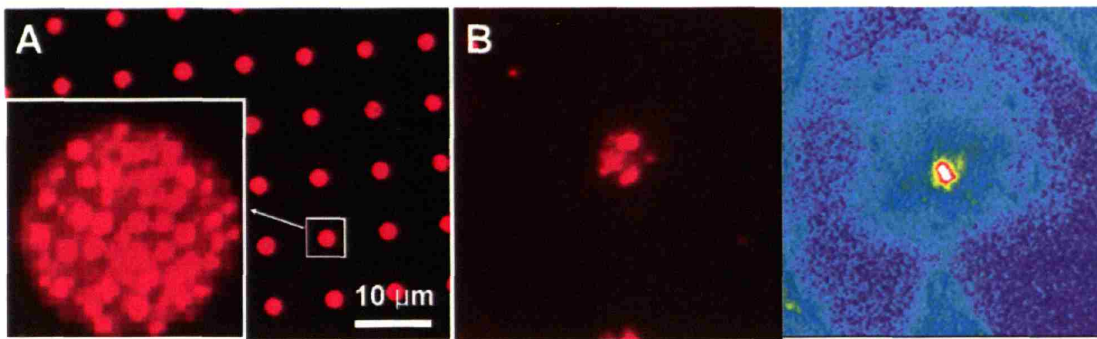


**Figure 6. 1 (A) Fluorescence micrograph of streptavidin bearing quantum dot patterned surface. (B) TCR clustering on nanosphere patterned activation domain. Red fluorescence from ligand-presenting nanospheres (left) and false color fluorescence image from anti-TCR antibody staining (right).**

We may also control the proximity of two different ligated receptors as schematically illustrated in Figure 6. 2. This will enable us to address arrays of interesting questions regarding TCR signaling. One example shown in Figure 6. 2 is controlling cross-talk between TCR and costimulatory molecules, which has not been tested.

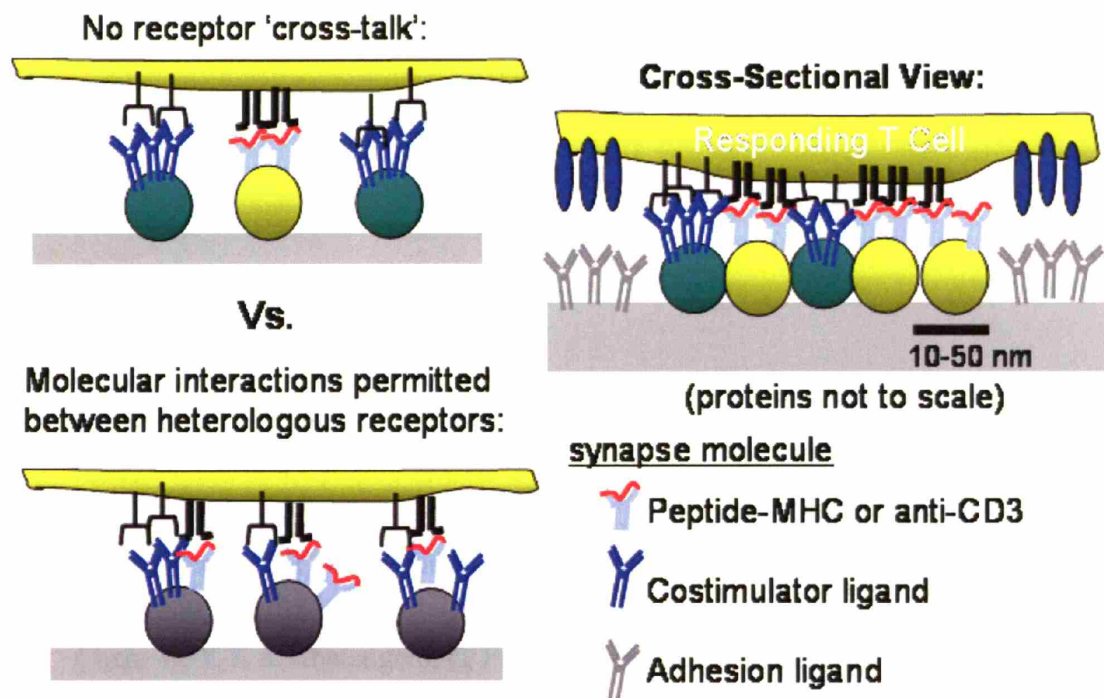


**Figure 6. 2 Schematic representation of nanoparticle patterned surfaces for studying the effect of nanoscale ligands segregation. Each ligand can be immobilized on different nanoparticles (left top) to prevent cross-talk between two different receptors or on the same nanoparticles (left bottom) to promote receptor interactions.**

## 7 Bibliography

1. Cukierman, E., Pankov, R. & Yamada, K. M. Cell interactions with three-dimensional matrices. *Current Opinion in Cell Biology* **14**, 633-639 (2002).
2. Park, C. C., Bissell, M. J. & Barcellos-Hoff, M. H. The influence of the microenvironment on the malignant phenotype. *Molecular Medicine Today* **6**, 324-329 (2000).
3. Chen, W. Y. J. & Abatangelo, G. Functions of hyaluronan in wound repair. *Wound Repair and Regeneration* **7**, 79-89 (1999).
4. Butcher, E. C. & Picker, L. J. Lymphocyte homing and homeostasis. *Science* **272**, 60-66 (1996).
5. Folch, A. & Toner, M. Microengineering of cellular interactions. *Annual Review of Biomedical Engineering* **2**, 227-256 (2000).
6. Whitesides, G. M., Ostuni, E., Takayama, S., Jiang, X. Y. & Ingber, D. E. Soft lithography in biology and biochemistry. *Annual Review of Biomedical Engineering* **3**, 335-373 (2001).
7. Raghavan, S. & Chen, C. S. Micropatterned environments in cell biology. *Advanced Materials* **16**, 1303-1313 (2004).
8. Chen, C. S., Mrksich, M., Huang, S., Whitesides, G. M. & Ingber, D. E. Geometric control of cell life and death. *Science* **276**, 1425-1428 (1997).
9. Koo, L. Y., Irvine, D. J., Mayes, A. M., Lauffenburger, D. A. & Griffith, L. G. Co-regulation of cell adhesion by nanoscale RGD organization and mechanical stimulus. *Journal of Cell Science* **115**, 1423-1433 (2002).
10. Jiang, X. Y., Bruzewicz, D. A., Wong, A. P., Piel, M. & Whitesides, G. M. Directing cell migration with asymmetric micropatterns. *Proceedings of the National Academy of Sciences of the United States of America* **102**, 975-978 (2005).
11. They, M. et al. The extracellular matrix guides the orientation of the cell division axis. *Nature Cell Biology* **7**, 947-U29 (2005).
12. Wu, M., Holowka, D., Craighead, H. G. & Baird, B. Visualization of plasma



- membrane compartmentalization with patterned lipid bilayers. *Proceedings of the National Academy of Sciences of the United States of America* **101**, 13798-13803 (2004).
13. McBeath, R., Pirone, D. M., Nelson, C. M., Bhadriraju, K. & Chen, C. S. Cell shape, cytoskeletal tension, and RhoA regulate stem cell lineage commitment. *Developmental Cell* **6**, 483-495 (2004).
  14. Grakoui, A. et al. The immunological synapse: A molecular machine controlling T cell activation. *Science* **285**, 221-227 (1999).
  15. Dustin, M. L. & Colman, D. R. Neural and immunological synaptic relations. *Science* **298**, 785-789 (2002).
  16. Giancotti, F. G. & Ruoslahti, E. Transduction - Integrin signaling. *Science* **285**, 1028-1032 (1999).
  17. Davis, D. M. et al. The human natural killer cell immune synapse. *Proceedings of the National Academy of Sciences of the United States of America* **96**, 15062-15067 (1999).
  18. Monks, C. R. F., Freiberg, B. A., Kupfer, H., Sciaky, N. & Kupfer, A. Three-dimensional segregation of supramolecular activation clusters in T cells. *Nature* **395**, 82-86 (1998).
  19. Negulescu, P. A., Krasieva, T. B., Khan, A., Kerschbaum, H. H. & Cahalan, M. D. Polarity of T cell shape, motility, and sensitivity to antigen. *Immunity* **4**, 421-430 (1996).
  20. Dustin, M. L., Bromley, S. K., Kan, Z. Y., Peterson, D. A. & Unanue, E. R. Antigen receptor engagement delivers a stop signal to migrating T lymphocytes. *Proceedings of the National Academy of Sciences of the United States of America* **94**, 3909-3913 (1997).
  21. Wulfing, C., Sjaastad, M. D. & Davis, M. M. Visualizing the dynamics of T cell activation: Intracellular adhesion molecule 1 migrates rapidly to the T cell/B cell interface and acts to sustain calcium levels. *Proceedings of the National Academy of Sciences of the United States of America* **95**, 6302-6307 (1998).
  22. Donnadieu, E., Bismuth, C. & Trautmann, A. Antigen Recognition by Helper T-Cells Elicits a Sequence of Distinct Changes of Their Shape and Intracellular Calcium. *Current Biology* **4**, 584-595 (1994).
  23. Delon, J., Bercovici, N., Liblau, R. & Trautmann, A. Imaging antigen recognition by naive CD4(+) T cells: compulsory cytoskeletal alterations for the triggering of an intracellular calcium response. *European Journal of Immunology* **28**, 716-729 (1998).
  24. Huppa, J. B., Gleimer, M., Sumen, C. & Davis, M. M. Continuous T cell receptor

- signaling required for synapse maintenance and full effector potential. *Nature Immunology* **4**, 749-755 (2003).
25. Kupfer, A. & Singer, S. J. The Specific Interaction of Helper T-Cells and Antigen-Presenting B-Cells .4. Membrane and Cytoskeletal Reorganizations in the Bound T-Cell as a Function of Antigen Dose. *Journal of Experimental Medicine* **170**, 1697-1713 (1989).
  26. Lee, K. H. et al. T cell receptor signaling precedes immunological synapse formation. *Science* **295**, 1539-1542 (2002).
  27. Watson, A. R. O. & Lee, W. T. Differences in signaling molecule organization between naive and memory CD4(+) T lymphocytes. *Journal of Immunology* **173**, 33-41 (2004).
  28. Purdie, B., Pitcher, L. A., van Oers, N. S. C. & Wulfigg, C. T cell receptor (TCR) clustering in the immunological synapse integrates TCR and costimulatory signaling in selected T cells. *Proceedings of the National Academy of Sciences of the United States of America* **102**, 2904-2909 (2005).
  29. Purbhoo, M. A., Irvine, D. J., Huppa, J. B. & Davis, M. M. T cell killing does not require the formation of a stable mature immunological synapse. *Nature Immunology* **5**, 524-530 (2004).
  30. Faroudi, M. et al. Lytic versus stimulatory synapse in cytotoxic T lymphocyte/target cell interaction: Manifestation of a dual activation threshold. *Proceedings of the National Academy of Sciences of the United States of America* **100**, 14145-14150 (2003).
  31. Richie, L. I. et al. Imaging synapse formation during thymocyte selection: Inability of CD3 zeta to form a stable central accumulation during negative selection. *Immunity* **16**, 595-606 (2002).
  32. Hallman, E., Burack, W. R., Shaw, A. S., Dustin, M. L. & Allen, P. M. Immature CD4(+)CD8(+) thymocytes form a multifocal immunological synapse with sustained tyrosine phosphorylation. *Immunity* **16**, 839-848 (2002).
  33. Brossard, C. et al. Multifocal structure of the T cell - dendritic cell synapse. *European Journal of Immunology* **35**, 1741-1753 (2005).
  34. Friedl, P., den Boer, A. T. & Gunzer, M. Tuning immune responses: Diversity and adaptation of the immunological synapse. *Nature Reviews Immunology* **5**, 532-545 (2005).
  35. Trautmann, A. & Valitutti, S. The diversity of immunological synapses. *Current Opinion in Immunology* **15**, 249-254 (2003).
  36. Mossman, K. D., Campi, G., Groves, J. T. & Dustin, M. L. Altered TCR signaling

from geometrically repatterned immunological synapses. *Science* **310**, 1191-1193 (2005).

37. Blawas, A. S. & Reichert, W. M. Protein patterning. *Biomaterials* **19**, 595-609 (1998).
38. Sorribas, H., Padeste, C. & Tiefenauer, L. Photolithographic generation of protein micropatterns for neuron culture applications. *Biomaterials* **23**, 893-900 (2002).
39. Orth, R. N., Clark, T. G. & Craighead, H. G. Avidin-biotin micropatterning methods for biosensor applications. *Biomedical Microdevices* **5**, 29-34 (2003).
40. Sundberg, S. A. et al. Spatially-Addressable Immobilization of Macromolecules on Solid Supports. *Journal of the American Chemical Society* **117**, 12050-12057 (1995).
41. Zhang, K., Diehl, M. R. & Tirrell, D. A. Artificial Polypeptide Scaffold for Protein Immobilization. *Journal of the American Chemical Society* **127**, 10136-10137 (2005).
42. Holden, M. A. & Cremer, P. S. Light activated patterning of dye-labeled molecules on surfaces. *Journal of the American Chemical Society* **125**, 8074-8075 (2003).
43. Blawas, A. S., Oliver, T. F., Pirrung, M. C. & Reichert, W. M. Step-and-Repeat Photopatterning of Protein Features Using Caged-Biotin--BSA: Characterization and Resolution. *Langmuir* **14**, 4243-4250 (1998).
44. Pritchard, D. J., Morgan, H. & Cooper, J. M. Micron-Scale Patterning of Biological Molecules. *Angew. Chem. Int. Ed. Engl* **34**, 91-93 (1995).
45. Bernard, A., Renault, J. P., Michel, B., Bosshard, H. R. & Delamarche, E. Microcontact printing of proteins. *Advanced Materials* **12**, 1067-1070 (2000).
46. Tien, J., Nelson, C. M. & Chen, C. S. Fabrication of aligned microstructures with a single elastomeric stamp. *Proceedings of the National Academy of Sciences of the United States of America* **99**, 1758-1762 (2002).
47. Yang, Z. P. & Chilkoti, A. Microstamping of a biological ligand onto an activated polymer surface. *Advanced Materials* **12**, 413-+ (2000).
48. Pirrung, M. C. & Huang, C. Y. A general method for the spatially defined immobilization of biomolecules on glass surfaces using "caged" biotin. *Bioconjugate Chemistry* **7**, 317-321 (1996).
49. Kodadek, T. Protein microarrays: prospects and problems. *Chemistry & Biology* **8**, 105-115 (2001).
50. de Wildt, R. M. T., Mundy, C. R., Gorick, B. D. & Tomlinson, I. M. Antibody arrays for high-throughput screening of antibody-antigen interactions. *Nature Biotechnology* **18**, 989-994 (2000).
51. Cahalan, M. D. & Parker, I. Close encounters of the first and second kind: T-DC and T-B interactions in the lymph node. *Seminars in Immunology* **17**, 442-451 (2005).
52. Dustin, M. L. A dynamic view of the immunological synapse. *Seminars in*

- Immunology* **17**, 400-410 (2005).
53. Halin, C., Mora, J. R., Sumen, C. & von Andrian, U. H. In vivo imaging of lymphocyte trafficking. *Annual Review of Cell and Developmental Biology* **21**, 581-603 (2005).
  54. Friedman, R. S., Jacobelli, J. & Krummel, M. F. Mechanisms of T cell motility and arrest: Deciphering the relationship between intra- and extracellular determinants. *Seminars in Immunology* **17**, 387-399 (2005).
  55. Huppa, J. B. & Davis, M. M. T-cell-antigen recognition and the immunological synapse. *Nature Reviews Immunology* **3**, 973-983 (2003).
  56. Davis, D. M. & Dustin, M. L. What is the importance of the immunological synapse? *Trends in Immunology* **25**, 323-327 (2004).
  57. Miller, M. J., Wei, S. H., Parker, I. & Cahalan, M. D. Two-photon imaging of lymphocyte motility and antigen response in intact lymph node. *Science* **296**, 1869-1873 (2002).
  58. Miller, M. J., Wei, S. H., Cahalan, M. D. & Parker, I. Autonomous T cell trafficking examined in vivo with intravital two-photon microscopy. *Proceedings of the National Academy of Sciences of the United States of America* **100**, 2604-2609 (2003).
  59. Bousso, P. & Robey, E. Dynamics of CD8(+) T cell priming by dendritic cells in intact lymph nodes. *Nature Immunology* **4**, 579-585 (2003).
  60. Celli, S., Garcia, Z. & Bousso, P. CD4 T cells integrate signals delivered during successive DC encounters in vivo. *Journal of Experimental Medicine* **202**, 1271-1278 (2005).
  61. Mempel, T. R., Henrickson, S. E. & von Andrian, U. H. T-cell priming by dendritic cells in lymph nodes occurs in three distinct phases. *Nature* **427**, 154-159 (2004).
  62. Miller, M. J., Safrina, O., Parker, I. & Cahalan, M. D. Imaging the single cell dynamics of CD4(+) T cell activation by dendritic cells in lymph nodes. *Journal of Experimental Medicine* **200**, 847-856 (2004).
  63. Shakhar, G. et al. Stable T cell-dendritic cell interactions precede the development of both tolerance and immunity in vivo. *Nature Immunology* **6**, 707-714 (2005).
  64. Okada, T. et al. Antigen-engaged B cells undergo chemotaxis toward the T zone and form motile conjugates with helper T cells. *Plos Biology* **3**, 1047-1061 (2005).
  65. Germain, R. N. Imaging dynamic interactions in immune responses. *Seminars in Immunology* **17**, 385-386 (2005).
  66. Lee, K. H. et al. The immunological synapse balances T cell receptor signaling and degradation. *Science* **302**, 1218-1222 (2003).
  67. Faroudi, M., Zaru, R., Paulet, P., Muller, S. & Valitutti, S. Cutting edge: T lymphocyte

- activation by repeated immunological synapse formation and intermittent signaling. *Journal of Immunology* **171**, 1128-1132 (2003).
68. Zaru, R., Cameron, T. O., Stern, L. J., Muller, S. & Valitutti, S. Cutting edge: TCR engagement and triggering in the absence of large-scale molecular segregation at the T cell-APC contact site. *Journal of Immunology* **168**, 4287-4291 (2002).
  69. Irvine, D. J., Purbhoo, M. A., Krogsaard, M. & Davis, M. M. Direct observation of ligand recognition by T cells. *Nature* **419**, 845-849 (2002).
  70. Douglass, A. D. & Vale, R. D. Single-molecule microscopy reveals plasma membrane microdomains created by protein-protein networks that exclude or trap signaling molecules in T cells. *Cell* **121**, 937-950 (2005).
  71. Campi, G., Varma, R. & Dustin, M. L. Actin and agonist MHC-peptide complex-dependent T cell receptor microclusters as scaffolds for signaling. *Journal of Experimental Medicine* **202**, 1031-1036 (2005).
  72. Yokosuka, T. et al. Newly generated T cell receptor microclusters initiate and sustain T cell activation by recruitment of Zap70 and SLP-76. *Nature Immunology* **6**, 1253-1262 (2005).
  73. Barda-Saad, M. et al. Dynamic molecular interactions linking the T cell antigen receptor to the actin cytoskeleton. *Nature Immunology* **6**, 80-89 (2005).
  74. Lindquist, R. L. et al. Visualizing dendritic cell networks in vivo. *Nature Immunology* **5**, 1243-1250 (2004).
  75. Barzynski, H. & Sanger, D. Photolysis of Macromolecular Ortho-Nitrobenzyl Derivates. *Angewandte Makromolekulare Chemie* **93**, 131-141 (1981).
  76. Schwalm, R. Lithographic Evaluation of One-Component Deep-Uv Resists Containing Ortho-Nitrobenzyl Ester Moieties. *Journal of the Electrochemical Society* **136**, 3471-3476 (1989).
  77. Doh, J. & Irvine, D. J. Photogenerated polyelectrolyte bilayers from an aqueous-processible photoresist for multicomponent protein patterning. *Journal of the American Chemical Society* **126**, 9170-9171 (2004).
  78. Banerjee, P., Irvine, D. J., Mayes, A. M. & Griffith, L. G. Polymer latexes for cell-resistant and cell-interactive surfaces. *Journal of Biomedical Materials Research* **50**, 331-339 (2000).
  79. Irvine, D. J., Mayes, A. M. & Griffith, L. G. Nanoscale clustering of RGD peptides at surfaces using comb polymers. 1. Synthesis and characterization of comb thin films. *Biomacromolecules* **2**, 85-94 (2001).
  80. Bednar, B., Morawetz, H. & Shafer, J. A. Kinetics of the Conformational Transition of Poly(Methacrylic Acid) after Changes of Its Degree of Ionization. *Macromolecules* **18**,

1940-1944 (1985).

81. Gramain, P. & Frere, Y. Preparation of Monomethoxy-Poly(Ethylene Oxide) Acrylate and Methacrylate and Its Polymerization - Self-Gelling Polymers. *Polymer Communications* **27**, 16-18 (1986).
82. Ito, K. et al. Poly(Ethylene Oxide) Macromonomers .7. Micellar Polymerization in Water. *Macromolecules* **24**, 2348-2354 (1991).
83. Huang, J. & Wu, X. Y. Effects of pH, salt, surfactant and composition on phase transition of poly(NIPAm/MAA) nanoparticles. *Journal of Polymer Science Part a-Polymer Chemistry* **37**, 2667-2676 (1999).
84. Liu, S. Y., Yang, M. J. & Dan, Y. Complex system of poly(methacrylic acid) with poly(vinylpyrrolidone) in aqueous media. *Journal of Applied Polymer Science* **96**, 2280-2286 (2005).
85. Pohlmeier, A. & Haber-Pohlmeier, S. Ionization of short polymethacrylic acid: titration, DLS, and model calculations. *Journal of Colloid and Interface Science* **273**, 369-380 (2004).
86. Poe, G. D., Jarrett, W. L., Scales, C. W. & McCormick, C. L. Enhanced coil expansion and intrapolymer complex formation of linear poly(methacrylic acid) containing poly(ethylene glycol) grafts. *Macromolecules* **37**, 2603-2612 (2004).
87. Kim, B. & Peppas, N. A. Analysis of molecular interactions in poly(methacrylic acid-g-ethylene glycol) hydrogels. *Polymer* **44**, 3701-3707 (2003).
88. Lowman, A. M. & Peppas, N. A. Analysis of the complexation/decomplexation phenomena in graft copolymer networks. *Macromolecules* **30**, 4959-4965 (1997).
89. Hemker, D. J., Garza, V. & Frank, C. W. Complexation of Poly(Acrylic Acid) and Poly(Methacrylic Acid) with Pyrene-End-Labeled Poly(Ethylene Glycol) - Ph and Fluorescence Measurements. *Macromolecules* **23**, 4411-4418 (1990).
90. Sukhishvili, S. A. & Granick, S. Layered, erasable polymer multilayers formed by hydrogen-bonded sequential self-assembly. *Macromolecules* **35**, 301-310 (2002).
91. Sukhishvili, S. A. & Granick, S. Layered, erasable, ultrathin polymer films. *Journal of the American Chemical Society* **122**, 9550-9551 (2000).
92. Lee, J. Y., Painter, P. C. & Coleman, M. M. Hydrogen-Bonding in Polymer Blends .3. Blends Involving Polymers Containing Methacrylic-Acid and Ether Groups. *Macromolecules* **21**, 346-354 (1988).
93. Bell, C. L. & Peppas, N. A. Swelling/syneresis phenomena in gel-forming interpolymer complexes. *Journal of Biomaterials Science-Polymer Edition* **7**, 671-683 (1996).
94. Sandberg, S. A. et al. Spatially-Addressable Immobilization of Macromolecules on

- Solid Supports. *Journal of the American Chemical Society* **117**, 12050-12057 (1995).
95. Shiratori, S. S. & Rubner, M. F. pH-dependent thickness behavior of sequentially adsorbed layers of weak polyelectrolytes. *Macromolecules* **33**, 4213-4219 (2000).
  96. Yoo, D., Shiratori, S. S. & Rubner, M. F. Controlling bilayer composition and surface wettability of sequentially adsorbed multilayers of weak polyelectrolytes. *Macromolecules* **31**, 4309-4318 (1998).
  97. Yang, S. Y. & Rubner, M. F. Micropatterning of polymer thin films with pH-sensitive and cross-linkable hydrogen-bonded polyelectrolyte multilayers. *Journal of the American Chemical Society* **124**, 2100-2101 (2002).
  98. Harris, J. M. *Poly(ethylene glycol) Chemistry: Biotechnical and Biomedical Applications* (Plenum Press, New York, 1992).
  99. Prime, K. L. & Whitesides, G. M. Adsorption of Proteins onto Surfaces Containing End-Attached Oligo(Ethylene Oxide) - a Model System Using Self-Assembled Monolayers. *Journal of the American Chemical Society* **115**, 10714-10721 (1993).
  100. Kuhl, P. R. & Griffith-Cima, L. G. Tethered epidermal growth factor as a paradigm for growth factor-induced stimulation from the solid phase. *Nature Medicine* **2**, 1022-1027 (1996).
  101. Hermanson, G. T. *Bioconjugate Techniques* (Academic Press, San Diego, 1996).
  102. Harlow, E. & Lane, D. *Antibodies: a laboratory manual* (Cold Spring Harbor Laboratory, 1988).
  103. Robertson, J. M., Jensen, P. E. & Evavold, B. D. DO11.10 and OT-II T cells recognize a C-terminal ovalbumin 323-339 epitope. *Journal of Immunology* **164**, 4706-4712 (2000).
  104. Seder, R. A., Paul, W. E., Davis, M. M. & Destgroth, B. F. The Presence of Interleukin-4 During Invitro Priming Determines the Lymphokine-Producing Potential of Cd4+ T-Cells from T-Cell Receptor Transgenic Mice. *Journal of Experimental Medicine* **176**, 1091-1098 (1992).
  105. Smith, A., Bracke, M., Leitinger, B., Porter, J. C. & Hogg, N. LFA-1-induced T cell migration on ICAM-1 involves regulation of MLCK-mediated attachment and ROCK-dependent detachment. *Journal of Cell Science* **116**, 3123-3133 (2003).
  106. Bretscher, M. S. Cells Can Use Their Transferrin Receptors for Locomotion. *Embo Journal* **11**, 383-389 (1992).
  107. Leo, O., Foo, M., Sachs, D. H., Samelson, L. E. & Bluestone, J. A. Identification of a Monoclonal-Antibody Specific for a Murine T3 Polypeptide. *Proceedings of the National Academy of Sciences of the United States of America* **84**, 1374-1378 (1987).
  108. Bruniquel, D. & Schwartz, R. H. Selective, stable demethylation of the interleukin-2

- gene enhances transcription by an active process. *Nature Immunology* **4**, 235-240 (2003).
109. Lee, K. M. et al. Molecular basis of T cell inactivation by CTLA-4. *Science* **282**, 2263-2266 (1998).
  110. Lewis, R. S. & Cahalan, M. D. Potassium and Calcium Channels in Lymphocytes. *Annual Review of Immunology* **13**, 623-653 (1995).
  111. Vansventer, G. A. et al. Analysis of T-Cell Stimulation by Superantigen Plus Major Histocompatibility Complex Class-II Molecules or by Cd3 Monoclonal-Antibody - Costimulation by Purified Adhesion Ligands Vcam-1, Icam-1, but Not Elam-1. *Journal of Experimental Medicine* **174**, 901-913 (1991).
  112. Kuhlman, P., Moy, V. T., Lollo, B. A. & Brian, A. A. The Accessory Function of Murine Intercellular-Adhesion Molecule-1 in Lymphocyte-T Activation - Contributions of Adhesion and Coactivation. *Journal of Immunology* **146**, 1773-1782 (1991).
  113. O'Keefe, J. P., Blaine, K., Alegre, M. L. & Gajewski, T. F. Formation of a central supramolecular activation cluster is not required for activation of naive CD8(+) T cells. *Proceedings of the National Academy of Sciences of the United States of America* **101**, 9351-9356 (2004).
  114. Tooley, A. J., Jacobelli, J., Moldovan, M. C., Douglas, A. & Krummel, M. F. T cell synapse assembly: proteins, motors and the underlying cell biology. *Seminars in Immunology* **17**, 65-75 (2005).
  115. Wei, X. B., Tromberg, B. J. & Cahalan, M. D. Mapping the sensitivity of T cells with an optical trap: Polarity and minimal number of receptors for Ca<sup>2+</sup> signaling. *Proceedings of the National Academy of Sciences of the United States of America* **96**, 8471-8476 (1999).
  116. Jacobelli, J., Chmura, S. A., Buxton, D. B., Davis, M. M. & Krummel, M. F. A single class II myosin modulates T cell motility and stopping, but not synapse formation. *Nature Immunology* **5**, 531-538 (2004).
  117. Krummel, M. F., Sjaastad, M. D., Wulfig, C. & Davis, M. M. Differential clustering of CD4 and CD3 zeta during T cell recognition. *Science* **289**, 1349-1352 (2000).
  118. Monks, C. R. F., Kupfer, H., Tamir, I., Barlow, A. & Kupfer, A. Selective modulation of protein kinase C-theta during T-cell activation. *Nature* **385**, 83-86 (1997).
  119. Depoil, D. et al. Immunological synapses are versatile structures enabling selective T cell polarization. *Immunity* **22**, 185-194 (2005).
  120. Balamuth, F., Leitenberg, D., Unternaehrer, J., Mellman, I. & Bottomly, K. Distinct patterns of membrane microdomain partitioning in Th1 and Th2 cells. *Immunity* **15**,



- 729-738 (2001).
121. Lenschow, D. J., Walunas, T. L. & Bluestone, J. A. CD28/B7 system of T cell costimulation. *Annual Review of Immunology* **14**, 233-258 (1996).
  122. Watts, T. H. Tnf/tnfr family members in costimulation of T cell responses. *Annual Review of Immunology* **23**, 23-68 (2005).
  123. Sagerstrom, C. G., Kerr, E. M., Allison, J. P. & Davis, M. M. Activation and Differentiation Requirements of Primary T-Cells in-Vitro. *Proceedings of the National Academy of Sciences of the United States of America* **90**, 8987-8991 (1993).
  124. Andres, P. G. et al. CD28 signals in the immature immunological synapse. *Journal of Immunology* **172**, 5880-5886 (2004).
  125. Bromley, S. K. et al. The immunological synapse and CD28-CD80 interactions. *Nature Immunology* **2**, 1159-1166 (2001).
  126. Pentcheva-Hoang, T., Egen, J. G., Wojnoonski, K. & Allison, J. P. B7-1 and B7-2 selectively recruit CTLA-4 and CD28 to the immunological synapse. *Immunity* **21**, 401-413 (2004).
  127. Tseng, S. Y., Liu, M. L. & Dustin, M. L. CD80 cytoplasmic domain controls localization of CD28, CTLA-4, and protein kinase C theta in the immunological synapse. *Journal of Immunology* **175**, 7829-7836 (2005).
  128. Egen, J. G. & Allison, J. P. Cytotoxic T lymphocyte antigen-4 accumulation in the immunological synapse is regulated by TCR signal strength. *Immunity* **16**, 23-35 (2002).
  129. Greenwald, R. J., Freeman, G. J. & Sharpe, A. H. The B7 family revisited. *Annual Review of Immunology* **23**, 515-548 (2005).
  130. Carreno, B. M. & Collins, M. The B7 family of ligands and its receptors: New pathways for costimulation and inhibition of immune responses. *Annual Review of Immunology* **20**, 29-53 (2002).
  131. Saito, T. & Yamasaki, S. Negative feedback of T cell activation through inhibitory adapters and costimulatory receptors. *Immunological Reviews* **192**, 143-160 (2003).
  132. Thompson, C. B. & Allison, J. P. The emerging role of CTLA-4 as an immune attenuator. *Immunity* **7**, 445-450 (1997).
  133. Collins, A. V. et al. The interaction properties of costimulatory molecules revisited. *Immunity* **17**, 201-210 (2002).
  134. Sansom, D. M., Manzotti, C. N. & Zheng, Y. What's the difference between CD80 and CD86? *Trends in Immunology* **24**, 314-319 (2003).

## 8 Biographical Note

### Junsang Doh

- Education**      **Massachusetts Institute of Technology**  
Ph.D. Candidate in Chemical Engineering / Program in Polymer Science and  
Technology, 9/2001 ~ 6/2006
- Seoul National University**  
Bachelor of Science in Chemical Engineering, 3/1995 ~ 2/1999.  
*Summa Cum Laude*
- Research**      **Massachusetts Institute of Technology**  
**Experiences**    1/2002 ~ present, Graduate Research Assistant  
Advisor: Prof. Darrell J. Irvine  
Developing novel patterned surfaces presenting multiple proteins in multiple length  
scales to control immune cell functions.
- Synthesis of new types of photoresist polymers for the multiple  
                 patterning of biological molecules.
  - Synthesis and functionalization of polymeric colloids for protein  
                 immobilization and 2-D colloidal assembly.
  - Study cell- fabricated surface interactions by video fluorescence  
                 microscopy and bulk assays
- Developed cell-based biosensors for detecting pathogens.
- Seoul National University**  
12/1998 ~ 5/2001, Research Assistant

Advisor: Prof. Kookheon Char

Conducted Monte Carlo simulation to study the structure of semiflexible polymer brushes

**Teaching Experiences**      **Massachusetts Institute of Technology**

10/2004 ~ 12/2004, Teaching Assistant

Process Control by Design

Assisted students with individual questions regarding course materials. Graded course assignments.

**Massachusetts Institute of Technology**

1/2005, Teaching Assistant

Design of Heterogeneous Polymeric Gas Separation Membranes

Developed computational workshop.

**Awards/  
Honors**

ICI student award finalist, the American Chemical Society (ACS), 2005.

Gold Medal in Transport Phenomena Competition, the Korean Institute of Chemical Engineers (KIChE), 1998.

Honor Scholarship, 1997.

Bronze Medal in Math Competition for High School Students, Korean Education Ministry, 1994.

**Publications**

J. Doh and D.J. Irvine, Immunological synapse arrays: Patterned protein surfaces that modulate immunological synapse structure formation in T cells, *Proc. Natl. Acad. Sci. USA* **103** (15), 5700 (2006).

J.S. Katz, J. Doh, and D.J. Irvine, Composition-Tunable Properties of Amphiphilic Comb Terpolymers Containing Protected Methacrylic Acid Groups for Multicomponent Protein Patterning, *Langmuir* **22** (1), 353 (2006).

J. Doh and D.J. Irvine, Photogenerated polyelectrolyte bilayers from an aqueous-processible photoresist for multicomponent protein patterning., *J. Am. Chem. Soc.* **126** (30), 170 (2004).

H. Kim, J. Doh, D.J. Irvine, R.E. Cohen, and P.T. Hammond, Large area two-dimensional B cell arrays for sensing and cell-sorting applications, *Biomacromolecules* **5**, 822 (2004).

- Selected Presentations**
- J. Doh and D.J. Irvine, Aqueous-processible photoresist polymer for multiple protein patterning: synthesis, characterization, and application to T cell activation, American Chemical Societies 230<sup>th</sup> National Meeting, Washington, DC (2005).
- J. Doh and D.J. Irvine, Multicomponent protein patterning with photogenerated polyelectrolyte bilayers, Materials Research Societies 2004 Fall Meeting, Boston, Massachusetts (2004).
- J. Doh and D.J. Irvine, Multicomponent patterned surface for the control of *ex vivo* T cell activation, 7<sup>th</sup> World Biomaterials Congress, Sydney, Australia (2004).
- J. Doh and D.J. Irvine, Multicomponent protein patterning based on 2-D colloidal assembly, Materials Research Societies 2003 Fall Meeting, Boston, Massachusetts (2003).
- J. Doh and D.J. Irvine, Multicomponent patterned surface for the study of T cell activation, Society for Biomaterials 2003 Annual Meeting, Reno, Nevada (2003).
- J. Doh, K. Char, and G.G. Kim, "Structure of Semiflexible Polymer Brushes: A Monte Carlo Study.", Korean Society of Rheology 1999 Fall Meeting, Seoul, Korea (1999).
- Patents**
- J. Doh and D.J. Irvine, Photogenerated polyelectrolyte bilayers from an aqueous-processible photoresist for multicomponent protein patterning, USA patent, (provisional patent filed).
- H. Kim, J. Doh, D.J. Irvine, R.E. Cohen, P.T. Hammond, Large-area 2D B cell arrays, USA patent, (provisional patent filed).



Room 14-0551  
77 Massachusetts Avenue  
Cambridge, MA 02139  
Ph: 617.253.5668 Fax: 617.253.1690  
Email: docs@mit.edu  
<http://libraries.mit.edu/docs>

## **DISCLAIMER OF QUALITY**

Due to the condition of the original material, there are unavoidable flaws in this reproduction. We have made every effort possible to provide you with the best copy available. If you are dissatisfied with this product and find it unusable, please contact Document Services as soon as possible.

Thank you.

**Some pages in the original document contain color pictures or graphics that will not scan or reproduce well.**